Fully automated computer system for diagnosis of corneal diseases

Development of image processing technologies for the diagnosis of Acanthamoeba and Fusarium diseases in confocal microscopy images

Rania Saber Mohammad ALZUBAIDI

Submitted for the Degree of Doctor of Philosophy

Faculty of Engineering and Informatics

School of Electrical Engineering and Computer Science

University of Bradford

2017

Abstract

Rania Saber Mohammad Alzubaidi

Fully automated computer system for diagnosis of corneal diseases**.**

Development of image processing technologies for the diagnosis of Acanthamoeba and Fusarium diseases in confocal microscopy images.

Keywords: Image processing, Cornea, Digital diagnostic, Confocal microscopy, Infectious keratitis, Acanthamoeba, Fusarium.

Confocal microscopy demonstrated its value in the diagnosis of Acanthamoeba and fungal keratitis which considered sight-threatening corneal diseases. However, it can be difficult to find and train confocal microscopy graders to accurately detect Acanthamoeba cysts and fungal filaments in the images. Use of an automated system could overcome this problem and help to start the correct treatment more quickly. Also, response to treatment can be difficult to assess in infectious keratitis using clinical examination alone, but there is evidence that the morphology of filaments and cysts may change over time with the use of correct treatment. An automated system to analyse confocal microscopy images for such changes would also assist clinicians in determining whether the ulcer is improving, or whether a change of treatment is needed.

This research proposes a fully automated novel system with GUI to detect cysts and hyphae (filaments) and measure useful quantitative parameters for them through many stages; Image enhancement, image segmentation, quantitative analysis for detected cysts and hyphae, and registration and tracking of ordered sequence of images.

The performance of the proposed segmentation procedure is evaluated by comparing between the manual and the automated traced images of the dataset that was provided by the Manchester Royal Eye Hospital. The positive predictive values rate of cysts for Acanthamoeba images was 76%. For detected hyphae in Fusarium images, many standard measurements were computed. The accuracy of their values was quantified by calculating the percent error rate for each measurement and which ranged from 23% to 49%.

Dedications

To my Father and Mother,
To My Brothers and Sisters,
To My Nephews and Nieces.

Acknowledgments

All thankfulness to Allah, the most gracious and the most merciful, for giving me the strength, patience, and the capability to finish this crucial stage in my life.

I would like to destine my deepest gratitude to my first supervisor Prof. Rami Qahwaji who helped me to finish my PhD. His support, guidance, encouragement, constructive ideas and suggestions had a profound impact on my research. Also, I would like to thank him in particular for his patience.

My special thanks to my second supervisor Dr. Stanley Ipson who helped me greatly in improving my language and academic writing. His ideas and comments during my research were very valuable.

I want to greatly thank Dr. Saeed Sharif for supervising in my first two years. His support, tutorship, and his advice helped me to overcome many difficulties.

A special thanks of appreciation to my family for their endless support, trust, love, patience, and their encouragement.

I am very grateful to my best friend Hend Eissa. Her existence in my life has strengthened me. Also, I want to thank my kind friends; Ahmad Al-Dahoud, Lubna Kwuaileh, Jamil Razzak, and Zahera Mohammad and her family for their encouragement and motivation.

Many people have offered me great help in my personal life and academic matters especially during my first year. Their input made a big difference. I want to mention them in particular: Niaz Jalal, Omar Thalji, Mohammad Alomari, Ola Younis, Sofyan Hayajneh and Diala Bdour.

My colleagues in the Faculty were very supportive and cooperative. I want to thank them all, especially Zahra Sayed, Shumoos Taha, and Alaa Nassar.

Finally, I am very thankful and grateful for the ophthalmologists at the Manchester Royal Eye Hospital; Dr Arun Brahma, Dr Andrew Walkden, and Dr Jaya Chidambaram. They were very collaborative and helpful in enriching my medical background about the cornea.

Table of Contents

Table of Contents

List of Figures

List of Tables

List of Abbreviations

IVCM: In Vivo Confocal Microscopy

SNP: Sub-Basal Nerve Plexus

TSCM : Tandem Scanning Confocal Microscopy

SSCM: Slit Scanning Confocal Microscopy

LSCM: Laser Scanning Confocal Microscopy

HRT: Heidelberg Retina Tomograph

AK: Acanthamoeba Keratitis

RCM: Rostock Cornea Module

HSV: Herpes Simplex Virus

ICE: IridoCorneal Endothelial

PCR: Polymerase Chain Reaction

PK: Penetrating Keratoplasty

PPCD: Posterior Polymorphous Corneal Dystrophy

DPN: Diabetic Peripheral Neuropathy

GUI: Graphical User Interface

SIFT: Scale Invariant Feature Transform

DoG: Differences of Gaussian

CLAHE: Contrast-Limited Adaptive Histogram Equalisation

CED: Coherence-Enhancing Diffusion

EED: Edge-Enhancing Diffusion

List of Publications

Journal papers

1. Alzubaidi R, Sharif MS, Qahwaji R, Ipson S, Brahma A: **In vivo confocal microscopic corneal images in health and disease with an emphasis on extracting features and visual signatures for corneal diseases: a review study**. *British Journal of Ophthalmology* 2015.
2. Sharif MS, Qahwaji R, Shahamatnia E, Alzubaidi R, Ipson S, Brahma A: **An efficient intelligent analysis system for confocal corneal endothelium images**. *Computer methods and programs in biomedicine* 2015, **122**(3):421-436.

Conference paper

1. Sharif MS, Qahwaji R, Hayajneh S, Ipson S, Alzubaidi R, Brahma A: **An efficient system for preprocessing confocal corneal images for subsequent analysis**. In: *Computational Intelligence (UKCI), 2014 14th UK Workshop on: 8-10 Sept*; 2014: 1-8.

Posters

1. Alzubaidi R, Qahwaji R, Ipson S, Brahma A: **Fully automated system for detection single and double wall corneal acanthamoeba cysts using confocal microscopy images**. *Poster session presented at the Digital Health and Well being Festival 2016, Bradford, UK*.
2. Alzubaidi R, Qahwaji R, Ipson S, Brahma A, Walkden A: **Medical Imaging: Development of automated diagnostic system for corneal abnormalities of Acanthamoeba keratitis**. *Poster session presented at the 1st Annual Innovative Engineering Research Conference (aierc2017)*, *University of Bradford, UK*.

1. Introduction

1.1. Overview

In vivo confocal microscopy is a non-invasive, repeated, rapid, and high-resolution imaging technique which is helpful in evaluating the morphological characteristics of corneal abnormalities at the histological level and may be useful in diagnosis, determination of progression and understanding the pathophysiology of eye disease. The entire corneal volume can be accessed for in vivo imaging by the confocal microscopy technique. The acquired images show the cell structures in different corneal layers, with typical minimum depth separation of about 2-5 μm.

Infectious keratitis which is mostly associated with lens wearers is a sight-threatening infection. The value of IVCM method has been demonstrated in the diagnosis and management of Acanthamoeba and fungal keratitis where fungal filaments (hyphae) and Acanthamoeba cysts can be immediately detected, allowing clinician to promptly start the appropriate antimicrobial therapy.

The existing of an automated analysis system for patient confocal images makes the process of the diagnosis faster, more accurate, and more objective. The automated analysis of the quantitative parameters for cysts and filaments can be very helpful in studying the correlation of quantitative evaluation of these cysts and filaments with clinical staging of disease. It also aids in evaluating the effectiveness of treatment and the healing of the cornea in the follow-up of infectious keratitis patients.

1.2. The cornea: definition, function, and structure

The cornea is the eye's outermost layer. It is the transparent, dome shaped surface that covers the front of the eye and the area of this surface is approximately 1.3 cm^2. The cornea is an avascular tissue, which seems to lack substance but it is highly organized tissue containing proteins, fibrils and various corneal cells. The corneal cells receive their oxygen and nutrients via diffusion from the surrounding environment: tear fluid and aqueous humour that fills the chamber behind it. [1-6]

The cornea acts as a barrier against dirt, germs, dust, and other harmful matter. The cornea contributes in this protective task cooperatively with the eyelids, eye sockets, tears, and the sclera (white part of the eye). Also, the cornea and lens of the eye play a key role in vision by helping focus light on the retina, which is the light sensitive tissue at the back of the eye. When light strikes the cornea, it bends or refracts that incoming light onto the lens which in turn refocuses that light onto the retina. The retina starts the translation of light into vision by converting light into electrical impulses which travel through the optic nerve to the brain, which interprets them as images. The cornea is responsible for 65-75% of the eye's total focusing power. Furthermore, the cornea serves as a filter; it screens out damaging ultraviolet light from sunlight, which would otherwise expose the lens and the retina to injury [4, 6].

The cornea curvature is 43 dioptres, equating to a radius of curvature of the anterior surface of 7.8 mm and 6.5 mm of the posterior surface. The normal mean corneal diameter on its anterior surface measures 11.7 mm horizontally and 10.6 mm vertically. The cornea is thinnest centrally and gradually increases

in thickness towards the periphery with an approximate mean value of 0.5 mm and 0.7 mm respectively [1, 3].

In the histological cross-section, the normal cornea consists of five distinct layers. The corneal epithelium lies at the anterior side and is 38-53 μm thick at the central corneal region. Bowman's layer lies under the epithelium with a thickness of 10–16 μm and it is acellular except for the nerves that permeate it. Bowman's layer separates the epithelium from the stroma. The stromal region constitutes approximately 90% of the total corneal volume and its thickness ranges between approximately 450 and 550 μm. It contains large nerves, stromal keratocytes and orthogonal layers of collagen fibres. An acellular layer called Descemet's membrane lies posterior to the stroma. It is about 15–20 μm in thickness. The limiting layer on the posterior surface of the cornea is a single layer of corneal endothelial cells which has an approximate thickness of 4-6 μm [1, 3, 5, 7]. Figure 1.1 shows the anatomy of the human eye (at the top) and the corneal five layers in histological cross-section of a normal human cornea (at the bottom).

The corneal epithelium is arranged approximately in four layers of cells. ***Superficial epithelial cells*** present a polygonal cell pattern which has a size of up to 50 μm in diameter and about 5 μm in thickness. These cells have reflective nuclei with bright illuminated cytoplasm and perinuclear dark halos. Generally, superficial epithelial cells have light cell boundaries and bright visible nuclei [7]. ***Wing cells*** are an epithelial intermediate layer which forms a regular mosaic with reflecting and sharp cellular borders. These cells (which are regular in form) have a size of about 20 μm, and can also be subdivided into upper and lower wing cells; the latter smaller. Wing cells are characterised by bright cell

borders and a bright cell nucleus (which is usually not visible) with few organelles [7]. ***Basal epithelial cells*** form a regular mosaic that has dark cell bodies with light, narrow intercellular reflecting borders, and a small diameter ranging between 8 and 10 µm. These cells show only cell borders without nuclei reflectivity [7]. ***The sub-basal nerve plexus*** (SNP) is characterised by the appearance of bright, well-defined long linear nerve fibre bundles, frequently demonstrating branches or anastomosis. These nerves range between 4 and 8 µm in length and are organised in a vortex pattern in the lower quadrant of the paracentral cornea. SNP may be identified in Bowman's layer [7]. ***Bowman's membrane*** is an acellular hyper-reflective structure with a thickness of 10-16 µm. It appears as an amorphous layer when viewed with confocal microscopy and consists of randomly arranged collagen fibrils located in between the basal cells and the stroma [7]. ***The corneal stroma*** which forms around 80-90% of the whole corneal volume has keratocytes that appear as hyper-reflective cell nuclei, typically forming clusters, with poorly visualised cell processes. The corneal stroma composes of three main histological constituents: cellular, acellular and neurosensorial. The connective lamellae appear black (i.e., transparent), whereas the keratocyte nuclei are visible as egg-shaped light reflecting corpuscles. Using cross sections to analyse keratocyte density, which is measured in cells/mm2, density is largest immediately under Bowman's membrane (in the anterior stroma), and it is reported to be around 500-1300 cells/mm2. Towards the central stroma, the density declines sharply (minimum 65 cells/mm2), and it increases again slightly in the posterior stroma where it is reported to be around 250-900 cells/mm2. It is mentioned that keratocyte density seems to decrease with age in a rate of 0.45% per year and appears to be independent of sex [7]. ***Descemet's membrane*** is rather difficult to see

using confocal microscopy under normal circumstances particularly in younger subjects and it appears as an acellular layer between the posterior stroma and the endothelium. It is thin with a thickness of about 6-10 µm and with no nerve plexus [7]. ***The corneal endothelium*** is located immediately posterior to Descemet's membrane and is easy to recognise because of its clearly identifiable structure of cells characterised by a hyper-reflective, regular hexagonal pattern, and surrounded by hypo-reflective borders without obvious nuclei reflections [7].

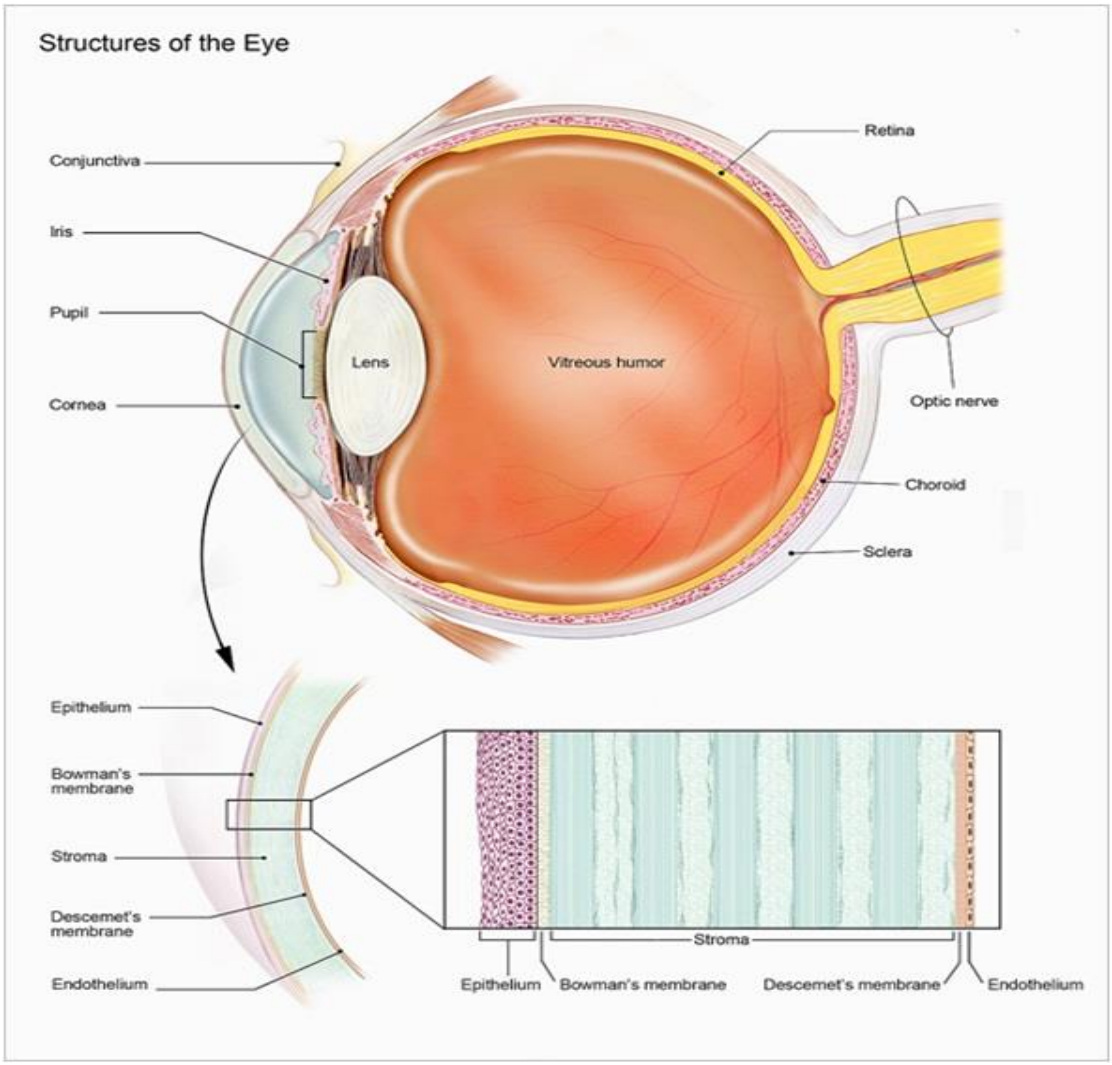

Figure 1.1 An anatomy of the human eye (at the top) and a histological cross-section of a normal human cornea demonstrating its five layers (at the bottom) [4].

1.3. In vivo confocal microscopy (IVCM)

The confocal microscope was originally developed by Marvin Minsky in the mid-1950s. The instrument he constructed, which focused the light on a small area of tissue, was called the ‘double focusing stage scanning microscope’ and was patented in 1957. The term ‘confocal’ came from the principle of the illumination and observation pathways that have a common focal point [7]. After Minsky’s work, a multiple-beam confocal microscope for examining unstained brain sections and ganglion cells was created in the late 1960s by M. David Egger and Mojmir Petran. Egger continued in this arena; he developed the first mechanically scanned confocal laser microscope, and in 1973, he published the first recognisable images of cells produced by this technique. During the late 1970s and the 1980s, a growing interest in confocal microscopy developed Because of the advances in computer and laser technology coupled to new algorithms for digital manipulation of images [7]. The practical laser scanning confocal microscope designs were translated to working instrument by several investigators. In 1979, Dutch physicist G. Fred Brakenhoff developed a scanning confocal microscope, while at almost the same time Colin Sheppard contributed to the technique with a theory of image formation. The concept was nurtured by Tony Wilson, Brad Amos and John White and later (in the late 1980s) they demonstrated the utility of confocal imaging in the examination of fluorescent biological specimens [7].

There are three main types of confocal microscopy: tandem scanning confocal microscopy (TSCM), slit scanning confocal microscopy (SSCM) and laser scanning confocal microscopy (LSCM). Petran and Hadravsky developed the first real-time TSCM by using point illumination and detection. Nipkow

modified the basic part of the system and he invented a spinning disc composed of sets of conjugate pinholes arranged in spirals. A two-dimensional image is generated after a specimen is scanned. The pinholes need to be as small as possible to eliminate most of the scattered light. However, this results in very low light throughput (only 0.25-1% of light reaches the cornea), which requires a high-intensity light source and a low-light-level camera to enable image acquisition. The Tandem Scanning Corporation (Reston, Virginia, USA) produced this original microscope in its clinical version and later by the Advanced Scanning Corporation (New Orleans, Louisiana, USA), but it is no longer in production [7]. The SSCM was first developed by Thaer for observing the in vivo cornea as an alternative to point scanning. This involves illumination from a slit of scanned over the back focal plane of the microscope objective which consequently allows greatly reduces scanning times over the TSCM where all points on the axis of the slit can be scanned at the same time. The slit illumination also allows a greater light throughput than the TSCM and thus allows longer examination times because a lower intensity light source may be used [7]. Contrast with the SSCM is greater in comparison to the TSCM, which enables imaging of the low reflecting layer of wing cells in the epithelium and provides clearer images of the stroma. The slit height may be adjustable, which would allow the user to control the amount of light throughput and the thickness of the optical section. However, the microscope is only truly confocal in the axis perpendicular to the slit and provides lower axial and transverse resolution than the TSCM [7]. Slit scanning in vivo confocal microscopes are provided from many commercial sources such as Tomey Corporation (Cambridge, Massachusetts, USA), Nidek Technologies (Gamagori, Japan) and Helmut Hund (Wetzlar, Germany) [7]. The LSCM which employs a coherent laser as a

high-intensity light source was developed by Webb. The laser beam is scanned using a set of galvanometer scanning mirrors, which provides fast scanning over the x-, y-plane. The reflected light refocused by the microscope objective is rescanned by the galvanometer scanning mirrors and imaged onto a pinhole aperture located in front of a photomultiplier. The Heidelberg Retina Tomograph (HRT) (Heidelberg Engineering, Heidelberg, Germany) is one of the well-established in vivo confocal imaging systems used in ophthalmology. HRT is a device that was designed to acquire and evaluate topographic measurements of the optic nerve head to detect glaucomatous damage using a 670 mm diode laser. The University of Rostock (Germany) modified the HRT to use a detachable objective system called the 'Rostock Cornea Module' (RCM). This helps in converting it into a high-resolution LSCM for the visualisation of the anterior segment of the eye. Because of the high-depth resolution of LSCM, optical sections of only a few micrometres can be imaged with a high contrast and precisely measured. LSCM provides greater contrast than the TSCM or SSCM.

Niederer and McGhee mentioned that the data existing for comparisons of performance between the different types of in vivo confocal microscopy are limited [7, 8]. A comparison between keratocyte density measured with TSCM and SSCM (Confoscan 3) demonstrated that comparable measurements of keratocyte cell density were achievable between the two devices, providing the effective depth of the sample volume is taken into consideration. A further qualitative study compared the appearance of the central cornea in normal subjects and in subjects with corneal dystrophy between SSCM (Confoscan 2) and LSCM (HRT II RCM). The observed morphology was similar with the two devices, but image contrast appeared greater with the LSCM. A comparison

between SSCM (Confoscan 3) and LSCM (HRT II RCM) [7] to measure endothelial cell density has been conducted and all the cell density results (for patients and normal subjects) that were measured with the RCM were higher than those with the Confoscan 3. Measurements of cell density and image contrast with contemporary SSCM (Confoscan 4, NIDEK, Gamagori, Japan) and LSCM (HRT II RCM) have been compared. At the levels of the basal epithelium and the endothelium, good agreement between the two devices for cell density measurement has been observed. Mid-stromal keratocyte density (measured in cells/mm2) was approximately double with SSCM in comparison with LSCM, presumably due to differences in optical section thickness [7]. It has been observed as well that the contrast at the level of the mid-stroma was greater with the LSCM compared with the SSCM and the contrast levels were consistent over the whole image, whereas there was a loss of image quality towards the edges of the SSCM image. Poor agreement was observed in the measurement of sub-basal nerve plexus (SNP) density, probably due to differences in image contrast, with values measured with LSCM greater than those measured with SSCM [7]. It has been observed that SNP density measured with SSCM was two to three times higher than density measured with TSCM [7].

Using the HRT-RCM laser-scanning system, which is used to obtain the dataset of this research, IVCM examination consists of one or several scans (each lasting from 3.3 to 100 sec, depending on the acquisition rate), where each scan consists of 100 consecutive images acquired at a selectable rate from 1 to 30 frames/sec. The entire corneal volume can be accessed for in vivo imaging since a depth range of approximately 1200 µm is available while human corneal thickness is typically 550µm [9]. The acquired images show the

cell structures in different corneal layers, with typical minimum depth separation of about 2-5 μm [6]. Furthermore, the images acquired represent a field of view of either 300 × 300μm or 400 × 400μm, depending on the choice of the internal field lens. The axial resolution is about 4 μm, while the lateral resolution is about 1-2 μm [9]. Figure 1.2 shows the corneal examination using IVCM [10].

Figure 1.2 Examination by confocal microscope [10].

IVCM is considered a non-invasive imaging technique that allows acquisition of high-resolution images of all the corneal layers. Since accurate and rapid diagnosis is significant for the management and outcome of infectious keratitis, diagnosis of infectious keratitis constitutes one of the most important clinical uses of IVCM [11].

1.4. Visual signatures of corneal diseases

1.4.1 Overview

Corneal pathologies can be classified according to which corneal layer is affected and in this case, corneal diseases lie in four groups: epithelial and sub-epithelial dystrophies, Bowman layer dystrophies, stromal dystrophies, and Descemet's membrane and endothelial dystrophies. Each corneal disease creates in the corneal layers in the eyes of patients significant qualitative and/or quantitative alterations. In other words, any defect occurring in the cornea has

its own signs relative to the involved layer. Qualitative alterations relate to changes in the morphology of the corneal layer, while quantitative alterations relate to changes in measurements such as cell diameter, cell density, the total number of nerves within a frame, nerve length, keratocytes density, corneal reflectivity and corneal thickness, and number of cells within a frame [7]. Two examples on each layer are summarised in Section 1.3.2. More details can be obtained from [7], where the most common corneal diseases and their visual signatures are identified. Moreover, images of the diseases were analysed to extract their features in terms of intensity, region of interest and contained shapes with both their sizes and diffusion [7].

1.4.2 Corneal layers in disease

Epithelial and subepithelial: 1) Amiodarone-induced keratopathy. This is characterised by bright intracellular, highly reflective inclusions appearing in the corneal epithelial cells (see Figure 1.3A). Other corneal layers may be involved in more advanced cases; bright microdots arise within the anterior and posterior stroma as shown in Figure 1.3B and these microdots could reach the endothelial cell layer. 2) Viral keratitis: Herpes Simplex Virus (HSV). HSV infection is usually followed by an inflammatory response, which can seriously damage all corneal layers. As indicated in Figure 1.3C, the superficial epithelium layer shows an increase in cell size and hyper-reflectivity while there is a lowering in cell density. Some patients with HSV infection have variations of the SNP. **Bowman's layer:** 1) Reis–Bückler's dystrophy. This shows focal deposition of homogeneous, reflective material, as indicated by arrows in Figure 1.3 D, interspersed with the basal epithelial cells. The dystrophy shows also

highly reflective material at the level of Bowman's layer as indicated by an asterisk in Figure 1.3 E.

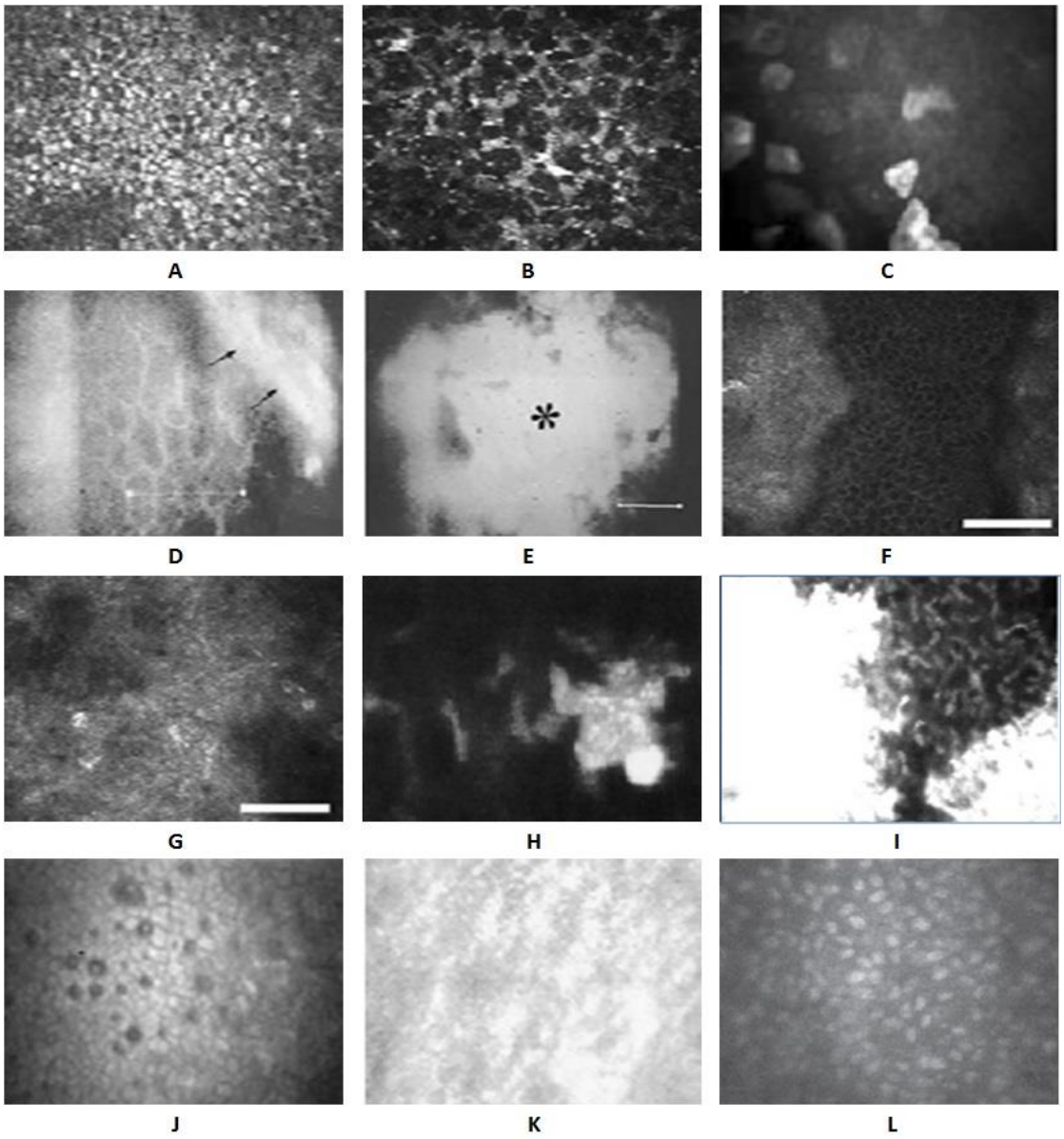

Figure 1.3 Examples of corneal diseases [7]. A) Basal cell layer clearly showing hyper-reflective cell inclusions. B) The increase in the number of microdots between the keratocyte nuclei in anterior stroma with the period of amiodarone ingestion. C) Increase in cell size and hyper-reflectivity while there is a decrease in cell density. D) Deposition of homogeneous, reflective material (arrows) interspersed with the basal epithelial cells. E) Highly reflective material (asterisk) at the level of Bowman's layer. F) Deposits with homogeneous reflectivity, rounded edges and dark shadows in the basal epithelium. G) The homogeneous reflective materials completely replaced Bowman's layer. H) hyper-reflective and largely intracellular dots distributed throughout stroma, and a cluster of these hyper-reflective dots enclosed in cyst-like structures. I) Clusters of highly reflective granular materials with irregular edges at the level of the superficial and middle stroma. J) Roundish hypo-reflective areas of varying size surrounded by hyper-reflective endothelial cells. K) Descemet's membrane displays significant fibrosis. L) epithelium-like transformation with prominent bright nuclei, and with irregular and indistinct borders.

2) Thiel–Behnke dystrophy. This disease shows deposits of homogenous reflectivity, rounded edges and dark shadows in the basal epithelium, as indicated in Figure 1.3 F. Bowman's layer is completely replaced as indicated in Figure 1.3G. **Stromal:** 1) Fleck dystrophy. In this dystrophy, various shapes of hyper-reflective and largely intracellular dots are distributed throughout the corneal stroma. They are sometimes enclosed in cyst-like structures with diameters of 3–5 μm as indicated in Figure 1.3H. 2) Avellino corneal dystrophy. This shows clusters of highly reflective granular materials with irregular edges at the level of the superficial and middle stroma as appearing in Figure 1.3I. **Descemet's membrane and endothelial:** 1) Fuchs' endothelial dystrophy (Cornea guttata). At the level of the endothelium, corneal guttae appear as roundish hypo-reflective areas of varying size with central bright spots and surrounded by hyper-reflective endothelial cells (see Figure 1.3J). Significant fibrosis appears in Descemet's membrane as shown in Figure 1.3K. 2) Iridocorneal endothelial syndrome. In iridocorneal endothelial (ICE) syndrome, endothelial cells appear as an epithelioid-like cell with irregular borders and non-homogenous, diversely shaped prominent bright nuclei as shown in Figure 1.3L.

1.5 Importance of this research and technical challenges

This research deals with confocal microscope images of infectious keratitis, especially Acanthamoeba keratitis and fungal keratitis (Fusarium). This research gains its clinical importance firstly, from the seriousness and danger of these diseases on eyesight, and secondly, from the using of confocal microscope images in diagnosing the infection. Infectious keratitis is the main reason for ocular morbidity in developing countries. The early diagnosis or even

a strong suspicion of the disease, if leading to effective treatment, may improve the outcome of infectious keratitis. IVCM has demonstrated its value for the diagnosis and management of Acanthamoeba and fungal keratitis [12].

The incidence of Acanthamoeba keratitis (AK) is still relatively rare, but a rise in the number of cases of the disease has been noticed. This may vary between regions, contact lens practices, and the methods used for diagnosis [11, 12]. A leaflet produced by Moorfields eye hospital in 2015 demonstrated that around 85% of cases of AK have been associated with contact lens wear [13]. In the United Kingdom, Europe, Hong Kong, and the USA, it is estimated they have an infection rate of 1.2 per million adults and between 0.2 and 1 per 10,000 contact lens wearers per year [11]. In developed countries, where the most common risk factor is contact lenses, the infection rate is about 1 per 10,000 contact lens wearers per year. In India, it has been reported that Acanthamoeba keratitis forms 1.0-2.4% of all culture positive corneal ulcerations [12]. Acanthamoeba keratitis is a serious, sight-threatening infection of the cornea that can lead to irreversible complications and even blindness [14]. However, blindness due to Acanthamoeba keratitis can be prevented unless a significant delay in diagnostic occurs, which is considered a major factor that may lead to blindness in 15% of untreated cases [15].

Fungal keratitis is one of the most common infectious keratopathy in Asia and Africa. During the past decade, the incidence of fungal keratitis has increased in China [16, 17]. According to the US Centres for Disease Control and Prevention, it becomes a public health concern in developed countries, with a recent rise in Fusarium keratitis infections associated with extended wear of contact lenses [18]. Fungal keratitis is considered as a major ophthalmological

problem in agriculture-based geographical regions with humid, hot, tropical and subtropical climates. A high prevalence of fungal keratitis has been noticed in Asia especially in South India, China, Bangladesh, and Nepal and also in Ghana and South Florida, where filamentous fungi are implicated as major pathogens [11, 18] and the cause of more than 60% of fungal corneal ulcers with Fusarium being one of the most predominant species [19]. On the other hand, the incidence of fungal keratitis in regions with temperate climates such as Britain, France and the Northern US remains low [11, 18]. However, fungal keratitis, which is a common cause of corneal infection and blindness after trauma in the developing countries, is frequently caused by Fusarium species [20]. It is becoming a public health problem in industrialised countries as well and it is increasing in frequency according to the Centres for Disease Control and Prevention [11, 18].

Making an accurate and early clinical diagnosis of infectious keratitis and then determining the possible cause are critical for successful therapy [11, 12]. However, it remains a challenge for the ophthalmologist to get an accurate and rapid identification of the infectious agent involved [11].

Many traditional corneal diagnostic methods are available. The principal diagnostic tool in clinical ophthalmology is the slit lamp, while corneal cultures are considered to be the gold standard diagnostic tool for infectious keratitis [11]. The slit lamp with approximately 40 times magnification could narrow its usefulness in the diagnosis of microbial keratitis. The infective organisms cannot be seen directly, so indirect criteria should be used initially to differentiate etiologies. However, differentiating the major forms of infectious keratitis is challenging where characteristic clinical signs may not be present in

all cases. Microorganisms need time to be detected using corneal cultures and smears and they may not be detected because of inadequate sample material, delay in performing the investigations, deeply seated lesions, and previous use of empirical antimicrobial treatments [11].

Clinicians are often forced to use empirical therapy with broad spectrum antibiotics or combination therapy that may increase the delay in healing keratitis because of the lack of microbiology facilities and the time required for definitive identification of the causative agent by microbiologic techniques. In such cases, reliable and accurate methods to identify the causative organism would tighten the differential diagnosis and facilitate proper therapy. Furthermore, situations presenting with deep stromal lesions often require invasive and potentially risky procedures like a corneal biopsy to obtain a microbiologic diagnosis [11, 12]. Thus, as an important method for the early diagnosis of various corneal conditions; confocal microscopy is fast emerging. It provides high-resolution images with magnifications of up to X1000 [17], and it allows details to be visualized even in hazy corneas. It is a non-invasive tool which makes it an important modality in the rapid diagnosis of fungal and Acanthamoeba keratitis. It can be used to make rapid and repeated observations, which will help in managing the disease by providing early diagnosis so that treatment may be initiated earlier. It also aids follow-up of infectious keratitis patients and evaluating the effectiveness of the treatment [11, 12].

Clinicians use confocal microscopy in conjunction with the traditional methods and sometimes they need to use it to overcome the limits of traditional methods. The signs of infectious keratitis (affected areas) need to be detected

first and then need to be tracked in the sequence of images that are captured from different depths of the patient's cornea. Manual detection and tracking of those signs in confocal images, and thus the derived clinical parameter values are subjective, time-consuming and error-prone. Therefore, there is a strong need for a reliable automatic tool that provides a much easier, objective and clinically rapid usable procedure which is capable of extracting those signatures and their quantitative analysis. The crucial need for this automatic tool which was developed in this work, gives this research its technical importance.

Confocal microscope images of infectious keratitis can present a technical challenge since they suffer from many problems that necessitate processing. These problems begin with the quality of the image; the appearance of haze and other artefacts can be noticed. Therefore, the images need to be improved by pre-processing. Then, there is a need to isolate (segment) the affected regions from the background, and thus further processing can be done. The segmentation stage is a real challenge especially when the affected areas are blurry and connected to each other, or are confused with other structures such as inflammatory cells or cells of the involved layer (e.g. epithelial cells, or stromal keratocytes). An ophthalmologist cannot make decisions from just one image; there is a need to get an estimation of the depth of infection in all captured images along the whole cornea. To get the depth of the infection, there is a need to align the ordered images on top of each other. This means, firstly, an efficient registration technique is required and secondly, an effective tracking method is needed.

1.6 The dataset

The work was conducted in collaboration with the NHS specifically with the corneal consultants Dr Arun Brahma, Dr Andrew Walkden, and Dr Jaya Chidambaram who are working in the department of ophthalmology of the Manchester Royal Eye Hospital, Manchester, UK.

The consultants provided normal corneal images and abnormal corneal images for patients with infectious keratitis. The abnormal images distributed over Acanthamoeba keratitis and Fusarium. The total number of Fusarium images was 39 of one patient; 22 of them were informative while the others were very bright or with no data, as shown in Figure 1.4, so they were excluded. Hundreds of Acanthamoeba infectious images were provided. Unfortunately, most of these images were non-informative or were taken at the stromal level (see Figure 1.5).

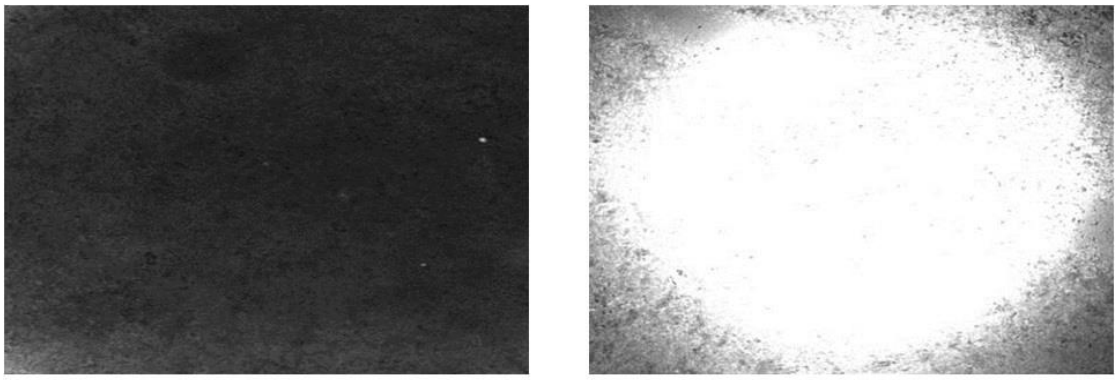

Figure 1.4 Example of excluded images from Fusarium dataset. A) Non-informative image (dark). B) Non-informative image (very bright).

Stromal images were excluded as well because Acanthamoeba usually affects the epithelial layer and even if it reaches stroma, which only happens in advanced cases, the developed system is not capable of distinguishing

between Acanthamoeba cysts and stromal keratocytes, since keratocytes have the same appearance as cysts.

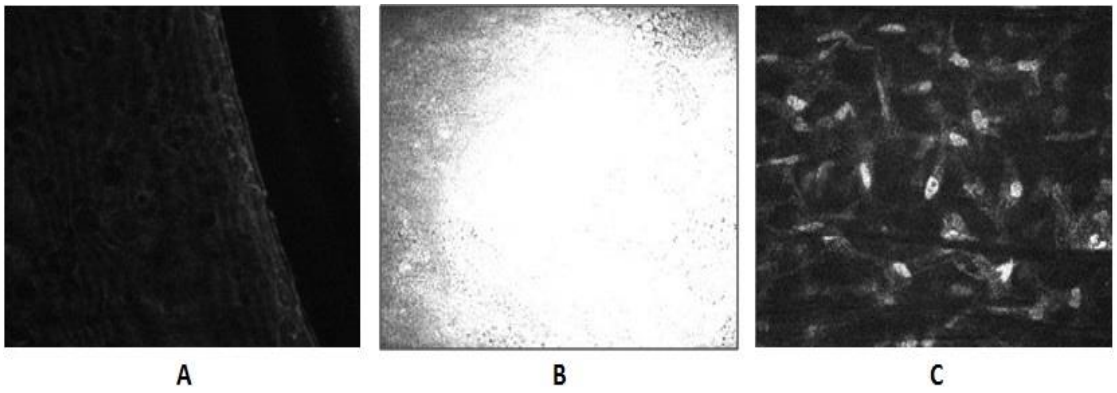

Figure 1.5 Example of excluded images from Acanthamoeba dataset. A) Non-informative image (dark). B) Non-informative image (very bright). C) Stromal layer image.

The images of interest of Acanthamoeba that have been worked on were 54 images from 13 patients. Each patient has an ordered sequence of images ranging in number from 3 to 7. The total number of the normal images was 40 of one subject. The normal images were taken for basal epithelial cells, sub-basal nerve plexus, and stroma. Only 8 images out of 40, which cover the basal epithelial cells, were picked. These ones were used in the evaluation of segmentation process of Acanthamoeba signs as explained in Section 3.5. All images in the dataset are LSCM images captured with an HRT3-RCM (Heidelberg Engineering, Heidelberg, Germany) with a field of view of 400×400 µm, the lateral resolution of 1µm, set at 800 times magnification, and image size 382×382 pixels and are saved in JPEG format.

1.7 Aims and objectives

The aim of this research is to work towards the development of an automatic corneal diagnostic system which can help the ophthalmologists in diagnosing the corneal abnormalities by detecting the visual signs of the disease and then extracting the main quantitative features using the IVCM images of that disease. The system could help as well to get an early diagnosis of the corneal diseases by drawing attention to affected areas and therefore avoiding any delay in treatment. It is also useful to evaluate the patient's condition after treatment by comparing the features of the disease in the confocal images for the patient before and after therapy. The system offers clinicians a graphical user-interface through which they process patient's confocal images. Also, the useful measurements that are computed for the detected cysts are saved in a separate file automatically to be used later.

The following objectives have been addressed to work towards the achievement of the overall aim.

- Creating a knowledge base of visual signatures for common corneal diseases that identifies the visual appearance of each disease in the confocal microscope images.
- Enhancing the corneal confocal images which suffer from haze, blur, and appearance of some artefacts by applying proper image processing techniques.
- Detecting the regions of interest (visual signs of the disease) and isolating them from the background by developing an efficient segmentation method.

- Extracting quantitative features that describe the regions of interest and thus help clinicians in gaining more knowledge about the disease.
- Tackling the displacement of an ordered sequence of images in a particular scan for an Acanthamoeba keratitis patient eye, which is mostly caused by breathing, cardiac pulse, and eye movement. A normalised efficient registration technique is used in this work to align the images on top of each other.
- Tracking the detected regions of interest (Acanthamoeba cysts) in an ordered sequence of images in a particular scan for a patient eye, and hence get the depth of each cyst. The tracking process uses an estimated geometric transform on the segmented sequence of images and that geometric transform is obtained by applying registration on the original sequence of images.

Incidences of Fusarium in the UK are less frequent than Acanthamoeba keratitis [11, 18]. Therefore, only 22 informative images of Fusarium for one patient have been obtained. Consequently, after segmentation, only a colour mapping is applied on the detected hyphae in each image whereas registration is applied on the Acanthamoeba images and then Acanthamoeba cysts that are detected after segmentation are tracked in a sequence of images.

The overall strategy proposed to colour map and track Acanthamoeba cysts and to colour map Fusarium hyphae is demonstrated in Figure 1.6.

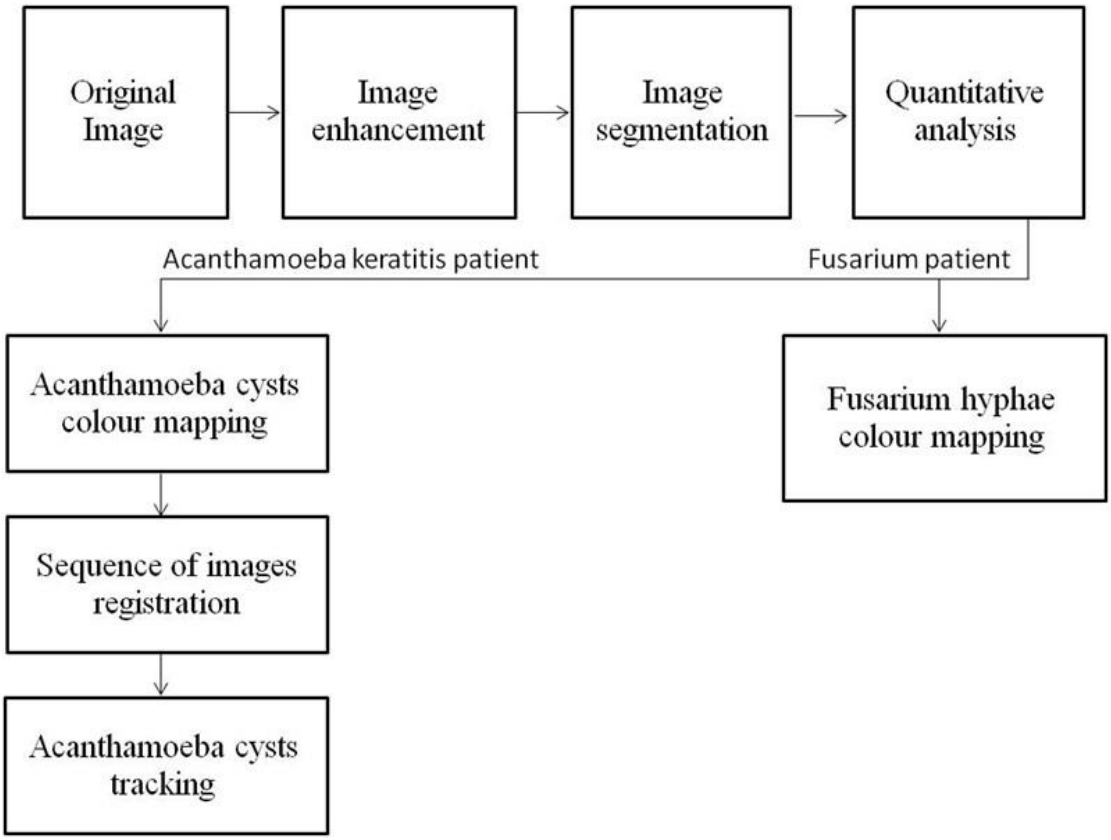

Figure 1.6 The overall strategy proposed to colour map and track Acanthamoeba cysts and to colour map Fusarium hyphae.

1.8 Outline of the thesis

The remainder of the thesis is organised into six chapters. Chapter two is a review of medical and technical literature for Acanthamoeba keratitis and fungal keratitis (Fusarium). It shows the signature of these diseases and any automated attempts to diagnose them. It also indicates gaps in knowledge that this research tries to tackle. Chapters three and four are dedicated to the system that has been developed to diagnosis Acanthamoeba keratitis using confocal images. The proposed approach of Acanthamoeba images enhancement and Acanthamoeba cysts segmentation is explained in detail in Chapter three, while the normalised adopted registration technique that is used to align Acanthamoeba sequence of images and then tracks the segmented

cysts and computes their quantitative parameters over the sequence of registered images is demonstrated in Chapter four. The proposed approach for Fusarium diagnosis appears in Chapter five. It shows the normalised techniques adopted to enhance Fusarium images, and then to detect the Fusarium hyphae and isolate them from the background. Lastly, it clarifies the standard measurements that could be useful in diagnosing fungal keratitis. The conclusions and suggestions for future work are presented in Chapter six.

2. Literature Review

2.1. Introduction

The early diagnosis of infectious keratitis is of major importance to avoid any delay in appropriate treatment which in turn could cause detrimental effects on the best visual outcome. A detailed clinical search for specific signs is usually made through examination of corneal smear and culture which remains the gold standard. However, culture often takes three or more days to provide definite results. The diagnostic interval has substantially reduced since the introduction of a new molecular technique called polymerase chain reaction (PCR) which takes only one day before results become available, and the IVCM which has the potential to identify Acanthamoeba and fungal keratitis immediately [2, 11]. Although PCR has been shown to be useful in the diagnosis of fungal and amoebic keratitis, it is not strongly reliable as this technique is expensive, not available in all laboratories and for all infectious microorganisms and its exact capability as a diagnostic tool has still not to be determined, more details about PCR can be found in ref. [11].

Since the introduction of IVCM of the cornea, interest for this technique has increased constantly. Initially, many case-reports appeared which document the cellular morphology in rare corneal disorders. Later on, the main focus switched to larger case-series with quantitative assessment in normal and diseased corneas. IVCM has already proven its value as a research tool, therefore, the logical next step would be to put this technique into daily ophthalmic practice [2].

In this chapter, medical and technical reviews for infectious keratitis using IVCM are discussed, highlighting the knowledge gaps that have been tackled by this research.

2.2. Medical review of Acanthamoeba keratitis and fungal keratitis (Fusarium)

Acanthamoeba is a ubiquitous protozoan living in water, air, and soil with a lifecycle consisting of two stages: active motile trophozoites and dormant cysts. Cysts have a single or a double wall containing cellulose and are resistant to many chemical agents which make them harder to treat than other microbes [2, 11, 21, 22]. The most common risk factor for Acanthamoeba is contact lens wear, especially in unhygienic circumstances like swimming while wearing contact lenses, the use of non-sterile lens solutions, and insufficient disinfection practices [2, 11, 13, 21, 22]. Other risk factors for Acanthamoeba are associated with a poor water supply and a history of eye trauma and previous ocular diseases [21, 22].

The first experimental use of IVCM images to visualise amoebic cysts and trophozoites were reported by Chew et al. in 1992 using TSCM on a corneal button excised by penetrating keratoplasty (PK) and in another report on a pig cornea infected with Acanthamoeba castellanii produced in 1993 by Cavanagh et al. A year later, Auran et al. reported the first in vivo images utilising SSCM showing Acanthamoeba cysts in the anterior stroma of a patient with Acanthamoeba keratitis confirmed by a corneal biopsy [1, 11]. Since then, the use of IVCM as a non-invasive tool has been described in many publications not only to diagnose Acanthamoeba keratitis but also to observe the progression and response to antimicrobial treatment.

IVCM was used to diagnose 61 out of 63 cases of suspected Acanthamoeba Keratitis by Parmar et al. [11, 23]. In a study of 133 eyes with infectious keratitis, Kanavi et al. used IVCM and found 100% sensitivity and 84% specificity in diagnosing Acanthamoeba Keratitis, compared to results from corneal or contact lens case scrapings in many microbiologic studies [11, 24]. Tu et al. used SSCM in 125 patients suspected to have Acanthamoeba Keratitis and used multi-test reference standards to evaluate the diagnostic value of IVCM more precisely. They supported the utilisation of IVCM as a diagnostic tool for Acanthamoeba Keratitis when they reported IVCM diagnostic tests with sensitivity ranging from 90.6% to 92.9%, and specificity ranging from 77.3% to 100% [11, 25]. Matsumoto et al. revealed that trophozoites and cysts disappeared 4–6 weeks after treatment using a repetitive IVCM examination of patients with Acanthamoeba keratitis [11, 26]. The treatment of combined fungal and Acanthamoeba keratitis has been monitored using IVCM by Babu et al. [11, 27]. Diagnostic accuracy of Acanthamoeba keratitis has been studied more recently, when Hau et al. in 2010 used a laser confocal system and achieved a wider range of accuracy, with a much lower sensitivity (less than 56%) and with specificity up to 84.2% [2, 21, 28]. Vaddavalli et al. in 2011 achieved higher values of sensitivity (88.3%) and specificity (91.1%) [12, 21].

The signs of Acanthamoeba keratitis that can be shown by IVCM are cysts and, to a lesser extent, trophozoites [2, 11, 26, 27]. Other signs are rare but have been mentioned in a few cases finding Acanthamoeba keratitis using IVCM; radial keratoneuritis, modifications in the corneal stroma that appeared at the late-stage of the disease, and hyper-reflective inflammatory cells [11].

The cysts, which are the most common signature seen by IVCM, are observed as spherical, round, ovoid, pear, egg, or coffee bean-shaped hyper-reflective structures measuring 15-28 µm in diameter and localised in the epithelium and the stroma [2, 11]. Sometimes, these cysts have a double-wall nature and appearance with a diameter measuring between 10 and 30 µm (see Figure 2.1). Matsumoto et al. [26] reported double-wall cyst structures in various sizes and shapes with the diameters of cysts ranging between 20 and 100 µm. The space between the outer and the inner wall is not stable and the tracery structure inside the inner wall also showed variation [26]. The authors of [26] imputed the variations in cyst sizes to either the difference of the biological behaviour of the amoeba organisms in living tissues compared to the in vitro environment in cultures or to the presence of different pathogenetic strains in the tissues. Double-wall cysts are considered a mature stage of Acanthamoeba and these cysts typically vary in diameter from 5 to 200 µm [9].

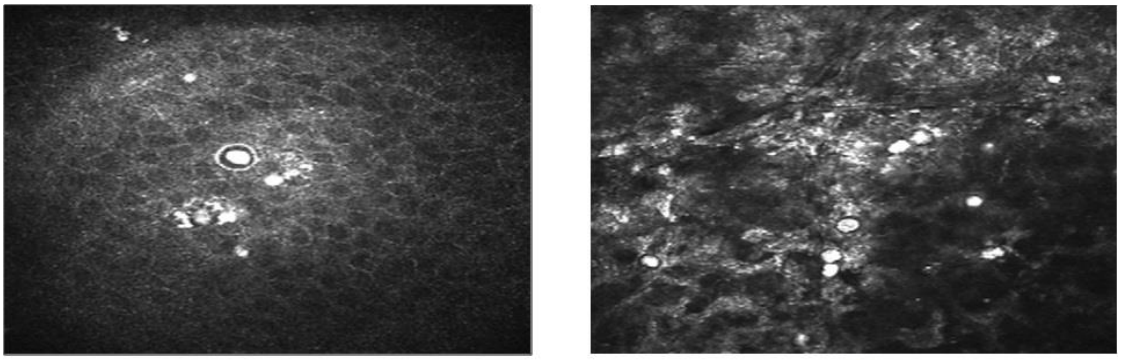

Figure 2.1 Acanthamoeba keratitis imaged by laser scanning confocal microscopy: HRT-RCM [11]. A) Acanthamoeba cysts with single-wall and double-wall appearance in the epithelium. B) Acanthamoeba cysts with a single-wall appearance in the stroma.

Trophozoites are the active and motile form of Acanthamoeba [11, 29], and they are slightly larger than cysts; measuring 15-45 µm in diameter, and may have low interior reflectivity [29]. According to Labbe et al. [11] trophozoites

are variable in shape and size; from 15 μm to more than 100 μm. Although IVCM may be able to afford images of trophozoites in Acanthamoeba keratitis, they appear to be more difficult to be distinguished from other hyper-reflective structures [11]. Matsumoto et al. [26] reported images of trophozoites using the HRT II-RCM for the first time in the literature and they described them as high-reflective and multiform structures that are homogeneous intense and measuring generally over 100 μm in diameter. It has been reported that the trophozoite forms are more difficult to discern with previous confocal device technologies as they appear within the corneal stroma similar to normal corneal keratocyte nuclei with ovoid, S-shaped structures [26].

The clinical features of fungal keratitis are not specific, particularly in the early phase of the disease, and clinically it looks similar to more common cases of infectious keratitis [11, 18]. For that reason, the diagnosis is frequently not suspect until an aggressive treatment for bacterial, viral, or amoebic keratitis has failed [11]. Many factors increase the risk of developing fungal keratitis; they include contact lens wear, trauma with vegetable matter, and immunosuppression (especially with topical corticosteroids [30]. The major etiologic agents of fungal keratitis are filamentous fungi especially with Fusarium and Aspergillus species [11].

The first experiment to analyse the characteristics of filamentous keratitis was done by Chew et al. in a rabbit model of keratitis (Aspergillus) using TSCM [11, 31]. They observed hyper-reflective, thin, and branching hyphae of variable lengths and 3-5 μm in width in the stroma. In a similar model, interlocking white lines approximately 6 μm in width, 200-400 μm in length and with branching at a 45° angle were observed in the superficial stroma by Avunduk et al. [11, 32]. In

this rabbit model and in the later stage of infection, IVCM was more sensitive than culture techniques in diagnosing fungal keratitis. More recently, Brasnu et al. showed comparable IVCM images with the HRT-RCM where they could differentiate experimentally Fusarium solani with branches at a 90° angle from Aspergillus fumigatus with branches at a 45° angle [11, 18]. Fusarium is also a filamentous fungus similar in appearance to Aspergillus but consists of hyphae with branches that are oriented at a 90° angle [33]. Four cases of Fusarium solani keratitis imaged with the HRTII-RCM were analysed by Brasnu et al. [11, 18]. They observed numerous hyper-reflective lines of length 200-300 μm and of width 3-5 μm with branches at a 90° angle in the anterior stroma resembling Fusarium hyphae and consistent with the cytological examination of corneal smears. Vaddavalli et al. [12] used SSCM in 103 microbiologically proven cases of Acanthamoeba or Fungal keratitis, and their study was able to identify fungal filaments in fungal keratitis or Acanthamoeba cysts in Acanthamoeba keratitis in 91 cases with a sensitivity of 88.3% and specificity of 91.1%. The criterion they used to identify fungal filaments with confocal microscopy was the presence of highly reflective filaments varying in size between 3 and 8 μm. These filaments had a uniform width with an irregular branching pattern and were not seen in isolation. A case of fungal keratitis was studied by Labbe et al. [34] using an HRTIII-RCM. The IVCM images revealed hyper-reflective, thin, and branching interlocking linear structures in the stroma, 200-400 μm in length and 5-7 μm in width resembling filamentous fungi. These bright structures were detected on the boundaries of the central corneal infiltrate at depths ranging between 100 to 300 μm and were surrounded by oedema and inflammatory cells. 38 confirmed fungal keratitis patients were enrolled in a study by Wang et al. [17]. The group of patients including 18 of isolated Fusarium species and the confocal

microscopy images of them showed branching and hyper-reflective hyphae appearing as interlocking white lines, 2 to 4 μm in width woven together forming reticulation in the superficial stroma. Shi et al. used an SSCM to adapt and guide antifungal therapy [16]. They monitored 121 patients with fungal keratitis, and before antifungal therapy, they found a significant reflection at the centre of corneal ulcers in all the patients using confocal microscopy. Thin and branching filaments which interlaced with each other were identified clearly in the background and some bright and obscure boundary inflammatory cells of various sizes were also observed. As described by Winchester et al. [33], the hyper-reflective filaments can be confused with basal corneal epithelial nerves and with stromal nerves. However, basal corneal epithelial nerves have relatively moderate branching compared to the numerous and chaotic branching of fungal filaments, and stromal nerves are much larger in diameter (25–50 μm) and located deeper in the stroma.

2.3. Technical review of Acanthamoeba keratitis and fungal keratitis (Fusarium)

The existing work on cornea using automated IVCM based systems is still limited and mostly focuses on the healthy cornea. The main areas that have been covered by the researchers who developed automated corneal systems using IVCM are: determining cell counts and densities, classifying layers, 3D reconstruction, and tracing nerves. For example, Elbita et al. [5] introduced an automated system for corneal layers classification, re-ordering, registration and segmentation of sequences of corneal images. Furthermore, a simple but promising 3D model of colour labelled segmented objects in a sequence of the confocal image was implemented. Scarpa et al. [35] addressed the problem of

providing a 3D reconstruction of an in vivo sequence of corneal images. Ruggeri and Pajaro [36] classified confocal microscope corneal images into their related layers using artificial neural networks. They based on some features derived from the shape processing of cells. Sharif et al. [37] introduced an efficient pre-processing approach that enhances the visual appearance of confocal corneal images before their use in subsequent analysis and classification. This approach is able to detect the individual keratocytes in the resulting enhanced images of stroma and provide their count and density, as well as their individual properties. In addition, a useful interactive graphical user interface was developed. Sharif et al. [6] developed a robust system to analyse corneal endothelial cells and to extract clinically useful information to help clinicians in diagnosing the endothelial layer rapidly and accurately. They addressed the problem of automatic estimation of endothelial cell densities in healthy images and they worked as well on three abnormal images with Fuchs' dystrophy, advanced Fuchs' disease, and posterior polymorphous corneal dystrophy (PPCD). Corneal sub-basal nerve tracing is a developing field that is of interest to researchers working with the healthy and diseased cornea. A possible application is to Diabetic Peripheral Neuropathy (DPN), a common type of diabetes that can affect the cornea, and an accurate analysis of the nerve structures could help in the early diagnosis of this disease. In that context, Al-Fahdawi et al. [38] proposed an automatic corneal sub-basal nerve registration system that produces a new informative corneal image containing structural and functional information. In addition, they produced a colour coded map for nerves after overlaying the sequence of registered corneal confocal microscopy images that differ in their illumination, displacement, scaling, and rotation. Al-Fahdawi et al. [39] proposed a fast, efficient and fully automatic

nerve segmentation and morphometric parameter quantification system for corneal confocal microscopy images. The system has potential to be used as a real-time and a fully automatic nerve tracing system in patients with DPN for diagnosis and follow-up. The system is able to provide clinicians with useful clinical features, such as nerve length, density, tortuosity, thickness, nerve perimeter, area and the image intensity.

Alzubaidi et al. [7] identifies the visual signatures of the most common corneal diseases and extracts the main features of those signatures in terms of reflectivity, shapes of the region of interest, and diffusion. This is the starting point of the aim to develop an automated diagnostic system that can help ophthalmologists in detecting abnormalities in confocal microscope images of the cornea.

Tsibidis et al. [40] developed an automated system that aims to assist in the extraction of quantitative information on Acanthamoeba polyphaga and cysts in a lawn of Salmonella Typhimurium bacteria. They identified objects in a series of images using thresholding. An automated classification of amoeba and cysts was performed by considering a circularity criterion. A manual correction of the object distinction was subsequently performed by means of a Graphical User Interface (GUI) to overcome problems related to classification errors. It should be noted that their system differs substantially from the system aimed at in this research. They demonstrated the interactions of protozoans with bacteria on plates examined with spatio-temporal images obtained using a Hamamatsu black and white digital camera (see Figure 2.2).

Qiu et al. [41] proposed a corneal fungi automatic detection method using a simple segmentation based on thresholding. They worked on images

obtained by HRT3 in vivo confocal microscopy. They enhance the images by applying a sub-regional contrast stretching algorithm, then they segment the hyphae based on a threshold to acquire binary images. The threshold used was set based on a maximum between-cluster variance algorithm. At the end, some morphological operations are done to fill up the gap in cracked hyphae and to remove unwanted regions. This kind of image cannot be segmented, and hence the hyphae be separated from the complex background, using simple segmentation based only on thresholding. Figure 2.3 shows an input image from the study by Qiu et al. and their segmentation result.

This research focuses on the diagnosis of infectious keratitis especially Acanthamoeba keratitis and fungal keratitis (Fusarium) in confocal microscope images. To the best knowledge of the researcher, there is no existing specialised automated system that tries to diagnose Acanthamoeba cysts or Fusarium hyphae in terms of colour mapping, tracking, and quantitative analysis.

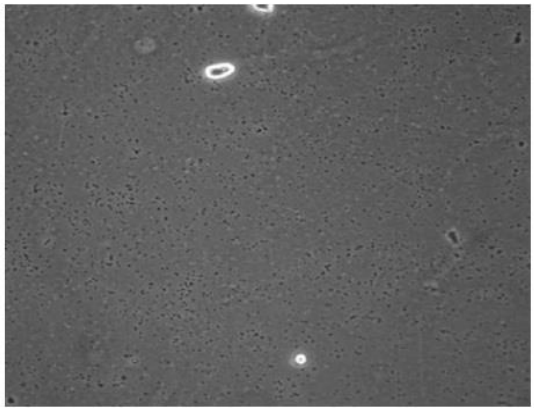

Figure 2.2 Example of the original image of bacteria (dark spots) in the presence of protozoa (bright regions) from the study by Tsibidis et al. [40].

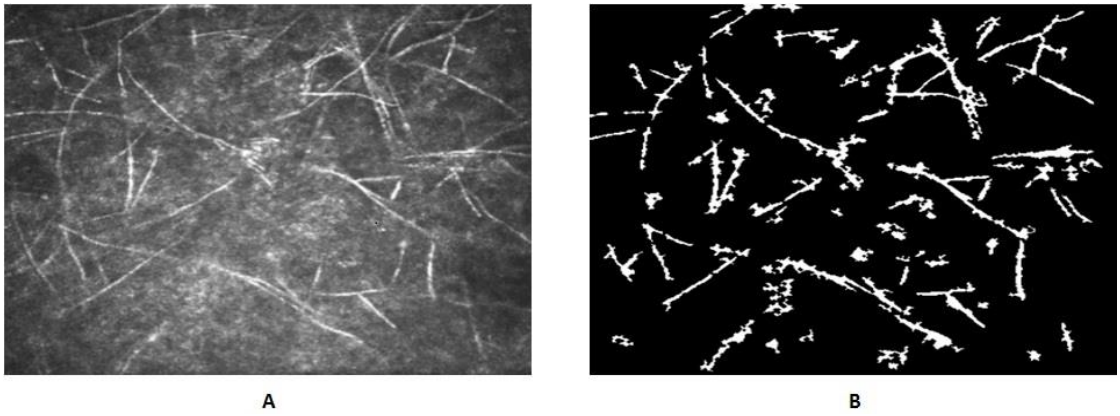

Figure 2.3 Example of the original image from the study by Qiu et al. [41]. A) The original image of fungal keratitis from Qiu's dataset. B) The result of Qiu's method.

2.4. Gaps in knowledge

This section highlights the main issues related to Acanthamoeba keratitis and fungal keratitis and is based on notes taken during a) a meeting between the author and the ophthalmology consultants of this research; Dr Arun Brahma and Dr Andrew Walkden (A. Brahma and A. Walkden, personal communication, Jan 15, 2017), and b) a Skype call with the ophthalmology consultant Dr Jaya Chidambaram (J. Chidambaram, personal communication, May 14, 2017).

There are two main stages of Acanthamoeba: 1) the trophozoite phase, which is the active phase that causing inflammation and cell destruction and resulting discomfort and reduced vision for the patient. This phase is treatable but cannot be easily visualised by the confocal microscope because this device captures little reflected light from the cell morphology. 2) The cystic phase, which is the dormant phase that is difficult to treat, as tough cellular walls are formed around the protozoa. Cysts have high light reflectivity and can, therefore, be visualized by in vivo confocal microscopy.

The Acanthamoeba cells are mobile and seek nutrition to grow and multiply. Trophozoites are found in the active infectious phase and they then go into the dormant phase if the environment changes i.e. lack of nutrition or supportive environment or due to anti-microbial therapy (PHMB and Brolene).

Anti-Acanthamoeba drugs need to be applied in high concentration at very early stages to kill Acanthamoeba whilst they are in the trophozoite phase. This treatment also causes damage for normal cells as the trophozoites have very similar metabolism to human cells.

In comparison to bacteria which can be treated effectively using antimicrobials, trophozoites can resist treatment by entering into the cystic phase which is impermeable to anti-microbials. These can remain dormant for long periods, and reactivate in the correct environment; this means that in future if surgery is planned, such as laser refractive surgery, it cannot be guaranteed that the infection will not reactive at a later date.

In general, if many cysts are seen in the confocal examination, it can be assumed that a high protozoal load is present. Ideally, the aim for the clinicians is to commence treatment before multiple dormant cysts occur, as this is when protozoal toxicity is most effective.

The confocal examination is useful to detect evidence of previous or active Acanthamoeba infection. The results are always used in conjunction with the clinical signs and symptoms of the patient. For example, if a patient who wears contact lenses exhibits corneal signs of inflammation, with cysts seen in the confocal images, treatment may be warranted.

Colour mapping is used in many ophthalmic devices e.g. OCT and corneal topographical scanning. It helps to draw attention to affected areas, with red usually denoting severe pathology and lighter colours e.g. green or blue being used for values within the normal range. A system that could count the number of cysts and gives other quantitative parameters would also be useful clinically.

Regarding fungal keratitis, the corneal ulcers caused by filamentous fungi are increasing in frequency throughout the world. It can take up to a week to grow these fungi in culture after a sample is taken from the surface of the ulcer, however, the corneal disease can significantly worsen during this time period. HRT3 laser scanning in vivo confocal microscopy is a high-resolution method allowing experienced graders to instantly detect fungal filaments in the cornea. However, it can be difficult to find and train confocal microscopy graders to accurately detect fungal filaments in the images. Use of an automated system could overcome this problem, and help a clinician to make the diagnosis then start the correct treatment more quickly.

Also, response to treatment can be difficult to assess in fungal keratitis using clinical examination alone, but there is evidence that fungal filament morphology may change over time with the use of the correct antifungal treatment (e.g. fungal filaments breaking up or disappearing) [19, 42]. An automated system to analyse confocal microscopy images for such changes would also assist clinician in determining whether the ulcer is improving, or whether a change of treatment is needed.

Some challenging areas are still unexplored and could help ophthalmologists with diagnosis of Acanthamoeba. Firstly, there is a need to

design a system that can accurately perform serial scans in an identical location on the cornea in order to allow follow-up scans to be performed. This will help assess the response to treatment. Secondly, there is a need to design an in vivo microscopy system that can pick up amoebas in their active form and separate them out from dormant cells and activated keratocytes.

2.5. Conclusion

One of the most important clinical uses of IVCM is to diagnose infectious keratitis, and it is also considered as an adjunctive modality to the clinical history and symptoms of the patient. Acanthamoeba cysts and Fusarium hyphae can be recognised from the corneal cellular structures using IVCM. Ophthalmologists need an automated system that could label the affected regions and analyse them, and determine the depth of the infection to evaluate the status of the patient and then to be used in the follow-up and treatment assessment.

From the previous review in Section 2.3, it has been noticed that there are no available automated systems that detect suspected cysts and hyphae in confocal microscope images to help improve the diagnosis of Acanthamoeba keratitis and fungal keratitis respectively. The researcher, and from her own experience, imputes that to the lack of communication between clinicians and computer scientists, and to the dearth of the available dataset to work on.

3. Acanthamoeba Images Enhancement and Segmentation

3.1. Introduction

Confocal microscope images of Acanthamoeba are not ready to be processed. They suffer mainly from blurring and hazing which makes the identification of the contours of Acanthamoeba cysts harder. Also, unwanted information, which could result from hyper-reflective inflammatory cells or noise affecting the original cells, appears among Acanthamoeba cysts (see Figure 3.1, A1-A3). For that reason, there is a pressing need to pre-process the images to enhance the appearance of the region of interest and improve the outcome of the segmentation process. Segmentation of Acanthamoeba images helps to separate the cysts from the background and then simplifies tracking them in the sequence of images. Cyst tracking will be explained in detail in Section 4.3.

Section 3.2 covers the algorithm proposed for enhancing Acanthamoeba images by reducing hazing and blurring and any unwanted information, while the segmentation algorithm proposed for detecting Acanthamoeba cysts from the binarised images is described in Section 3.3. Section 3.4 analyses the quantitative parameters obtained for Acanthamoeba cysts. Section 3.5 evaluates and discusses the results obtained after applying the proposed approaches of enhancement and segmentation on the dataset. The conclusion is presented in Section 3.6.

3.2. The proposed approach for image enhancement

3.2.1 Overview

Image enhancement seeks to improve the quality of an image [43]. What is considered an improvement in the image is subjective and depends usually upon the application, as well as on the perception of the observer [43, 44]. For example, we can improve the contrast and brightness characteristics of the image, reduce its noise content, or sharpen its details. The process of image enhancement is often used to improve the image for a subsequent analysis operation [43]. There are massive numbers of image enhancement techniques, however, the techniques used in this research were chosen with regard to the nature and the characteristics of the images that have been provided in the dataset. The focus was in reducing blurring, hazing, and any information not relevant to the segmentation of Acanthamoeba cysts.

3.2.2 Anisotropic diffusion filter

This work has adopted the use of Anisotropic Diffusion Filter that was proposed by Perona and Malik in 1990 [45] to enhance blurry noisy images. Anisotropic Diffusion is a non-linear filtering method that was introduced to avoid blurring at edges and localization problems caused by linear diffusion filtering that uses constant diffusion coefficient. It aims to reduce image noise and smooth the image without removing significant parts that are important for the interpretation of the image [45-47]. The confocal microscope images of Acanthamoeba keratitis suffers from the appearance of many unwanted information besides the cysts, such as affected layer cells and haze which have hypo-reflectivity and un-sharp borders in comparison to the cysts. This makes the Anisotropic Diffusion Filter convenient for use in this work. It helps to

smooth the homogeneous regions (whether the background area or internal region of the cyst). Moreover, it preserves the important features such as boundaries of the cysts.

The Anisotropic Diffusion equation identified in [45] is:

$$\begin{Bmatrix} I(x,y,t) = div[c(x,y,t)\nabla I] \\ I(x,y,0) = I_0 \end{Bmatrix} \qquad Eq.3.1$$

where *(x,y)* specifies spatial position, *t* is the time parameter (the iteration step), *div* is the divergence operator, ∇*I* is the gradient of the version of the image at time *t*, *c(x,y,t)* is the diffusivity (edge-stopping) function (diffusion coefficient) that controls the rate of diffusion; *c(x,y,t) = g(||E(x,y,t)||)*, where g(.) is a function of the image gradient so as to preserve edges in the image. I_0 is the original image. The diffusivity function is chosen to satisfy $g(||E||)\rightarrow 0$ when $||E||\rightarrow\infty$, so that diffusion is stopped across edges [46, 48].

The authors of [45] suggested two different functions for diffusion coefficient:

$$g_1(||E||) = \frac{1}{1 + \left(||E||/_m\right)^2} \qquad Eq.3.2$$

or,

$$g_2(||E||) = exp\left[-\left(||E||/_m\right)^2\right] \qquad Eq.3.3$$

where *m* is a parameter that controls the sensitivity to edges (the level of diffusion between edges and homogeneous region in the image) and is either set experimentally or as a function of the image noise.

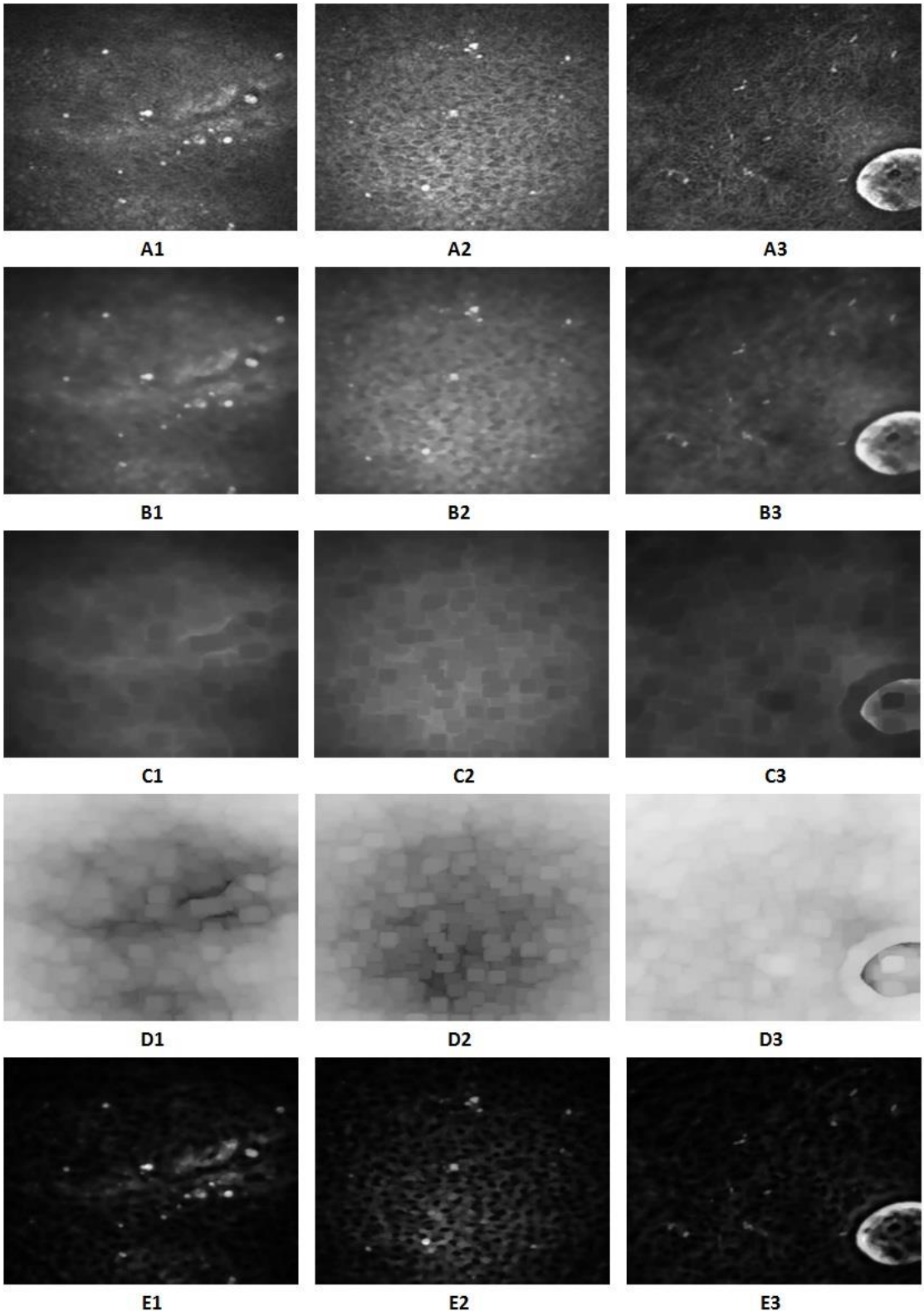

Figure 3.1 Enhancement steps for Acanthamoeba image. A1-A3) Input images from the dataset. B1-B3) Anisotropic diffusion filter output. C1-C3) Dark channel output. D1-D3) Transmission map output. E1-E3) Recovering scene radiance output.

In this work, the exponential diffusion coefficient was used with an *m* value equal to the standard deviation of the image. The time parameter *t* was set to 3. These values of *m* and *t* contribute to smooth the noise without losing the main structure of cysts. The results of this step are shown in Figure 3.1, B1-B3.

3.2.3 Dark channel prior

To eliminate haze from input images, this research uses the simple but effective idea of the dark channel prior proposed by He et al. [49] for images of outdoor scenes. It is based on the key observation that there are some pixels having very low intensities in at least one colour channel of haze-free outdoor images. The thickness of haze could be directly estimated using this prior with the haze imaging model and therefore a high-quality haze-free image would be recovered.

The main steps of the dark channel prior scheme [49] could be summarised as follows: a) Calculate the dark channel. b) Estimate the transmission map. c) Estimate the atmospheric light. d) Recover the scene radiance.

The statistical observation or knowledge of dark channel prior for an image *J* is defined as:

$$J^{dark}(x) = min\left(min\left(J^{c}(y)\right)\right), c \in \{r, g, b\} \;\; y \in \Omega(x) \qquad Eq.3.4$$

where J^c is a colour channel of *J* and $\Omega(x)$ is a local patch centred at *x*. The intensity of J^{dark} (except for the sky region) is low and tends to be zero. J^{dark} is the dark channel of the haze-free outdoor image *J*.

The dark channel of the haze image has a higher intensity in regions with denser haze, due to the additive air light which makes a haze image brighter than its haze-free version where the transmission *t* is low. Visually, the intensity of dark channel is a rough estimate of the thickness of haze. This property was used in [49] to estimate the transmission and the atmospheric light. Figure 3.1, C1-C3 shows Acanthamoeba images after obtaining the dark channel.

Now, assuming that the atmospheric light *A* is given and the transmission in a local patch Ω*(x)* is constant. The authors of [49] estimated the patch's transmission t̃(x) by:

$$\tilde{t}(x) = 1 - \min_{c}\left(\min_{y\in\Omega(x)}\left(\frac{I^{c}(y)}{A^{c}}\right)\right) \qquad Eq.3.5$$

The *min* operation is performed on the three colour channels independently, $\min_{c}\left(\min_{y\in\Omega(x)}\left(\frac{I^{c}(y)}{A^{c}}\right)\right)$ is the dark channel of the normalised haze image $\frac{I^{c}(y)}{A^{c}}$. Therefore, the estimation of the transmission is directly provided as shown in Figure 3.1, D1-D3.

The scene radiance can be recovered with the transmission map as shown in Figure 3.1, E1-E3. When the transmission *t(x)* is close to zero, the direct attenuation term *J(x)t(x)* can be very close to zero. Therefore, the transmission *t(x)* is restricted to a lower bound t_0, which means that in very dense haze regions a certain, small, amount of haze is preserved. The final scene radiance *J(x)* is recovered by:

$$\mathrm{J}(x) = \frac{I(x) - A}{\max(t(x), t_0)} + A \qquad Eq.3.6$$

A is the atmospheric light. t_0 has a typical value which is 0.1. The image after haze removal looks dim because the scene radiance is usually not as bright as the atmospheric light. Consequently, the exposure of *J(x)* is increased by the authors of [49], and they improve the atmospheric light estimation using the dark channel prior. They pick the top 0.1% brightest pixels in the dark channel which are most haze-opaque. From those pixels, the pixel with the highest intensity in the input image is chosen as the atmospheric light.

Now, before going further, there is a need to raise some important points that show the difference between this work and the work of He et al. [49] in applying the 'dehazing' process.

- This work deals with medical grey-scale images produced by confocal microscopy and is aiming to detect Acanthamoeba cysts which are highly reflective objects on a dark background. Most images show haze that spreads among Acanthamoeba cysts. On the other hand, He et al. have worked on outdoor coloured images produced by cameras and the scene in each image is covered by haze and they aim to remove this haze and recover a high-quality haze-free image. Their approach works as well for the grey-scaled images, but only if there are enough shadow regions in the image.

- He et al. deal with the weather phenomenon called haze. Here haze is comprised of an aerosol which is a dispersed system of small particles hanging in gas [50]. Haze tends to produce a distinctive grey or bluish hue that affects the visibility of the scene [50]. Haze, smoke and fog differ mainly in the material, shape, size, and concentration of the atmospheric particles but He et al. don't distinguish these similar phenomena and use

the term haze in place of all of them for simplicity [49], while the case in this work is to deal with a display reflection called haze. Haze is a diffuse reflection that occurs when light generated from the medical device is randomly scattered into a narrow distribution of angles in the vicinity of the specular direction [51, 52].

From the comparison mentioned above, it is clear that the method of He et al. itself without any optimising or adapting is not valid for the haze problem of this work. Figure 3.2 shows the result of applying the method of He et al. (without any adaptation) to a sample from the dataset of Acanthamoeba images.

3.2.4 Contribution to reducing hazing using dark channel prior

It has been concluded that the prior channel scheme suggested by He et al. [49] is not efficient to reduce hazing in Acanthamoeba images. This happened due to the difference of haze natures in their images and this research's images. Furthermore, the prior channel scheme estimates haze from a clean hazy image, while the confocal microscope images in this research are noisy. Thus, an extra step was added to the dark channel prior scheme to get the processed image that is sought.

A common use of image subtraction is to subtract a background that varies in illumination from a scene, so that the foreground objects in the image may be more easily analysed [53]. The prior channel scheme has been applied to the diffusion-filtered image as shown in Figure 3.1, and when the researcher observed the dark, the transmission map, and the recovered scene radiance images, a clue was found to getting a reduced-haze image by subtracting the

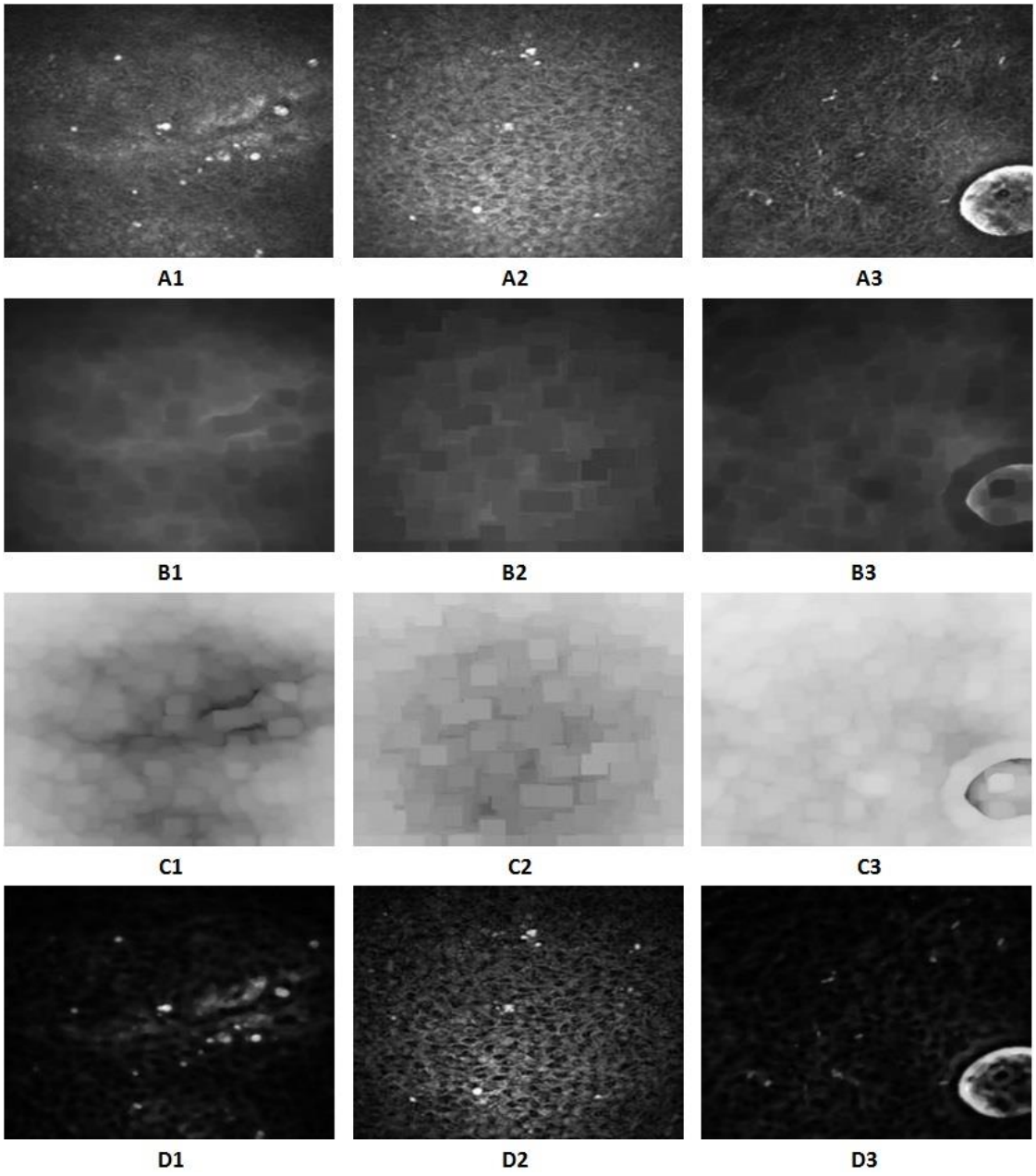

Figure 3.2 Channel prior method result. A1-A3) Input images from the dataset. B1-B3) Dark channel output. C1-C3) Transmission map output. D1-D3) Recovering scene radiance output (supposed to be haze-free).

dark image from recovered scene radiance one, the result is shown in Figure 3.3. It is obvious that the greyscale image obtained from this step is very clean and it contains most of the regions of interest that are being looked for in addition to few unwanted regions.

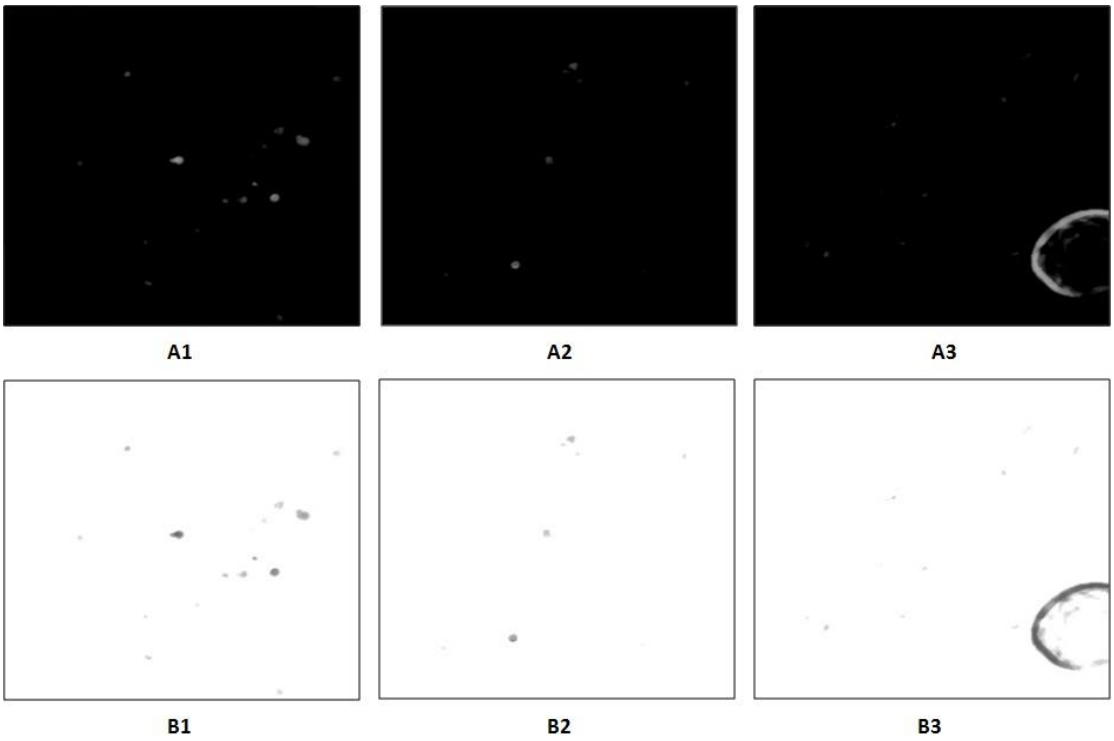

Figure 3.3 Reduce hazing in Acanthamoeba image using dark channel prior. A1-A3) Result of subtracting the dark image from recovered scene radiance image that appears in Figure 3.1 (called later enhanced image). B1-B3) The complement of images (A1-A3) respectively.

The enhanced image that resulted from this step possesses three significant characteristics which will be used as a base for further processing:

a) The image is greyscale.
b) The isolated background was not completely separated from the foreground. The subtraction process gave the background negative intensity values and they are displayed as black pixels or we can say these negative values are mapped to zero.
c) The resulting foreground contains most of the regions of interest in comparison to the images that were traced manually by the clinicians (see Appendix A.

3.3. The proposed approach for image segmentation

3.3.1 Overview

Image segmentation is applied to subdivide an image into its basic components, elements, or objects. The problem being solved determines the level to which this subdivision is carried out. Thus, segmentation should stop when the objects of interest for such an application have been isolated [43, 44].

The detection of Acanthamoeba cysts in confocal microscope images is rationally based on the most common features of Acanthamoeba cysts that are observed using in vivo confocal microscopy. As mentioned in Section 2.2, Acanthamoeba cysts appear as hyper-reflective and spherical, round, ovoid, pear, egg, or coffee bean-shaped structures. Therefore, the most obvious visual computing approach to automatically detect Acanthamoeba cysts is to extract components with high reflectivity pixels and then to keep the most circular shape regions among these components.

Is this visual impression verifiable, and if so, how can 'highly reflective' and 'circularity' be described mathematically?

In microscopic grey-scale images, a highly reflective region is a bright region that has high-intensity values, which means high-value pixels. Acanthamoeba images have a structure of grey to dark background and light grey to bright foreground, where the latter contains the cysts. It has been noticed that the final greyscale enhanced image that has been obtained after haze reducing included many high reflective regions which are most likely to be cysts. To detect these cysts and go further in processing, there is a need to binarise the enhanced greyscale image and this procedure is explained in the next section.

A common way to determine how close such a shape is to a circle is to evaluate the equation of circularity [54, 55]:

$$circularity = 4\pi \times (area)/(perimeter)^2 \qquad Eq.3.7$$

where *area* is the total number of pixels that occupy the region and *perimeter* is the total number of pixels that define the boundary of the region. With continuous data, a circularity value of 1 indicates a circular region (with the smallest perimeter to area ratio) and other shapes have smaller values of circularity. In this research, with sampled data, many roundness values have exceeded 1 when the regions are very small.

Put briefly, the regions of interest in this research are Acanthamoeba cysts characterised by their high intensity values and their circular shape. The effective enhancement step that has been proposed in Section 3.2 made the segmentation process much easier.

3.3.2 Contribution to binarisation for Acanthamoeba images

Binarisation or thresholding is the process of converting an image into a binary image with black background and white foreground. A threshold value is determined, and any pixel intensity value above that value is converted to 1 (white); otherwise it is converted to 0 (black). Image binarisation is a significant step for further image processing and analysis [56].

Because of the nature of the dataset images which show Acanthamoeba cysts with different appearances, it can be concluded that it is inappropriate to use a specific threshold value or one of the various existing binarisation algorithms to segment Acanthamoeba images in a way that isolates the cysts efficiently. For example, many of cysts do not have well-delineated borders (see

Figure 3.4, A1, B1, and C1), others are very blurred and connected together (see Figure 3.4, A2, B2, and C2) and some cysts appear as part of a reflective background which could be inflammatory cells or the original cells or an artefact (see Figure 3.4, A3, B3, and C3).

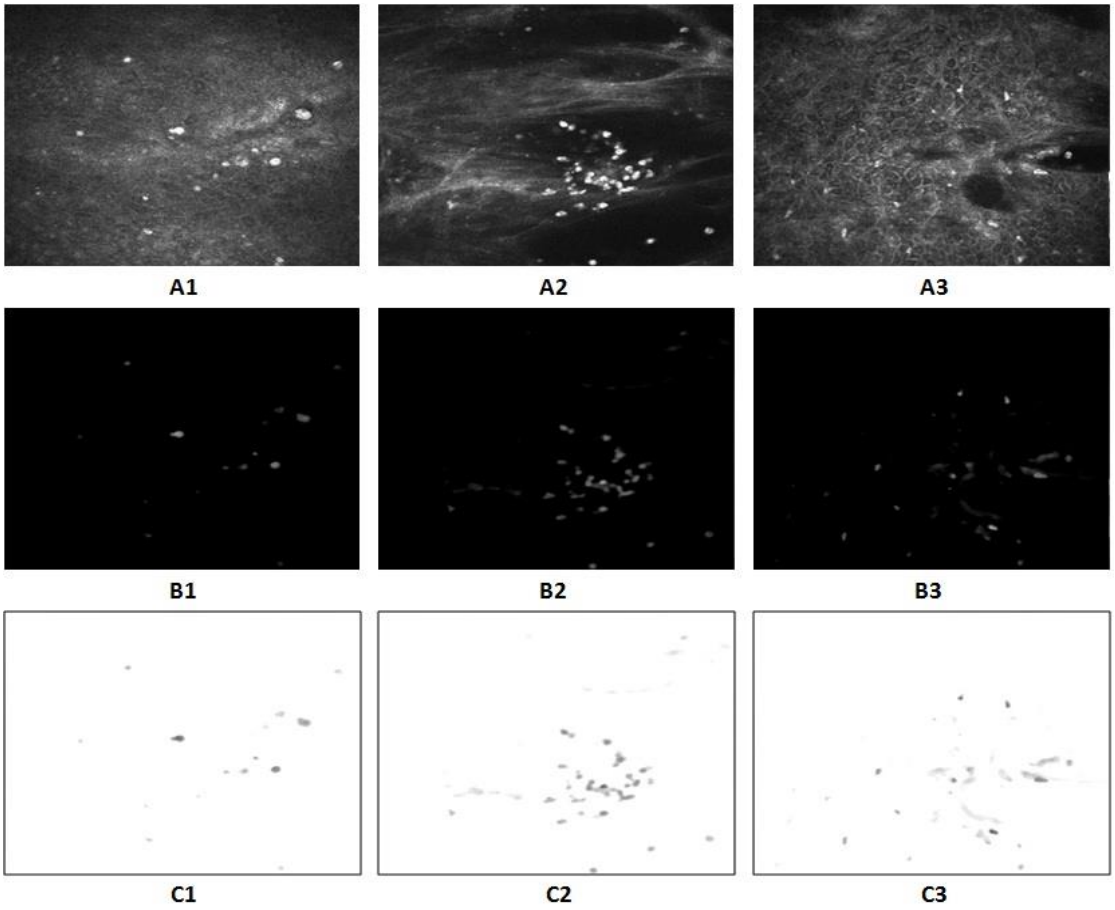

Figure 3.4 Different appearances of Acanthamoeba cysts. A1-A3) Input images from the dataset. B1-B3) The enhanced images according to the proposed approach in Section 3.2. C1-C3) The complement of images (B1-B3) respectively.
1: Example on cysts which do not have well-delineated borders. 2: Example on cysts which are very blurred and connected together. 3: Example on cysts which appear as a part of reflective background which could be inflammatory cells or the original cells or an artefact.

3.3.2.1 Normal sized cysts

In this work, a very simple but effective binarisation method was proposed. The idea has arisen from the way that cysts look in the Acanthamoeba images as mentioned previously in Section 3.3.2. That means it

is inefficient to binarise Acanthamoeba image in one go; there is a need to start with the most reflective regions, then the second most reflective regions, then the third most reflective regions, and so on. For each reflective regions phase, the circularity of those regions is computed and the regions that have roundness values above a threshold are kept. This method of binarisation gives a chance to check the criteria for Acanthamoeba cysts at each level.

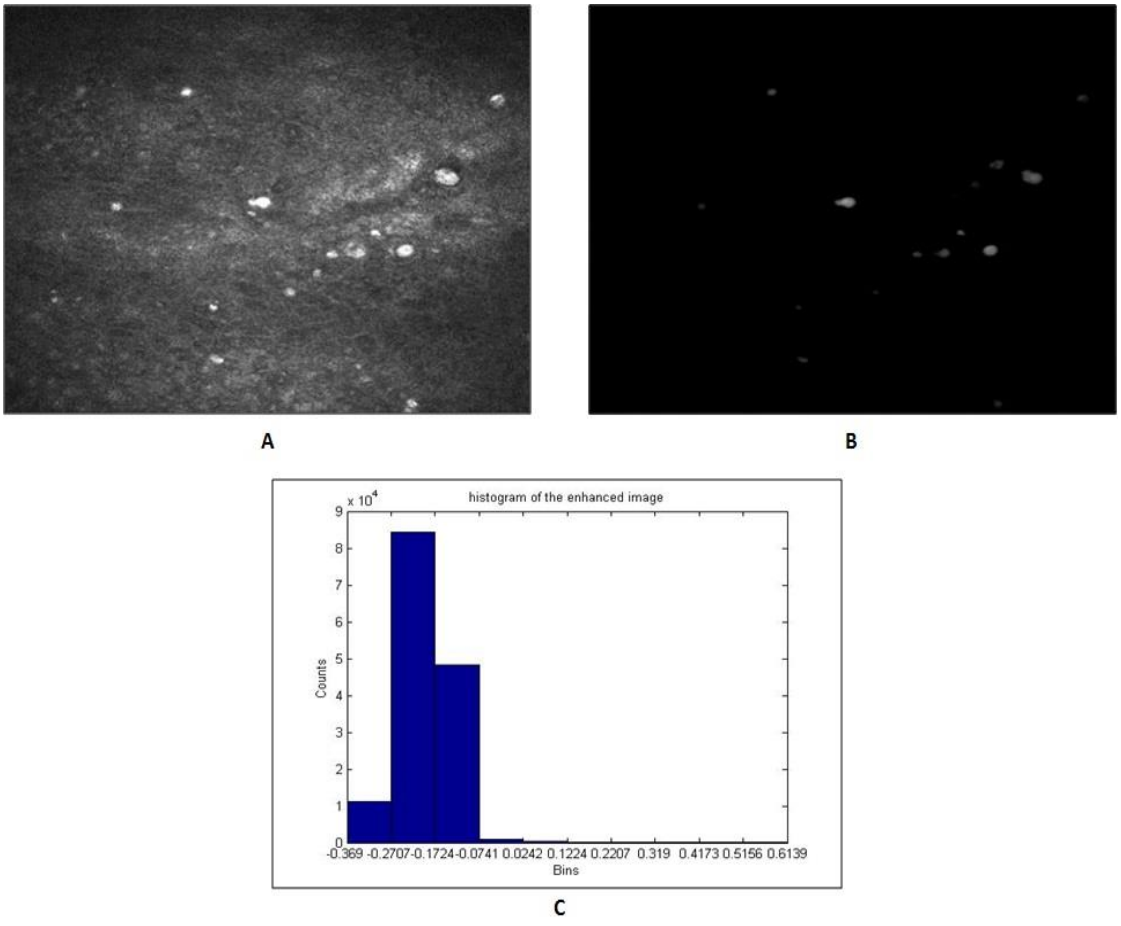

Figure 3.5 The example that used to show the proposed binarisation procedure. A) Input image. B) The enhanced image of (A) that is produced in Section 3.2.4. C) Representation of the histogram of the enhanced image appears in (B) as column graph.

To reach these different phases of reflectivity, the idea of binarising the enhanced image (which is produced in section 3.2.4) level by level was suggested. The image that appears in Figure 3.5A and its enhanced version that appears in Figure 3.5B are used to clarify the proposed idea of binarisation.

These levels are defined using the histogram of the enhanced image which is shown in Figure 3.5C. Here it is important to mention that the grey scale that is dealt with in this research is floating point, of class double; and the pixel intensity value ranges from 0 to 1. Therefore, it is reasonable to divide the histogram into ten bins (levels) starting from the minimum value and ending at the maximum value for the enhanced image. Moreover, this number of bins contributes to detect as much as possible of cysts especially in the case of blurring and connecting cysts, and it contributes as well to find the appropriate stopping level which is explained later. To create ten bins with defined lower and upper edges, the range of image intensity values is divided by 11 evenly spaced points in the interval [min_value, max_value] which corresponds to [-0.3690, 0.6139] in this example. Then to start the binarisation, all pixels that have intensity values equal to or exceed the lower edge of the tenth level are converted to 1 and then the connected components are identified and the roundness value for each component is computed. Any component that has a roundness value less than the threshold is ignored and then to refine the shape of those components; a morphological erosion operation using a disk structure element is applied. The next step is to convert all pixels that have intensity values equal to or exceeding the lower edge of the ninth level into 1 and then the connected components are identified and the roundness value for each component is computed. Any component that has a roundness value less than the threshold is ignored. The same thing is done with the eighth level and so on until the stopping level is reached. The stopping level in this example is level four (procedure of selecting the stopping level is explained later).

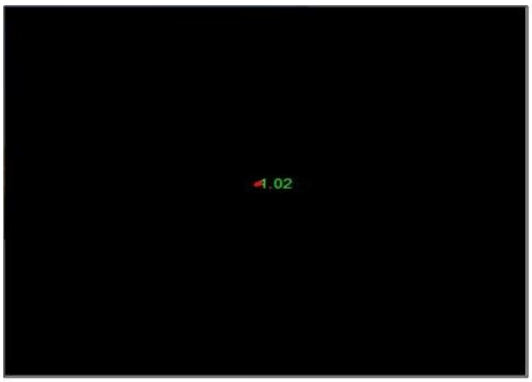

A1

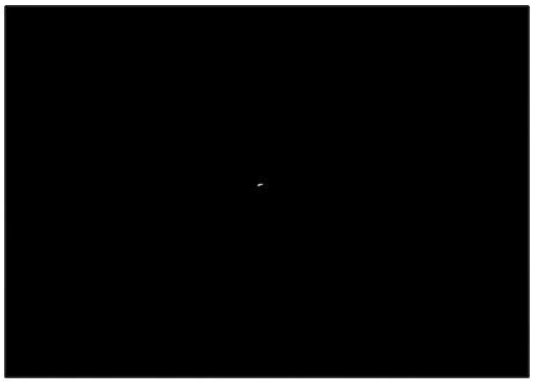

B1

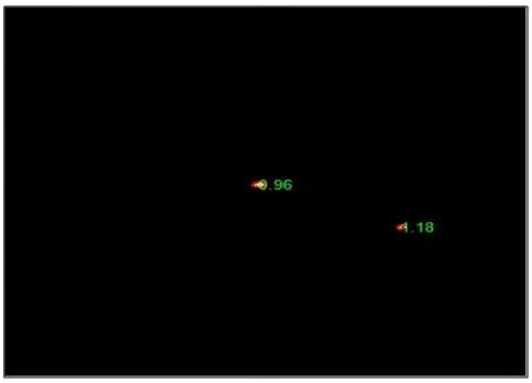

A2

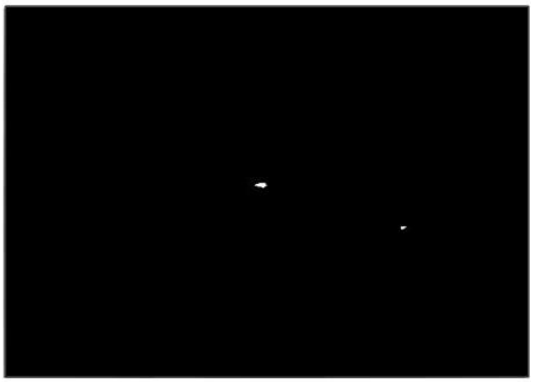

B2

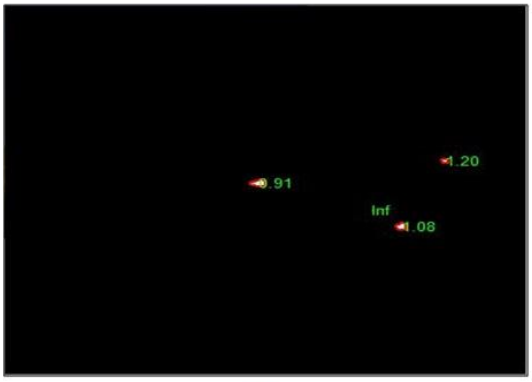

A3

B3

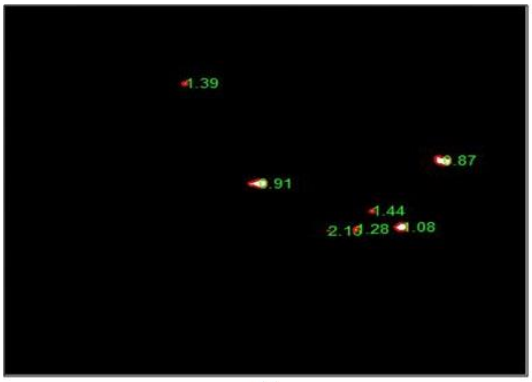

A4

B4

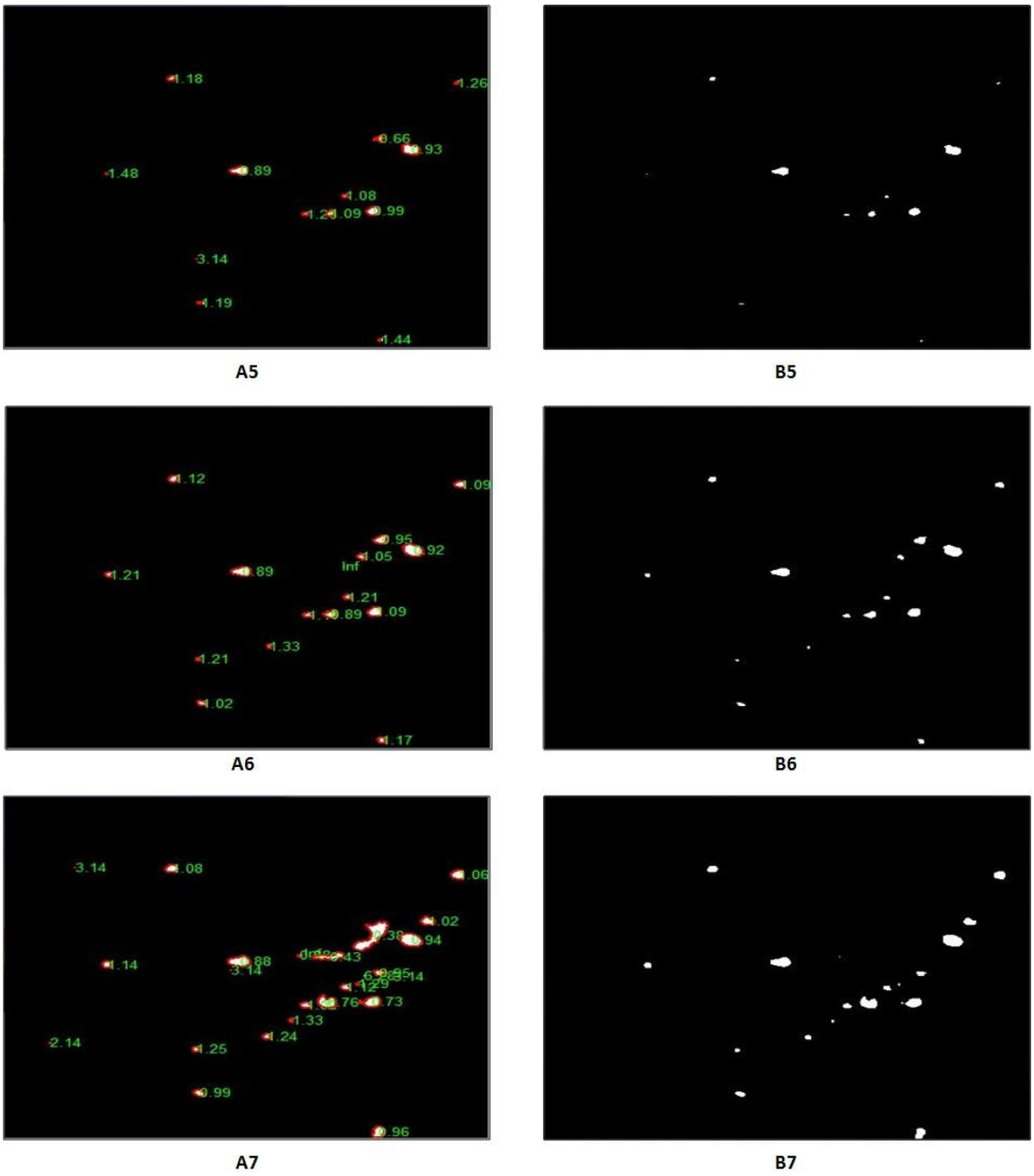

Figure 3.6 The proposed binarisation procedure for normal sized cysts. A1-A7) The results of converting all pixels that have intensity values equal to or exceed the lower edge of the i^{th} level into 1, and then computing the circularity values for each binarised component. (i starts from level ten and ends at the stopping level which is four in this example). B1-B7) The results from level ten to the stopping level (which is four in this example) of keeping components that have circularity values exceeding the threshold followed by erosion operation.

Figure 3.6, A1-A7 show the binarisation and roundness values for each binarised component from levels ten to four, while Figure 3.6, B1-B7 show the components kept after the roundness threshold is checked and after the erosion is applied from level ten to level four.

The outcome of each level is added to the one before and thus finally, an image of high reflective round regions is produced as shown in Figure 3.7.

Figure 3.7 All high reflective circular regions of normal sized cysts after applying the binarisation procedure. This result comes from combining images 1-7 that appear in Figure 3.6B to each other.

The two questions that arise here are 1) at which level to stop and 2) what is the threshold to use for the roundness (circularity) of cysts?

A logical way was proposed to discover the stopping level. Firstly, all positive pixels of the enhanced image (in this example, it appears in Figure 3.5B) are counted which means the foreground pixels. Secondly, the peak level is determined, defined as the level with the largest number of pixels. Thirdly, the first level from the left that has a number of pixels less than or equal to the number of foreground pixels and located to the right of the peak level is considered the stopping level.

The threshold for the circularity of cysts was chosen depending on the computation of the values of circularity for all the cysts that appear in the dataset and were detected manually by the clinician. The minimum computed value was 0.70. Consequently, any region with circularity value exceeding or equal to 0.70 is considered a circular region.

3.3.2.2 Massive sized cysts

Acanthamoeba images usually contain normal sized cysts ranging from 10 to 50 μm in diameter. They could have cysts of massive size reaching to more than 100 μm [11]. These cysts have a different structure from the normal ones; most of their interior parts are usually dark but having a fully or partially bright boundary. Consequently, it is not possible to detect these cysts using the method that has been described in Section 3.3.2.1. For that reason, another method was proposed in this section, and the image which appears in Figure 3.8A was used to illustrate the procedure. Figures 3.8B and 3.8C show the enhanced image of Figure 3.8A and its complement respectively. The idea is to convert all the foreground regions, which are represented by pixels with non-zero positive values, of the enhanced image to 1. This step ensures getting a result of, at least, the border of the massive cysts, in addition to the normal sized cysts and maybe other unwanted regions (see Figure 3.8D). The next step is the filling process, which fills any shape which has a closed border (see Figure 3.8E). To keep only the massive cysts, all unwanted regions that have fewer than *P* pixels were removed as shown in Figure 3.8F. From the area of a circle (see Eq.3.8) and the assumption that the diameter of massive cysts starts from 100, the value of *P* was set to 7000. The area of cyst that has a diameter of 100 is: 50 x 50 x π = 7850.

$$Area_{circle} = (radius)^2 \times \pi \qquad Eq.3.8$$

In the last step, the circularity of these massive regions is checked using a threshold value equal to 0.78 (see Figure 3.8G). The logic behind this selection comes from the computation of the values of roundness for all the cysts that appear in the dataset and were detected manually by the clinician. The

minimum computed value was 0.78. Any region having a circularity value below this threshold value is ignored. Therefore, if the original image contains massive cyst(s), this step ensures they are kept. The final result of detecting massive cyst(s) is shown in Figure 3.8H.

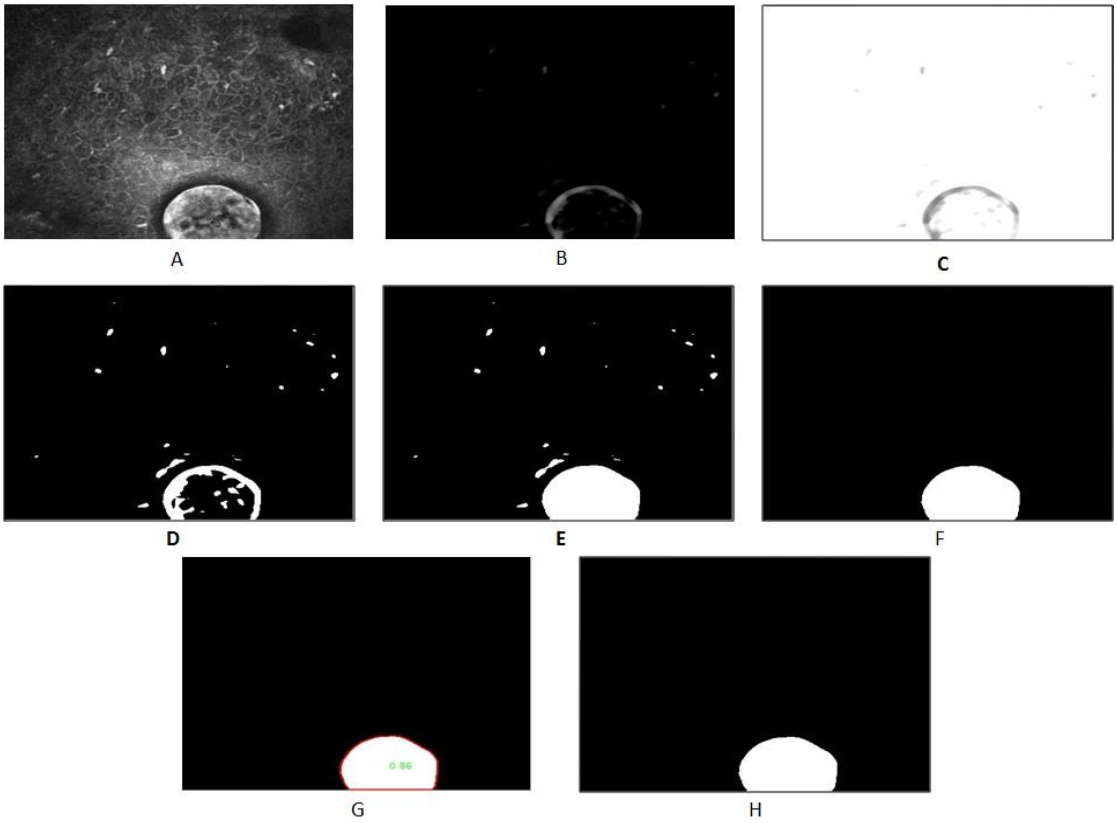

Figure 3.8 The proposed binarisation procedure for massive cysts applied to the image with massive cyst. A) Input image. B) The enhanced image of (A) that is produced in Section 3.2.4. C) The complement of the enhanced image. D) Converting all pixels with non-zero positive values of the enhanced image into 1. E) Filling any shape has closed border. F) Removing all unwanted regions that have fewer than 7000 pixels. G) Check the circularity of existing regions using a threshold value of 0.78. H) The final result of detecting massive cyst.

Another example of an image contains no massive cyst(s) (see Figure 3.9A) was demonstrated to show the efficiency of the proposed procedure. Figures 3.9B shows the enhanced image of Figure 3.9A. All foreground regions of the enhanced image are converted to 1 as shown in Figure 3.9C. The result of the filling step can be seen in Figure 3.9D. All unwanted regions that have

fewer than 7000 pixels are removed as shown in Figure 3.9E. It can be noticed that Figure 3.9E shows nothing because the original image (Figure 3.9A) contains no massive cyst(s).

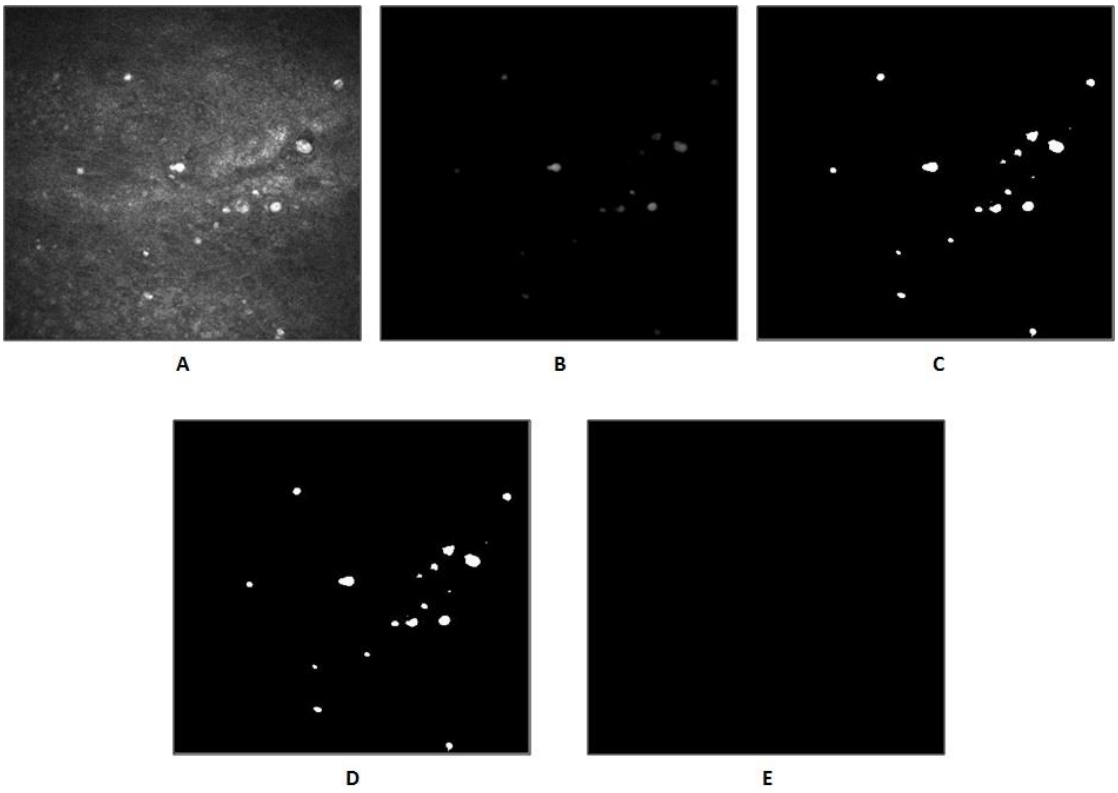

Figure 3.9 The proposed binarisation procedure for massive cysts applied to the image has no massive cyst(s). A) Input image. B) The enhanced image of (A) that is produced in Section 3.2.4. C) Converting all pixels with non-zero positive values of the enhanced image into 1. D) Filling any shape has closed border. E) Removing all unwanted regions that have fewer than 7000 pixels.

3.3.3 Detection of Acanthamoeba cysts

The regions that were detected in Section 3.3.2.1 represent the most circular reflective regions which are most likely to be cysts of normal size. A refinement step was proposed to support the segmentation process and consequently to make sure that the detected regions are verified as true regions of interest. The idea is to use the diffusion filtered image produced in Section 3.2.2 to emphasize bright regions (regions of interest), most of which are related to Acanthamoeba cysts or parts of those cysts. Figure 3.11A shows the

diffusion filtered image for the original input image shown in Figure 3.10A (which was used to demonstrate the proposed binarisation procedure). In contrast to the background which comprises grey to black values, the cyst has a bright interior or at least a bright boundary. Mathematically speaking, it should be noted that the variance in a small neighbourhood around a pixel is most probably larger than in the background. Hence, the regions with high local standard deviation, that is the square root of the variance, are defined. This is calculated by using a filter giving the standard deviation within a 3x3-neighbourhood of every pixel; the result is shown in Figure 3.11B. To use this image in improving the result of segmentation, there is a need to binarise it. A thresholding process similar to that mentioned earlier in Section 3.3.2.1 is used in this step. The histogram of the standard deviation filtered image is shown in Figure 3.11C, and the interesting part was to use the same stopping level that was detected in Section 3.3.2.1 to convert the standard deviation filtered image into a binary image as shown in Figure 3.11D. Here the binarisation process was done in one go, not level by level, where any pixel with an intensity value equal to or above the centre of the stopping level (see Eq.3.9) is converted to 1; otherwise, it is converted to 0. After that, regions in the binary image with fewer than 12 pixels are removed as shown in Figure 3.11E. It was found that the binarised components which most probably are cysts have regions with more than 12 pixels.

$$center_{level} = {(lowerEdge_{level} + upperEdge_{level})}/{2} \qquad Eq.3.9$$

The checking criterion, that is used to decide whether the detected regions in the binary image produced in Section 3.3.2.1 are region of interest, is

to find any pixel of that detected region appearing within the binarised standard deviation image.

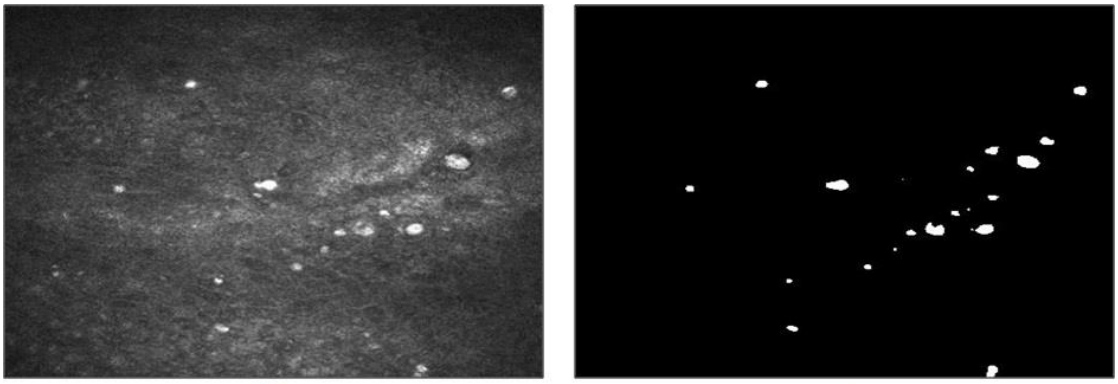

Figure 3.10 The image that used to show the proposed refinement step to detect the normal size of Acanthamoeba cysts. A) Input image. B) All high reflective circular regions of normal sized cysts detected after applying the proposed binarisation procedure.

More clearly, it is sufficient to look for any pixel of each identified region in Figure 3.10B and find its corresponding pixel in Figure 3.11E to decide whether such a region is of interest and is counted as a cyst. The result of this step is shown in Figure 3.11F.

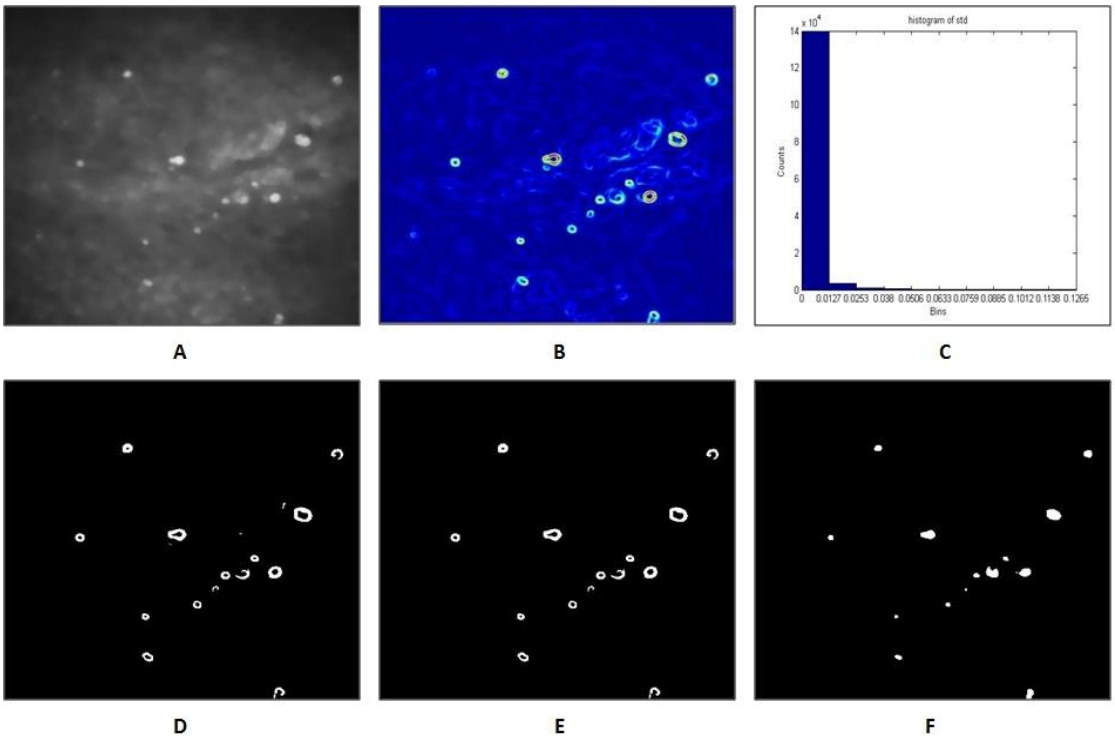

Figure 3.11 The proposed refinement step to detect the normal size of Acanthamoeba cysts. A) Anisotropic diffusion filtered image of the original image appears in Figure 3.10A. B) Local standard deviation of (A). C) Histogram of local standard deviation image appears in (B) represented as a column graph. D) Binarisation of the image (B). E) The binarised image after removing small regions. F) The result of keeping detected regions that at least one of their corresponding pixels is found in image (E).

To get all the detected Acanthamoeba cysts in one image which is considered the final result of cyst detection, the segmented image of normal sized cysts (after refinement stage) produced in Section 3.3.3 is added to the segmented image of massive cyst produced in Section 3.3.2.2. Figure 3.12 shows these final detected cysts; (A) as binary and (B) with their original intensity values.

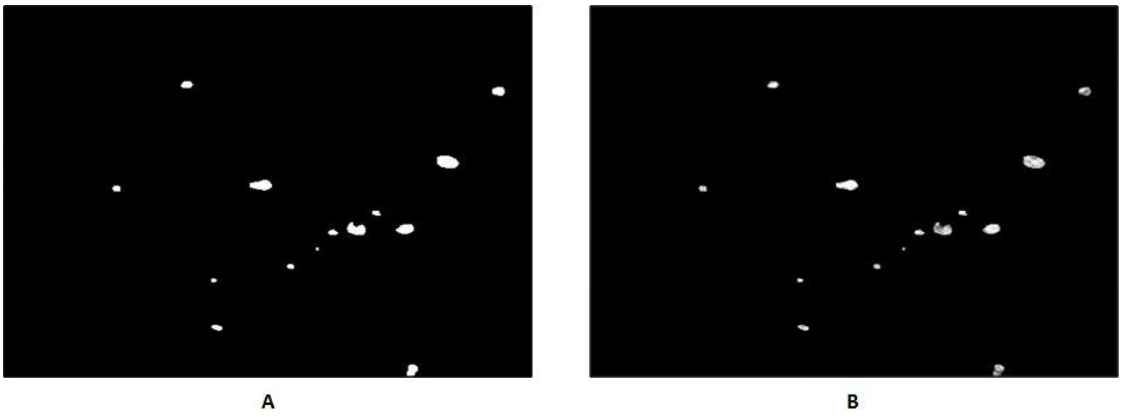

A B

Figure 3.12 Final result of the proposed segmentation process. A) All of the detected Acanthamoeba cysts in binary form. B) All of the detected Acanthamoeba cysts with their original intensity values.

For easier visualisation and following-up by clinicians, the detected cysts were marked on the original image in two ways; red circles and red pigmentation with numbering (see Figure 3.13).

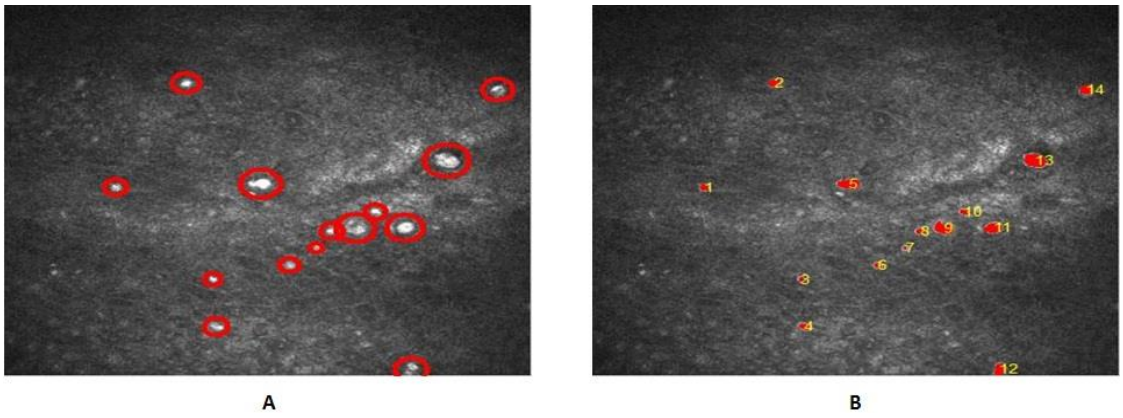

A B

Figure 3.13 Easier visualisation for the final detected cysts. A) Red circles around the detected cysts (Figure 3.12) over the original image (Figure 3.5A). B) Red pigmentation with numbering for the detected cysts (Figure 3.12) over the original image (Figure 3.5A).

3.4. Parameters for the quantitative analysis of Acanthamoeba cysts

Clinicians believe that there are criteria that could be useful in identifying Acanthamoeba keratitis or in measuring changes before and after treatment. As a result, this may help in excluding other round highly reflective structures that could be confused with Acanthamoeba cysts such as inflammatory cells,

epithelial cells or keratocyte nuclei, and may help as well in assessing the corneal response to therapy [12, 57]. These criteria could be summarised in the presence of oval to round highly reflective structures varying in size between 5 to 200 µm as mentioned in Section 2.2, and the number of cysts that confocal scan frames reveal would also be useful [26]. The differentiation between cysts and other structures may be still difficult when the characteristic double-wall feature is not visible [11]. There is no clear or specific description of the double-wall feature, but the study of [26] mentioned that the tracery structure inside the inner wall varied and the space between the outer and the inner wall was also not fixed, indicated by the black arrow in Figure 3.14.

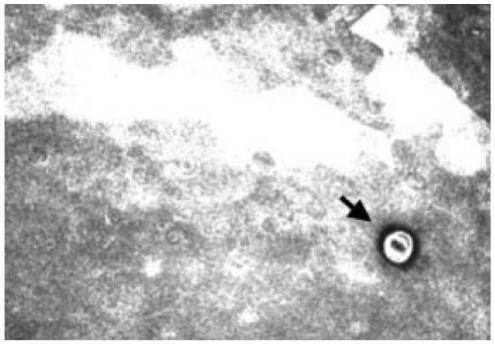

Figure 3.14 The HRTII-RCM appearance of double-wall Acanthamoeba cyst (black arrow) [26].

From the discussion above, it can be concluded that any quantitative parameter related to the reflectivity, size, shape, and count of the cysts may help in distinguishing cysts from other structures. Therefore, the system proposed in this research computed six parameters related to the criteria of identifying cysts in each processed image including: cyst number, darkness, halo, diameter, roundness, and lastly count of cysts. This information are automatically written and saved in a file (see Table 3.1 which shows the quantitative parameters for cysts appear in Figure 3.13).

Cyst number gives the number of each cyst according to its label (using 'bwlabel' MATLAB function). Cyst **darkness** is a parameter that measures the percentage of low-intensity pixels within the area of a detected cyst. Low-intensity pixels are determined using the multi-level Otsu thresholding method. The pixel intensities of the image have been divided into five levels (see Figure 3.15A). By observing the behaviour of Acanthamoeba cysts in the dataset, it was found that the dark intensity of the interior part of the cyst is located in the last three levels (black, dark grey, and mid-dark grey). The five-level image is binarised so all pixel intensity values coming within these last three levels are converted to 0 and the rest are converted to 1 as shown in Figure 3.15B. Then the percentage of cyst darkness is computed by counting the number of zeros that occur within the cyst's pixels and after that dividing the value by the cyst size which is computed using the 'Area' property in the 'regionprops' MATLAB function. The percentage of **halo** that surrounds the cyst is computed by using again the five-level image that appears in Figure 3.15A. For halo, which was noticed to be very dark in Figure 3.14 and in the expected double-wall cysts in the dataset (e.g. cyst number 14 in Figure 3.13B), the five-level image is binarised by setting to zero the pixel intensity values that come within the last level and the rest are set to 1 as shown in Figure 3.15C.

Image_name	Cyst_no	Darkness	Halo	Diameter	Roundness	Cysts_count
P2__S9_25_img3	1	0.03	0.01	8	1.17	14
P2__S9_25_img3	2	0.08	0.02	9	1.1	14
P2__S9_25_img3	3	0	0.03	6	1.5	14
P2__S9_25_img3	4	0	0	8	1.11	14
P2__S9_25_img3	5	0.02	0.01	14	0.86	14
P2__S9_25_img3	6	0	0	7	1.36	14
P2__S9_25_img3	7	0	0	4	2.09	14
P2__S9_25_img3	8	0	0	8	1.18	14
P2__S9_25_img3	9	0.1	0	14	0.71	14
P2__S9_25_img3	10	0	0.01	7	1.11	14
P2__S9_25_img3	11	0.03	0.01	13	0.99	14
P2__S9_25_img3	12	0.29	0.05	11	0.93	14
P2__S9_25_img3	13	0.03	0.11	16	0.96	14
P2__S9_25_img3	14	0.28	0.18	11	1.05	14

Table 3.1 The table that is produced automatically for each segmented image containing quantitative parameters about each detected cyst (the detected cysts which appear in Figure 3.13).

Each detected cyst is taken alone and dilated with a disk structure element of radius four for normal sized cysts and of radius eight for massive cysts. These values were chosen empirically by a trial and error procedure. Halo area represents the difference between the dilation and the original cyst, as shown in Figure 3.15D. Now, the percentage of the halo is computed by counting the number of zeros (in the image that appears in Figure 3.15C) which comes within the location of halo and then divide the value by the halo area which is represented by the number of pixels in that area. The cyst **diameter**, which is computed using 'EquivDiameter' property in 'regionprops' MATLAB function, is a parameter measures the diameter of a circle with the same area as the cyst. Finally, **count** finds the total number of detected cysts in the whole image and it is computed using the 'bwlabel' MATLAB function. Moreover, it is possible to compute other quantitative parameters according to clinicians' request.

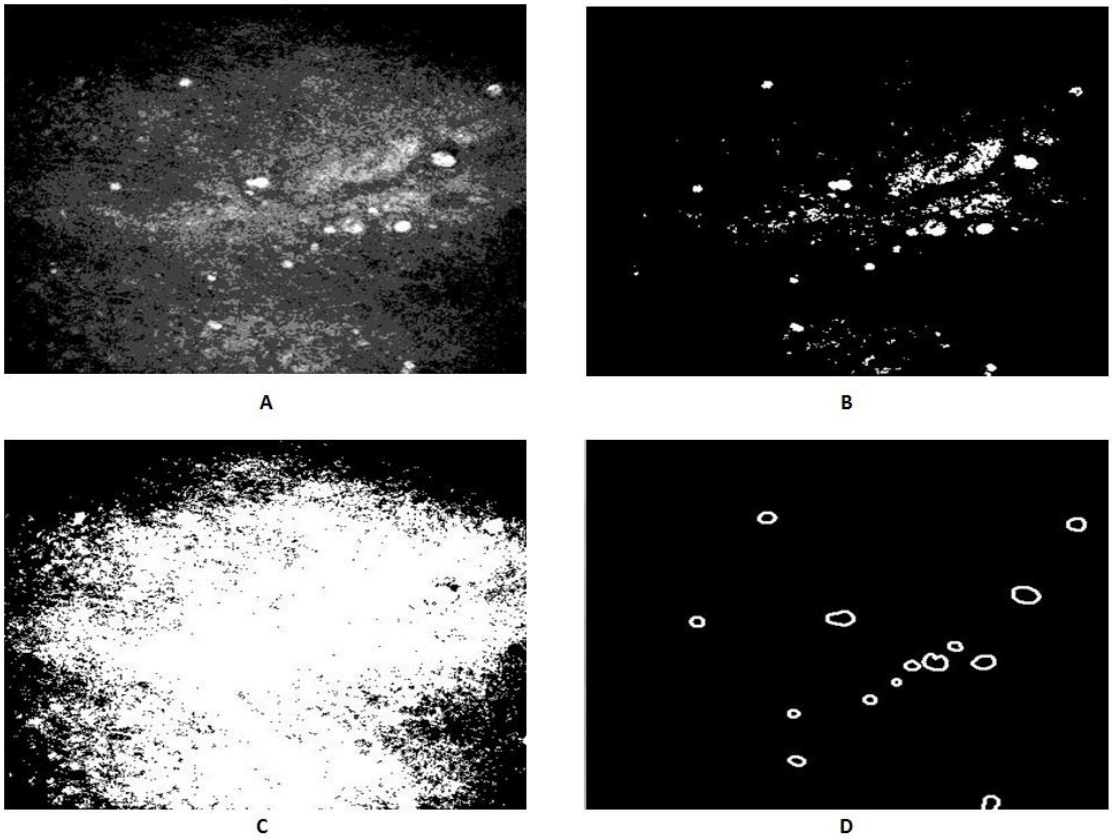

Figure 3.15 Procedure to calculate some quantitative parameters for Acanthamoeba cysts. A) Division of pixel intensities of the image into five levels using Otsu thresholding. B) Binarisation of the five-level image to compute the percentage of cyst darkness where all pixel intensity values come within the last three levels are converted to 0 and the rest are converted to 1. C) Binarisation of the five-level image to compute the percentage of cyst halo where all pixel intensity values come within the last level are converted to 0 and the rest are converted to 1. D) Estimated halo area surrounding each cyst of all detected cysts.

3.5. Results discussion and evaluation

Acanthamoeba image enhancement and segmentation phase is summarised in Figure 3.16. This process was applied to the dataset which contains 54 images from 13 subjects with Acanthamoeba keratitis and 8 images from one subject with normal healthy eyes. Each subject has a sequence of from 3 to 7 ordered images.

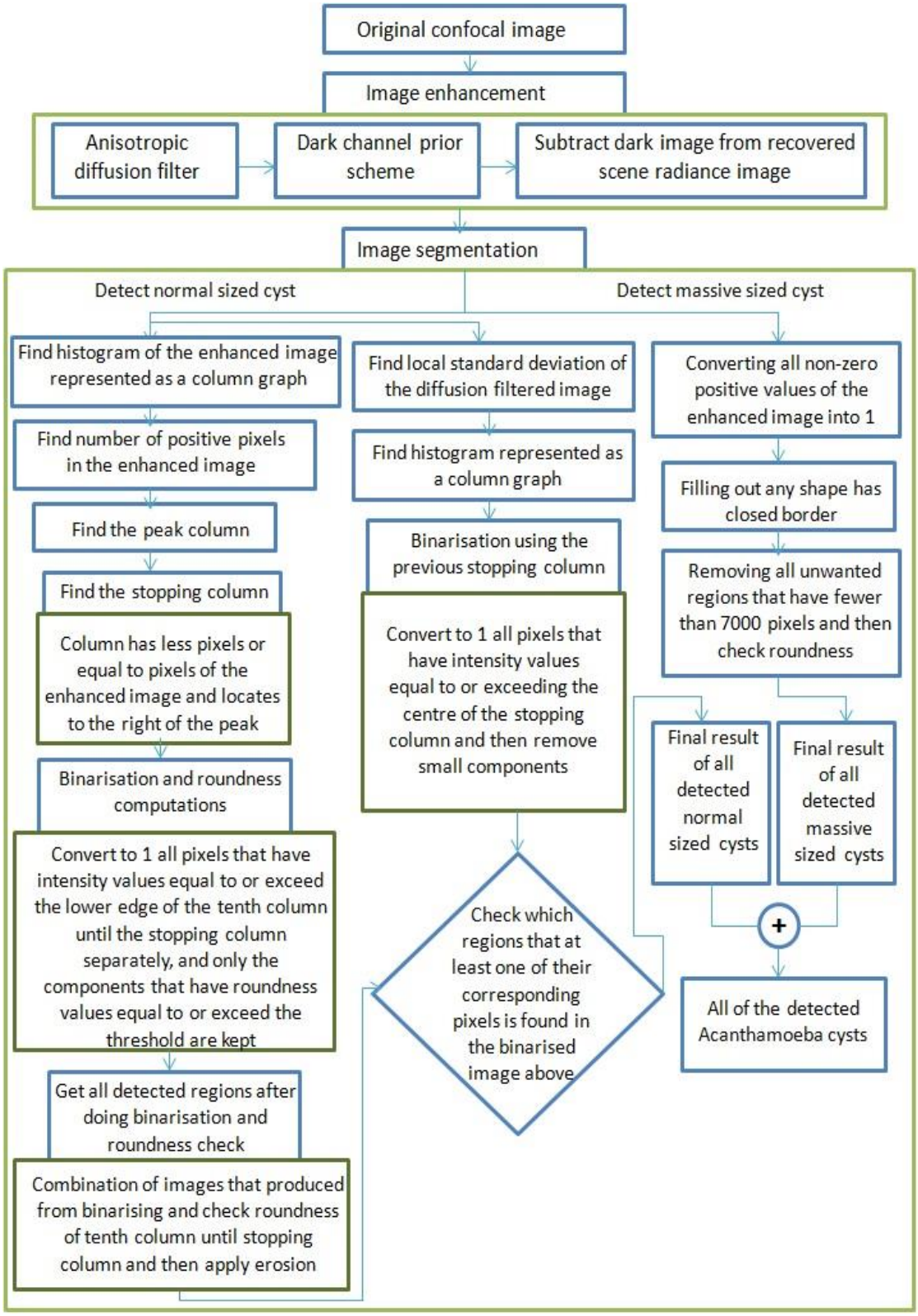

Figure 3.16 The proposed algorithm for Acanthamoeba image enhancement and segmentation.

The dataset of Acanthamoeba keratitis images was sent to the clinical consultant at Manchester Royal Eye Hospital (Dr Andrew Walkden) and he

circled the suspicious regions that are most likely to be Acanthamoeba cysts. Figure 3.17 shows the cysts detected by the proposed system in comparison to those circled by the clinical consultant (the rest of images appear in Appendix A). It is seen that most of the circled cysts are detected by the proposed system. Also, there are many cysts which are detected by the system and not circled by the clinician.

The performance of the segmentation process was evaluated by computing the positive predictive value (PPV) of cysts for each image as follows [58, 59]:

$$PPV = \frac{number\ of\ true\ positives}{number\ of\ true\ positives + number\ of\ false\ positives} \qquad Eq.3.10$$

The positive predictive values rate of cysts for all Acanthamoeba keratitis images in the dataset was 76%.

The researcher indicates that many of the detected cysts which were not circled by the clinician could be true positive cysts as these detected cysts appear in many images in the sequence (this idea is discussed more in Chapter 4) and they also have a similar appearance to the manually circled cysts.

In this context, it is imperative to quote what Dr Walkden has raised: "*there is no agreed way of deciding, from the confocal scan, which object is an Acanthamoeba cyst. There is no exact science to this; remember we use this scan in conjunction with our clinical suspicion, i.e., if the patient history and examination fits, if the corneal sample grows Acanthamoeba, etc.*" (A. Walkden, personal communication, Sept 5, 2016).

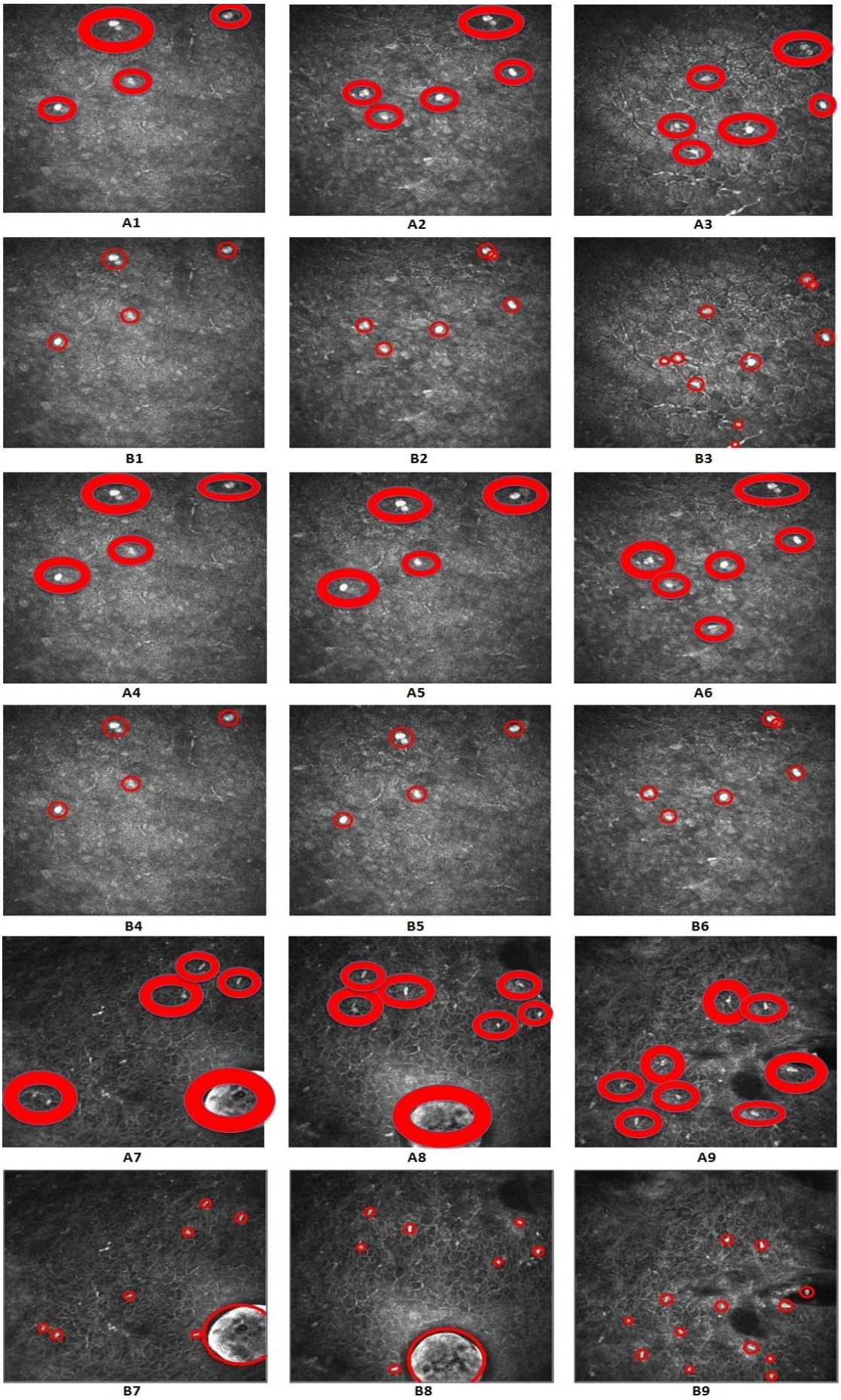
A1
A2
A3
B1
B2
B3
A4
A5
A6
B4
B5
B6
A7
A8
A9
B7
B8
B9

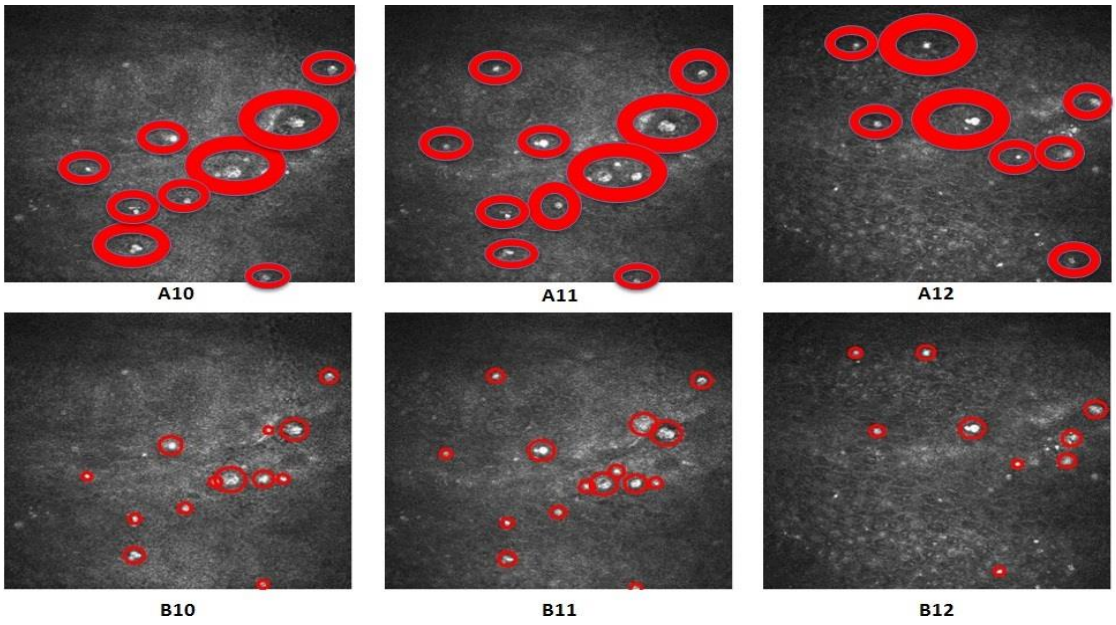

Figure 3.17 The performance of the proposed segmentation process for Acanthamoeba keratitis cysts in comparison to the manual segmentation. A1-A12) Manual detection of Acanthamoeba cysts by the clinical consultant. B1-B12) Automated detection of Acanthamoeba cysts by the developed system.

It can be concluded that confocal images are not used alone to determine Acanthamoeba cysts, and consequently, it is hard to determine an optimum segmentation or to say that such a segmentation algorithm is the best. However, other benchmarks to compare with would be helpful to evaluate the accuracy of the proposed system in detecting Acanthamoeba cysts. Unfortunately, the lack of benchmarks in the literature, whether manual or automated, was the main challenge of the evaluation process. As a result, a logical evaluation was carried out by applying the segmentation algorithm to normal healthy corneal images. The idea is to prove that the proposed algorithm is reliable and detects regions as cysts only in an abnormal epithelial layer that contains cysts and detects nothing in a normal epithelial layer that does not contain any cysts, except when nerves start to appear in the layer. The normal images that have been acquired are very close to the sub-basal nerve plexus and nerves appear in the images.

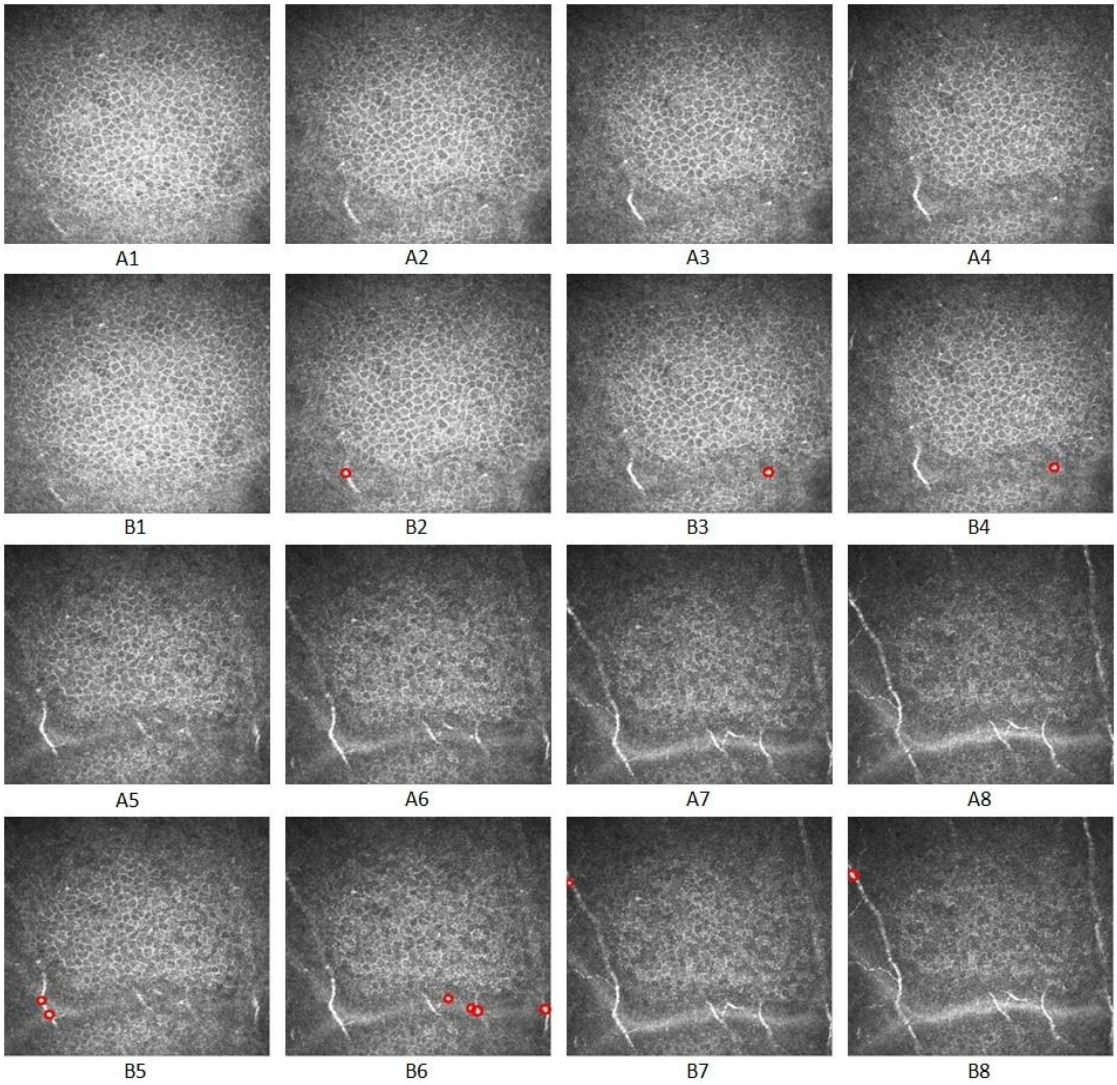

Figure 3.18 The logical evaluation of the proposed segmentation process by applying it to normal healthy corneal images. A1-A8) Original normal healthy corneal images. B1-B8) Result of applying the proposed segmentation process.

Those nerves are very bright and according to the proposed segmentation algorithm parts of them appear in the result as cysts because they are bright and exceed the roundness threshold. Figure 3.18 shows the original normal images and their result of segmentation.

The automated system proposed to detect Acanthamoeba faces two main challenges in the segmentation process:

1- If Acanthamoeba keratitis reaches stroma, which only happens in advanced cases, the developed system is not capable of distinguishing between Acanthamoeba cysts and stromal keratocytes nuclei, since keratocytes nuclei have the same appearance as cysts, see Figure 3.19. The interesting thing in this context is that many research studies mention this kind of confusion. For example, the authors of [12] excluded the round structures that could be confused with Acanthamoeba cysts such as inflammatory cells and epithelial cells based on their own prior experience or the characteristics described in the literature, but did not give any details. However, the authors of [11] mentioned that size, higher reflectivity, and contrast may help to distinguish between Acanthamoeba cysts and surrounding cells, but they also did not give any values to be used. Acanthamoeba cases in the study of [57] showed consistent features of Acanthamoeba, where the authors reported that Acanthamoeba are smaller and much more iridescent than corneal cells such as epithelial cells or keratocytes nuclei, but they did not give specific values related to these features.

2- Some images from the dataset and in a certain stage of the disease, Acanthamoeba cysts start to appear blurred and connected. In this case only few cysts can be segmented; this is possible when their binarisation level differs from adjacent ones or when connected ones have a similar binarisation level and still achieve the criterion of roundness. See Figure 3.20. This case was mentioned in the study of [42], where the authors reported IVCM images of an Acanthamoeba showing cysts in chains and clusters as shown in Figure 3.21.

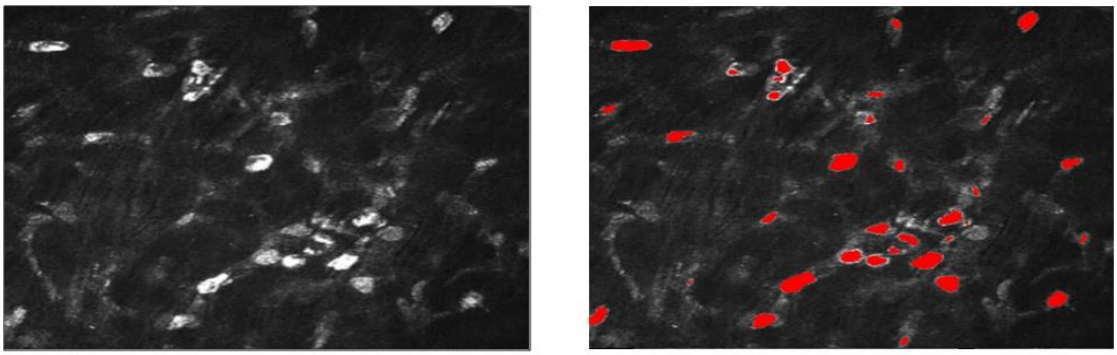

A B

Figure 3.19 Applying the system proposed to detect Acanthamoeba cysts to an image of the stromal layer from a patient with Acanthamoeba keratitis. A) Input image of the stromal layer from the dataset. B) The result of applying the proposed segmentation process.

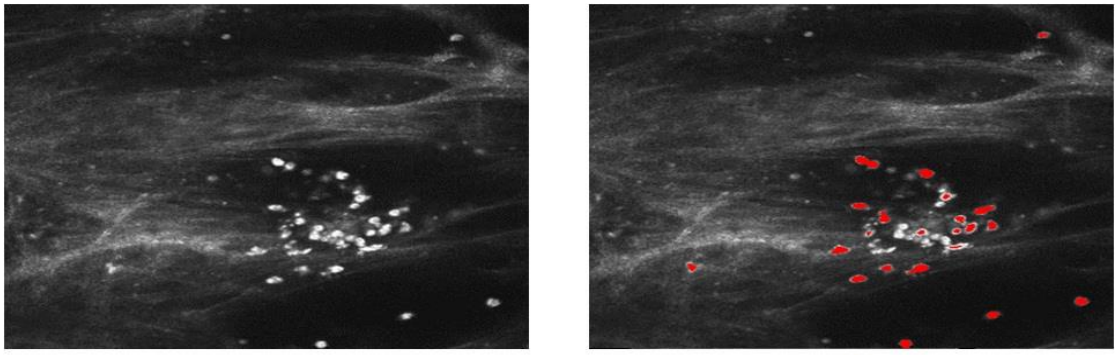

A B

Figure 3.20 Applying the system proposed to detect Acanthamoeba cysts to an image contains blurry connected Acanthamoeba cysts. A) Input image from the dataset contains blurry connected cysts. B) The result of applying the proposed segmentation process.

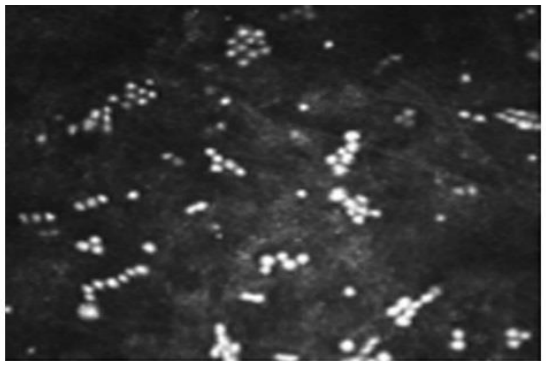

Figure 3.21 IVCM image of an Acanthamoeba showing cysts in chains and clusters [42].

The author of [42] considers that Acanthamoeba cysts start to form chains and clusters for a reason, such as treatment resistance, or that this is behaviour

in a certain stage of the disease means this case needs more attention and analysis. For this researcher, this could be a subject for a future work; to study the diffusion of cysts and to improve the segmentation scheme to capture the case of connected cysts.

3.6. Conclusion

Acanthamoeba confocal images suffer from blurriness and the appearance of artefacts (noise) which can be defined as any unwanted information appearing in the image and thus not a cyst. This unwanted information can result from mechanical contact with the cornea, motion of the cornea, light reflection from inflammatory cells, or cells of the corneal layers.

To reduce the artefacts, Acanthamoeba image processing starts with image enhancement where the diffusion filter and the simple idea of the dark channel prior were adopted. The diffusion filter has the capability to reduce image noise and smooth the image without removing significant parts that are important for the interpretation of the image. The adaptation that was done on the dark channel prior scheme contributed to produce more enhanced images with minimum unwanted information.

The level by level binarisation technique proposed in this research contributed to detecting most possible parts of the regions that are expected to be cysts especially those which were mostly dark. This technique helped as well to detect parts of blurry connected cysts.

After the enhancement and binarisation process, some regions detected as cysts needed to be excluded as not being relevant. Also in the case of normal epithelial images, some parts of the epithelial cells were detected as

cysts. For that reason, a refinement step was proposed to keep only the most expected regions that were considered as being cysts and to get rid of epithelial cells that are detected as cysts in normal images. This step is vital and it is the secret of making the segmentation process more accurate. It depends on producing the image from the local standard deviations of the diffusion filtered image. The local standard deviation image can clearly observe how most parts of the cyst or at least the bright border stand out in comparison to the background where the standard deviation is constantly low.

The proposed automated system that detects Acanthamoeba cysts in confocal microscopy images can help ophthalmologists in diagnosing Acanthamoeba keratitis, and in following-up the patient and consequently in assessing the treatment. The positive predictive values rate of cysts for all Acanthamoeba keratitis images in the dataset was 76%. However, this system faced many challenges such as the lack of benchmarks, and the confusion between Acanthamoeba cysts and other structures that have a similar appearance. On the other hand, lack of benchmarks can be considered one of the system's strengths as it will be the basis for any future work in the same field. Moreover, the system introduces a solution for the confusion problem by computing many measurements that may help to differentiate between cysts and other structures. It was not possible to go further with these measurements because there are no dedicated medical studies comparing the values of these measurements between Acanthamoeba cysts and the confusing structures. The author assumes that this research may encourage more medical imaging research in this field.

4. Registration and Cyst Tracking in Sequences of Acanthamoeba Images

4.1. Introduction

One of the ultimate goals of this research is to give ophthalmologists an indication of the depth of Acanthamoeba cysts, so that the ophthalmologist can detect how serious the disease is and get a clearer diagnosis for it. For that reason, there is a need to identify the region of interest (with cysts) across the sequence of images for such a patient regardless of scale, orientation and rotation.

Eye movement during the acquisition process, which mostly happens due to respiration and cardiac pulse, causes misalignment and shifts in the x-y plane of captured images [5, 35, 38]. Therefore, the importance of image registration rises in the analysis of confocal corneal images. The information obtained from the registration process for Acanthamoeba sequence of images is used to track each cyst in the sequential segmented images and detect its depth and therefore may provide an indicator of the stage of the disease.

Registration is an important process in image analysis where a new more informative image is obtained by integrating two or more images of the same object, possibly taken by different sensors, from different viewpoints, and/or at different times. The images to be registered may differ in orientation, rotation, and scale [5, 38].

The basis of the registration process is to find common features in the images of interest, and then to discover the transformation which will be used to align the images satisfactorily. In general, the image registration procedure goes through four main steps: a) prominent features detection, b) matching corresponding features between two images, c) generation of a mapping function and d) transforming one of the images to align with the other using the mapping function [5].

One of the most powerful and popular methods used to extract feature points in images, which are invariant to scale, rotation, illumination, and viewpoint, is the Scale Invariant Feature Transform (SIFT) [60]. The section below is dedicated to describing this technique in more detail.

4.2. Registration using the SIFT algorithm

SIFT is a technique for detecting salient and stable points in an image, each associated with a vector of low-level descriptors. These points are said to be key points and their descriptors are invariant under blur, rotation, shift, and scale, moderate changes in viewpoint, noise addition and in some cases under changes of illumination. The SIFT process can be summarised in four main steps [60-62]:

1) Scale-Space Extrema Detection: To create a scale space, the original image is taken and blurred progressively. SIFT resizes the original image to half size and again generates a blurred version. It keeps repeating this so that SIFT generates several Octaves of the original image; each Octave's image size is half that of the previous one. Within an Octave, images are progressively blurred using the Gaussian Blur operator. For each blurred image, its second

order derivatives are calculated (or the 'Laplacian'). This helps in locating edges and corners on the image, which are considered good for finding key points. Unfortunately, the second order derivative is extremely sensitive to noise. The scale space is used to generate the Laplacian of a Gaussian (LoG) image quickly by calculating the difference between two consecutive scales. These Differences of Gaussian image (DoG) are approximately equivalent to the Laplacian of Gaussian and have the advantage of replacing a computationally intensive process with a simple one (subtraction, fast and efficient). Two consecutive images in an Octave are picked and one is subtracted from the other. Then the next consecutive pair of images is taken, and the process repeats. This is carried out for all Octaves. The images produced are an approximation of scale invariant Laplacian of Gaussian (which is good for detecting key points). To detect the local maxima and minima, each pixel within the current image is compared with its eight neighbours at the same scale, and its nine neighbours up and down one scale (This way, a total of 26 checks are made). This pixel is marked as a "key point" if it is the greatest or least of all 26 neighbours. Usually, few initial checks will be sufficient to determine that a particular pixel is not a maximum or a minimum. The author of SIFT [60] recommends generating two such extrema images. Therefore, there is a need to produce exactly four DoG images and to do so, five Gaussian blurred images are needed to be generated and hence the five level of blurs in each Octave.

2) Keypoint Localisation: Once potential key points locations have been found, they have to be refined to get more accurate results. Some of these key points lie along an edge, or they may not have enough contrast. In both cases, they are not useful as features so they are removed. This helps increase the efficiency and robustness of the algorithm. To remove edges, two gradients

(perpendicular to each other) at the key point are calculated. The region around the key point can be one of three types: a) A flat region where both gradients will be small. b) An edge where one gradient will be big (perpendicular to the edge) and the other will be small (along the edge). c) A corner is where both gradients will be big. Corners are excellent key points and this is the desirable case. Otherwise, the key point is rejected. To remove low contrast features, the magnitude of the intensity at the current pixel in the DoG image (that is being checked for minima/maxima) is rejected if it is less than a certain value.

3) Orientation Assignment: To achieve invariance to image rotation, an orientation is assigned to each key point. A neighbourhood is taken around the key point location relying on the scale, and the gradient magnitude and direction is calculated in that region. An orientation histogram with 36 bins covering 360 degrees is identified. It is weighted by gradient magnitude and the window size, or the "orientation collection region", equal to the size of the kernel for Gaussian Blur of amount 1.5*sigma. The highest peak in the histogram is located. This highest peak and any other local peak within 80% of the highest are used to create a key point with that orientation. This creates key points with same location and scale, but different directions.

4) Keypoint Descriptor: The aim of this final step is to generate a kind of fingerprint that uniquely identifies the key points. To do this, a 16x16 window around a key point is taken. This 16x16 window is divided into 16 sub-blocks each of size 4x4. Within each sub-block, gradient magnitudes and orientations are calculated and are put into an 8 bin histogram. This result in a feature vector containing 128 elements. The first bin contains any gradient orientation in the range 0-44 degrees, and the second bin contains any gradient orientation in the

range 45-89 degrees, and so on. Once all 128 numbers have been generated, they are normalised (divided by the square root of the sum of squares). These 128 numbers form the 'feature vector' which identifies the key point uniquely. This feature vector introduces some complications; rotation dependence which is solved by subtracting the key point's rotation from each orientation, and illumination dependence which is solved by changing any number (of the 128) greater than 0.2 into 0.2. The resultant feature vector is normalised again.

In this research, the implementation of SIFT by Artiom Kovnatsky in [63] has been adopted. However, to make it applicable to the dataset of this work and to get the best results, values of many parameters were changed; mainly the count of sub-blocks for the window around the key point and count of orientation bins. According to this work's experiments, the best results were achieved with a 5 x 5 array of histograms, each with 12 orientation bins. So the descriptor of SIFT that is used here is 5 × 5 × 12 = 300 descriptors.

4.3. The proposed cyst tracking approach

As previously mentioned, confocal microscopy provides a sequence of images with a minimum depth separation of about 2 μm that show histological structure over the depth of corneal layers in health and disease. These images can be immediately viewed and used for diagnostic purposes.

To manage Acanthamoeba by providing a rapid diagnosis and consequently a treatment that can be initiated earlier, it is useful for clinicians to be provided with as much information about cysts as possible, such as their depths and their quantitative parameters.

Knowledge of cysts depths with some quantitative parameters gives the ophthalmologists a three-dimensional view of the disease, so they can estimate how serious it is and also the likely evolution of the disease and then decide how to start the treatment. This knowledge about cysts can be used not only for diagnosing the disease, but also for evaluating the effectiveness of the treatment.

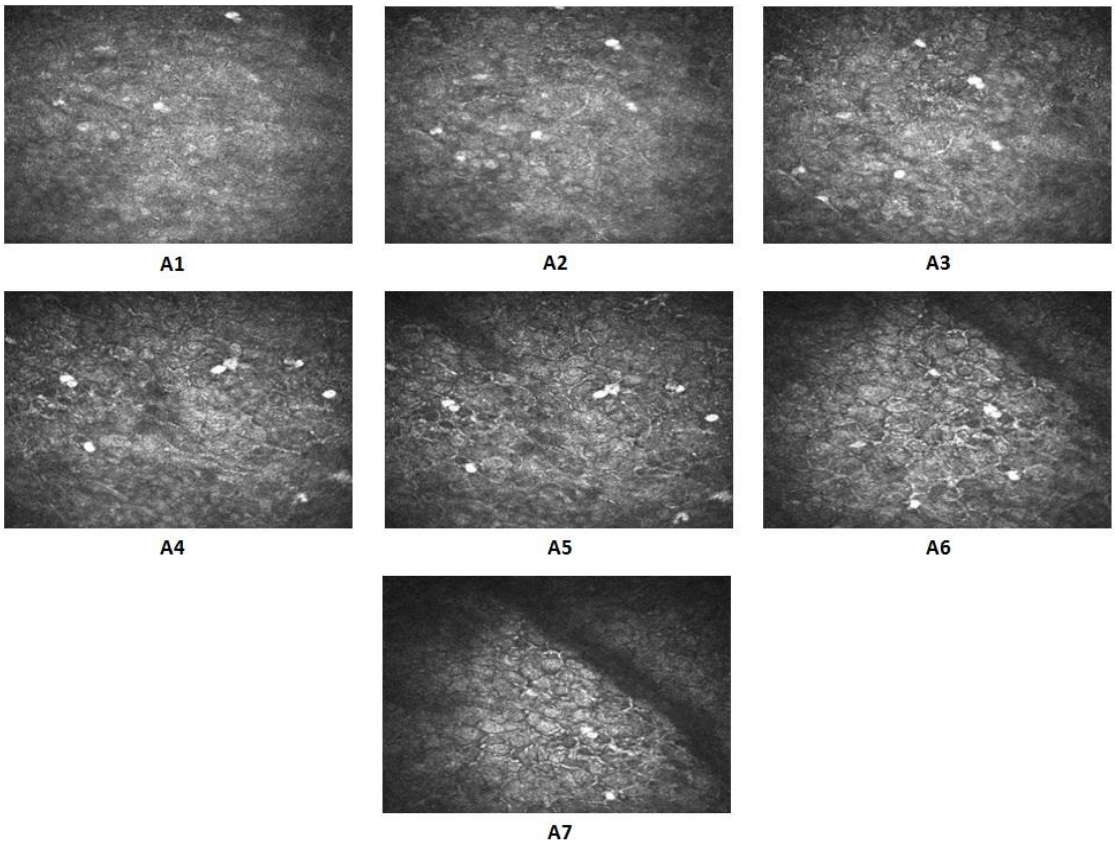

Figure 4.1 A sequence of ordered images for a patient with Acanthamoeba. A1-A7) used to demonstrate cyst tracking.

To estimate the depth of each cyst, there is a need to track each cyst sequentially from the first image in which it appears until the last image where it can be seen. An ordered sequence of seven images for such a patient is picked from the dataset (see Figure 4.1). To clarify the process of cyst tracking, the

steps are summarised in Figure 4.2 and are also demonstrated by describing a real example.

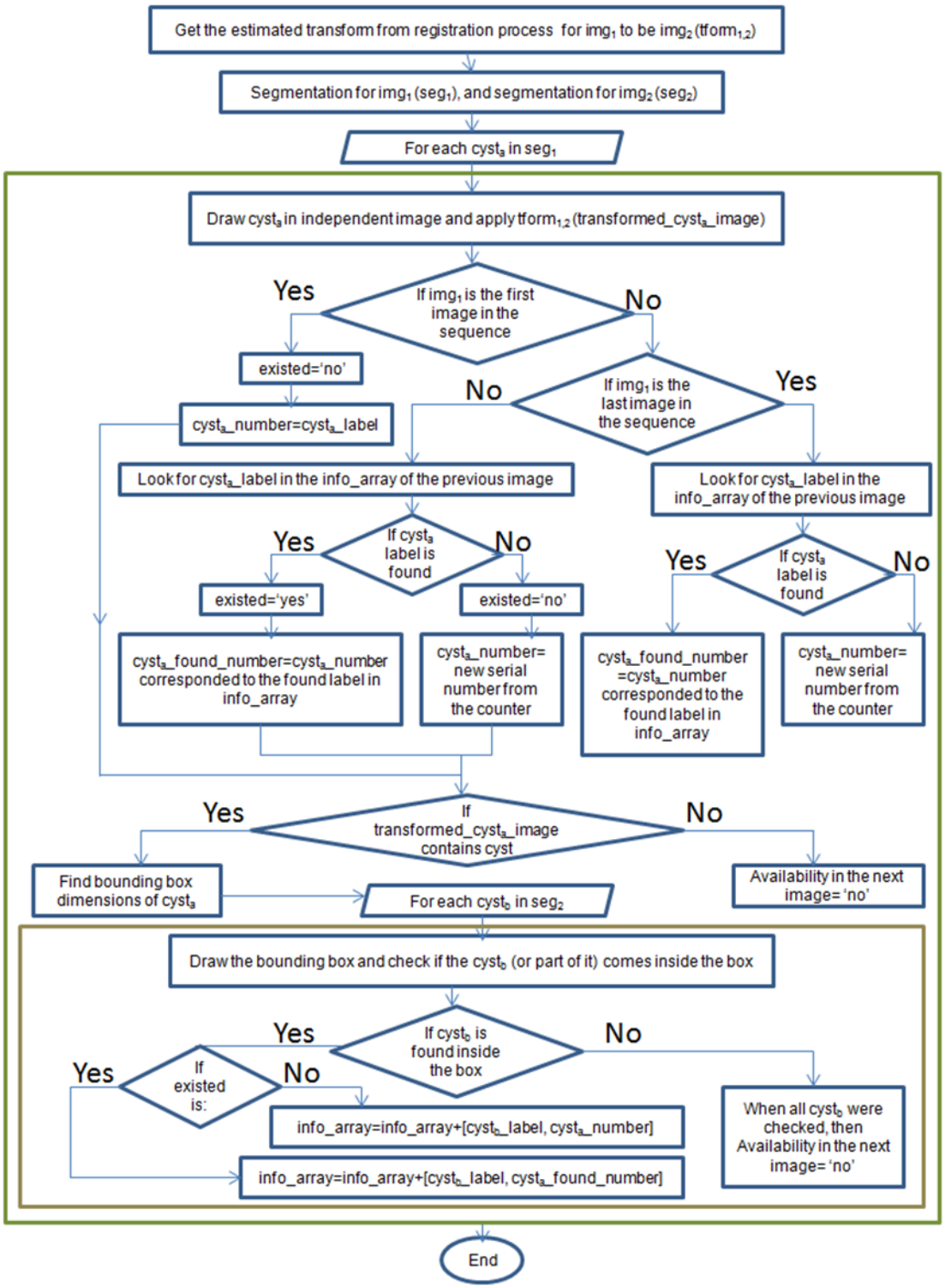

Figure 4.2 The proposed algorithm for cyst tracking in a sequence of Acanthamoeba images.

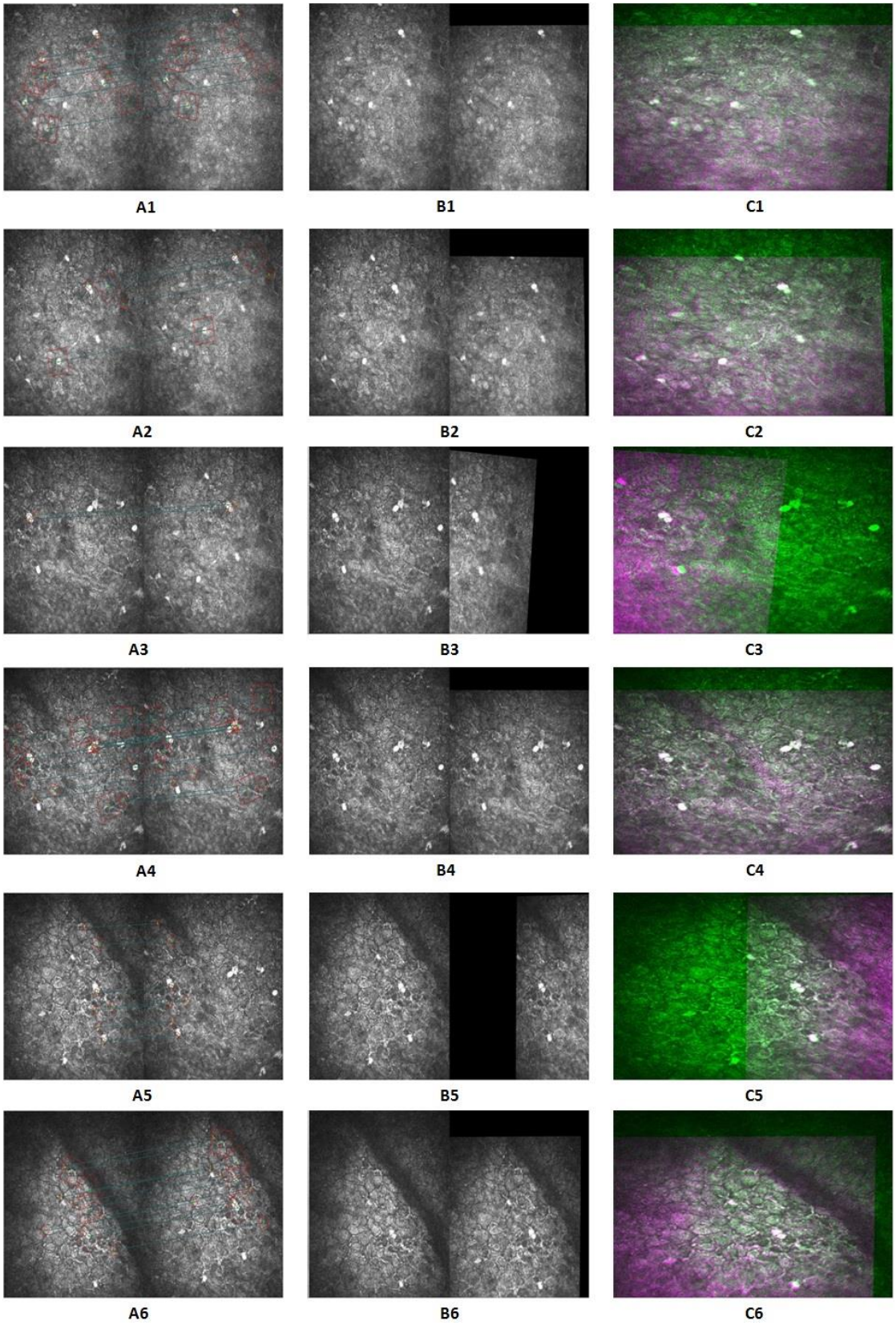

Figure 4.3 Estimating of geometric transformation between two consecutive images as a step in cyst tracking. A) Matching point pairs between the two images using SIFT. B) The image after applying the estimated geometric transformation lying beside the next image to be integrated with. C) The combination of the two images to be integrated that appear in (B). 1-6: covers the input images appear in Figure 4.1; A1 and A2, A2 and A3, A3 and A4, A4 and A5, A5 and A6, A6 and A7 respectively.

The proposed algorithm for cyst tracking starts by applying the registration process on the sequence of images. The aim here is to get the geometric transform for each image to make it aligned with the next image. Consequently, corresponding points (in terms of cysts) are being matched. Figure 4.3A shows the matching point pairs between each image and the next image, and Figure 4.3B shows the image after applying the estimated geometric transformation lying beside the next image to be integrated with, while Figure 4.3C combines the two images appearing in Figure 4.3B to show the integration.

The second phase, after estimating geometric transform for two images ($image_1$ and $image_2$), is to apply the segmentation process to these two images as shown in Figure 4.4. Now for each detected $cyst_a$ in $segmented\_image_1$, $cyst_a$ is drawn on an independent image as shown in Figure 4.5A (using 'PixelList' property of 'regionprops' MATLAB function to determine the location of the $cyst_a$ pixels) and the geometric transformation applied to that image to get the $transformed\_cyst_a\_image$ as shown in Figure 4.5B.

If $image_1$ is the first image in the sequence, then $cyst_a$ is not found in the previous image because there is no previous image and $cyst_a\_number=cyst_a\_label$ (the cyst_label is got by using the 'bwlabel' MATLAB function). If the $transformed\_cyst_a\_image$ contains $cyst_a$ or part of it, then the dimension of the bounding box for $cyst_a$ are found using the 'BoundingBox' property of 'regionprops' MATLAB function as shown in Figure 4.5C. Now the procedure tries to find $cyst_b$ in the $segmented\_image_2$ lying fully or partially within the same dimension of the bounding box of $cyst_a$ (see Figure 4.5, D-F).

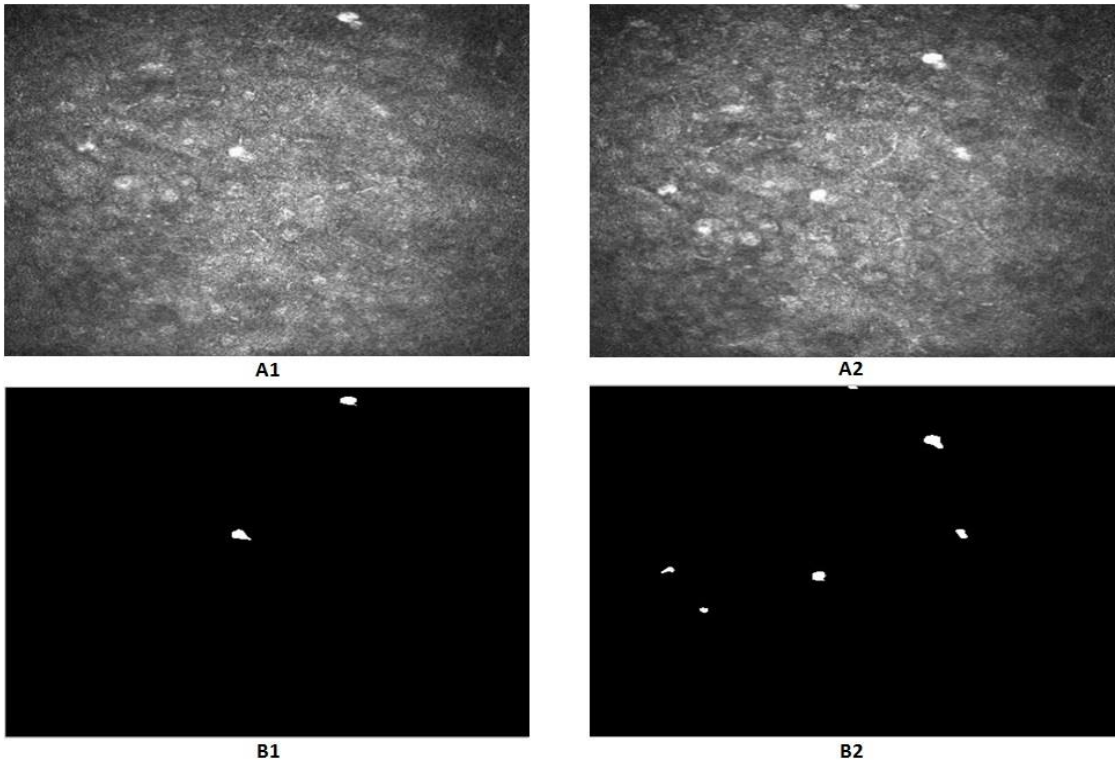

Figure 4.4 Applying the segmentation process to two consecutive images in the sequence. A1) Input $image_1$. A2) Input $image_2$. B1) $Image_1$ that appears in (A1) after segmentation. A2) $Image_2$ that appears in (A2) after segmentation.

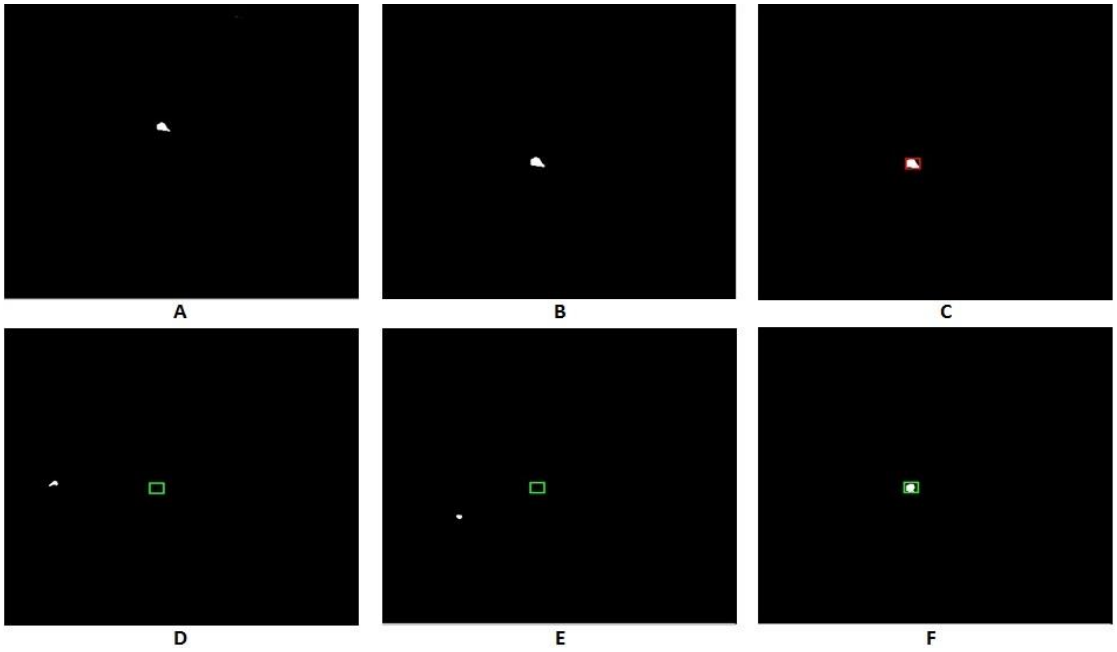

Figure 4.5 Tracking of the first cyst appears in $segmented\_image_1$ to get its label in $segmented\_image_2$. A) The cyst to be tracked that appears in $segmented\_image_1$. B) The transformed_cyst_image after applying the computed geometric transformation to the image (A). C) The bounding box for the cyst appears in the image (B). D-F) Trying to find a cyst in $segmented\_image_2$ lying fully or partially within the same dimension of the bounding box of the cyst that is being tracked.

If no $cyst_b$ is found, then this means that $cyst_a$ is not available in the next image and its tracking stops here, while if $cyst_b$ is found, then info_array=info_array+[$cyst_b$_label, $cyst_a$_number]. This procedure is repeated for all of existing cysts in the segmented_$image_1$ (see Figure 4.6). According to the illustrative example and at the end of this step, the value of info_array=[3 1; 5 2].

If $image_1$ is neither the first image nor the last image in the sequence, then there is a need to look for $cyst_a$_label in the info_array of the previous image. If the label is not found, then (existed='no') and $cyst_a$_number= $cyst_a$_number+1 (this means $cyst_a$ is a new appearance in the sequence and it gets a new number from the numbering series). Whereas, if the label is found, then (existed='yes') and $cyst_a$_found_number=$cyst_a$_number corresponded to the found label in info_array of the previous image. After that, for both cases (label is found and not found), if transformed_$cyst_a$_image contains $cyst_a$ or part of it, then the dimension of the bounding box for $cyst_a$ is found (using the 'BoundingBox' property of the 'regionprops' MATLAB function). Now, the procedure tries to find $cyst_b$ in segmented_$image_2$ that lies fully or partially within the same dimension of bounding box of $cyst_a$. If no $cyst_b$ is found in the box, then this means that $cyst_a$ is not available in the next image and its tracking stops here, while if $cyst_b$ is found, then info_array=info_array+[$cyst_b$_label, $cyst_a$_number] in the case that existed='no'. In the case that existed='yes', info_array=info_array+[$cyst_b$_label, $cyst_a$_found_number]

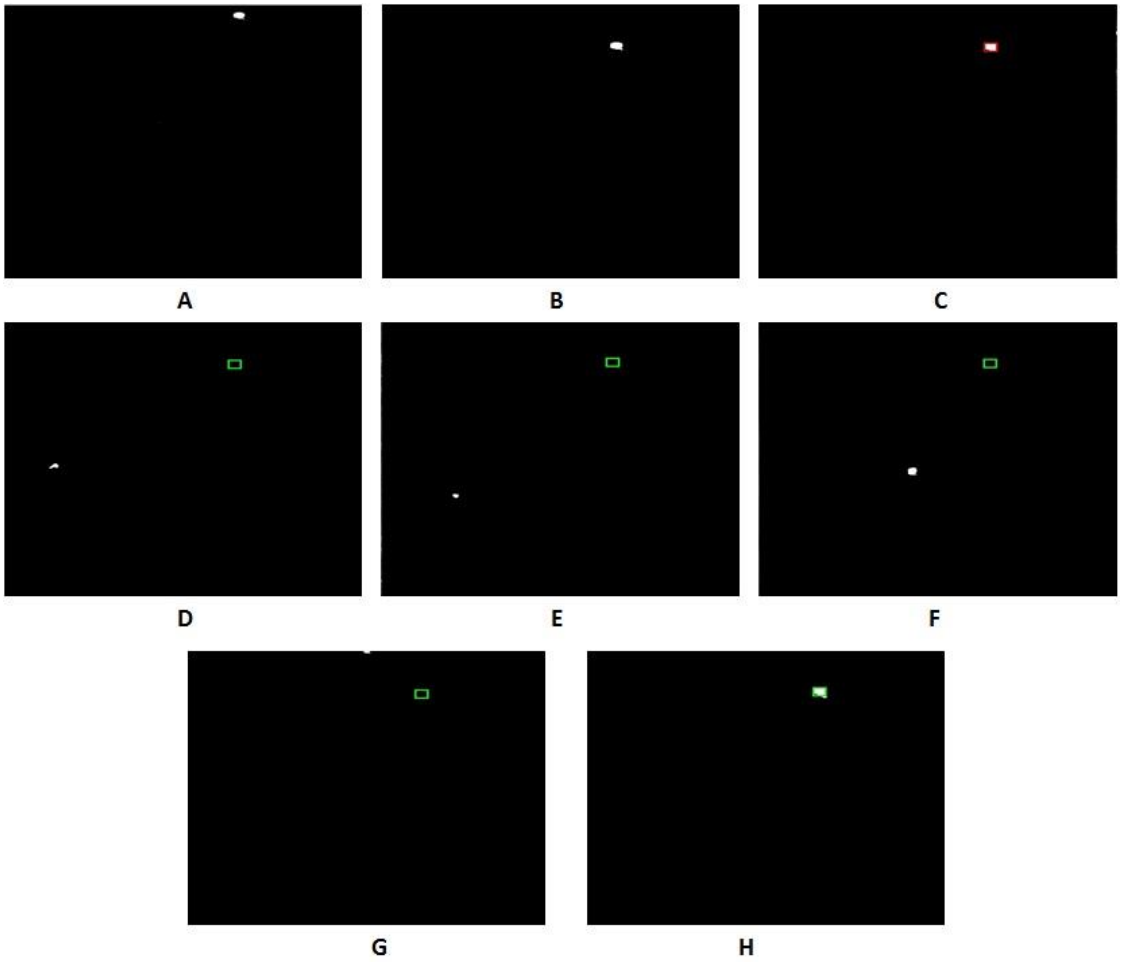

Figure 4.6 Tracking of the second cyst appears in segmented_image$_1$ to get its label in segmented_image$_2$. A) The cyst to be tracked that appears in segmented_image$_1$. B) The transformed_cyst_image after applying the computed geometric transformation to the image (A). C) The bounding box for the cyst appears in the image (B). D-H) trying to find a cyst in segmented_image$_2$ lying fully or partially within the same dimension of the bounding box of the cyst that is being tracked.

If image$_1$ is the last image in the sequence, then there is a need to look for cyst$_a$_label in the info_array of the previous image. If the label is not found, then cyst$_a$_number=cyst$_a$_number+1 (this means cyst$_a$ is a new appearance in the sequence and it gets a new number from the numbering series). Whereas, if the label is found, then cyst$_a$_found_number=cyst$_a$_number corresponded to the found label in info_array.

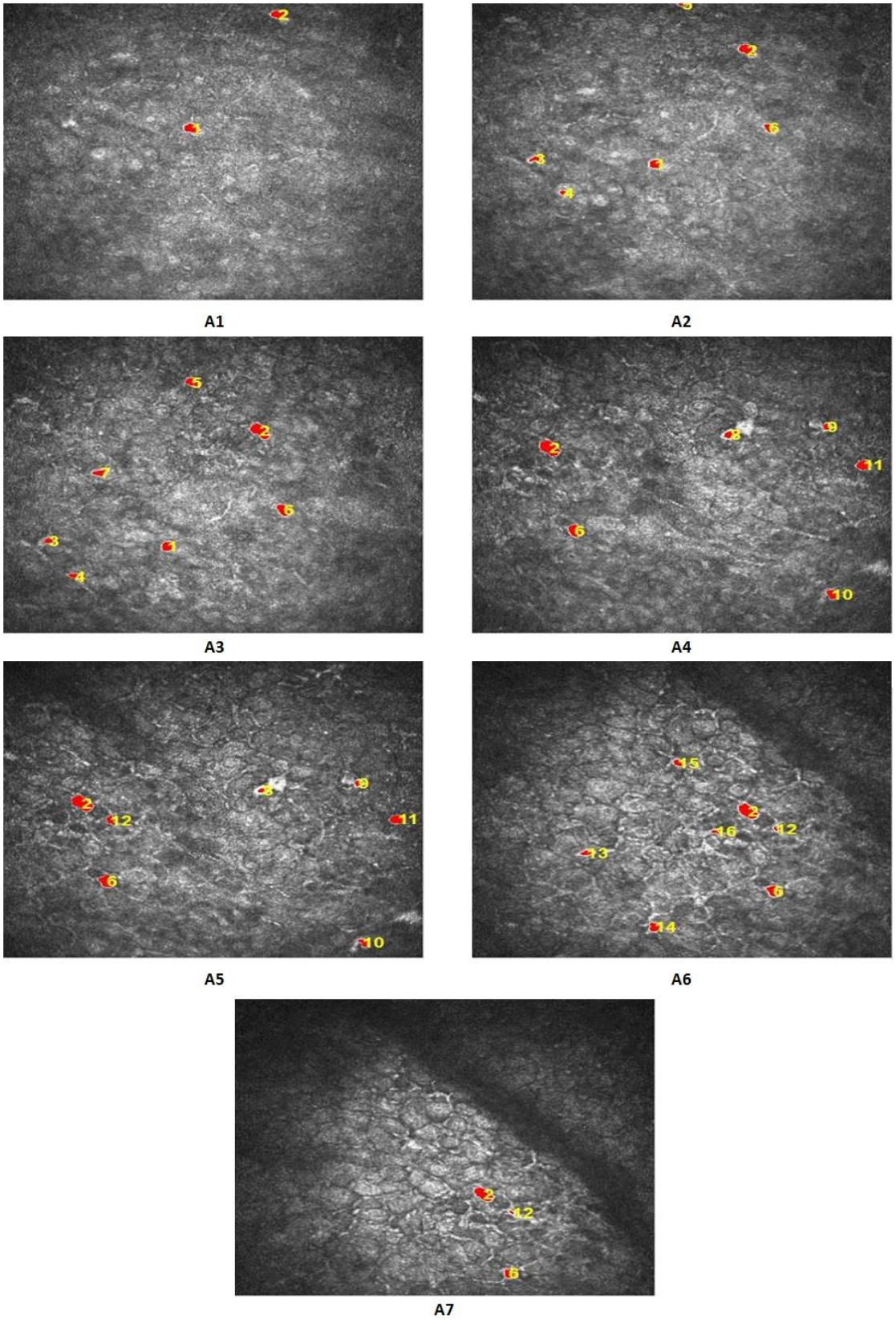

Figure 4.7 Results of applying the proposed algorithm of cyst tracking in a sequence of images. A1-A7) The detected cysts in each image in the sequence are coloured and have their track number displayed.

Figure 4.7 shows the final result of applying the proposed tracking algorithm on the sequence appears in Figure 4.1. For visualisation issues, the sequence of all images is shown in Figure 4.8. Also, each cyst is coloured and has its tracking number.

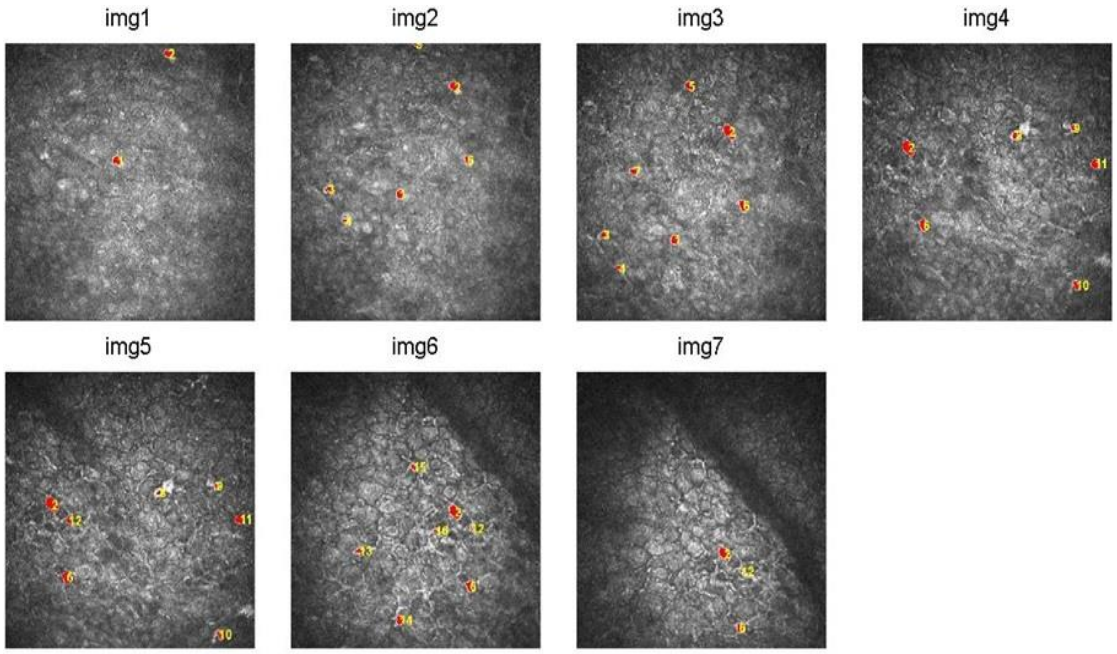

Figure 4.8 All the results of applying the proposed algorithm of cyst tracing in a sequence of images are shown in one Figure.

Cyst_track_no	Count of images	Depth in micron_start	Depth in micron_end	Images_filenames
1	3	0	10	P11__S15_2-6_img1, P11__S15_2-6_img2, P11__S15_2-6_img3
2	7	0	30	P11__S15_2-6_img1, P11__S15_2-6_img2, P11__S15_2-6_img3, P11__S1
3	2	5	10	P11__S15_2-6_img2, P11__S15_2-6_img3
4	2	5	10	P11__S15_2-6_img2, P11__S15_2-6_img3
5	2	5	10	P11__S15_2-6_img2, P11__S15_2-6_img3
6	6	5	30	P11__S15_2-6_img2, P11__S15_2-6_img3, P11__S15_2-6_img4, P11__S1
7	1	10	10	P11__S15_2-6_img3
8	2	15	20	P11__S15_2-6_img4, P11__S15_2-6_img5
9	2	15	20	P11__S15_2-6_img4, P11__S15_2-6_img5
10	2	15	20	P11__S15_2-6_img4, P11__S15_2-6_img5
11	2	15	20	P11__S15_2-6_img4, P11__S15_2-6_img5
12	3	20	30	P11__S15_2-6_img5, P11__S15_2-6_img6, P11__S15_2-6_img7
13	1	25	25	P11__S15_2-6_img6
14	1	25	25	P11__S15_2-6_img6
15	1	25	25	P11__S15_2-6_img6
16	1	25	25	P11__S15_2-6_img6

Table 4.1 The table that is produced automatically for the tracked cysts.

To keep a reference to the tracked cysts, a file is created and saved automatically by the system. It contains useful information about each cyst; the track number, the count of images it appear in, the depth where it first appear, the depth where it last appear, and the filenames of images that contain the cyst (see Table 4.1).

4.4. Parameters for the quantitative analysis of tracked cysts

Many parameters are extracted for the detected cysts in a sequence of ordered images which include the filename of each processed image, cyst number, cyst track number, the percentage of cyst darkness, cyst diameter, cyst roundness, the percentage of cyst halo, availability of cyst in the next image, and the total count of detected cysts in each processed image. Table 4.2 shows this information for the processed sequence of images that appear in Figure 4.7.

Cyst number, the percentage of cyst darkness, cyst diameter, cyst roundness, the percentage of cyst halo, and the total count of detected cysts in each processed image were explained in Section 3.4. Cyst track number gives the number of each tracked cyst in the processed image according to the sequence, so the cyst gets the same number as long as it keeps coming into view in the sequence. Availability of cyst in the next image has 'yes' value when a cyst is been found in the next image with the same location of the processed cyst, otherwise, it has 'no' value.

image_name	cyst_no	Cyst_track_no	darkness	Diameter	roundness	halo	availability in next image	cysts_count
P11__S15_2-6_img1	1	1	0	13	0.77	0	yes	2
P11__S15_2-6_img1	2	2	0	12	0.8	0.1	yes	2
P11__S15_2-6_img2	1	3	0	8	0.73	0	yes	6
P11__S15_2-6_img2	2	4	0	7	1.16	0	yes	6
P11__S15_2-6_img2	3	1	0	12	0.93	0	yes	6
P11__S15_2-6_img2	4	5	0	6	1.09	0.16	yes	6
P11__S15_2-6_img2	5	2	0	14	0.79	0.01	yes	6
P11__S15_2-6_img2	6	6	0	10	0.9	0	yes	6
P11__S15_2-6_img3	1	3	0	9	0.64	0	no	7
P11__S15_2-6_img3	2	4	0	9	0.92	0.04	no	7
P11__S15_2-6_img3	3	7	0	11	0.77	0	no	7
P11__S15_2-6_img3	4	1	0	12	0.99	0	no	7
P11__S15_2-6_img3	5	5	0	12	0.91	0.05	no	7
P11__S15_2-6_img3	6	2	0	17	0.75	0.02	yes	7
P11__S15_2-6_img3	7	6	0	13	0.89	0	yes	7
P11__S15_2-6_img4	1	2	0.01	18	0.81	0.09	yes	6
P11__S15_2-6_img4	2	6	0	14	0.88	0	yes	6
P11__S15_2-6_img4	3	8	0	11	0.89	0	yes	6
P11__S15_2-6_img4	4	9	0	9	1.15	0.05	yes	6
P11__S15_2-6_img4	5	10	0	11	0.91	0.02	yes	6
P11__S15_2-6_img4	6	11	0	14	0.99	0.12	yes	6
P11__S15_2-6_img5	1	2	0.01	19	0.72	0.03	yes	7
P11__S15_2-6_img5	2	6	0	15	0.91	0.02	yes	7
P11__S15_2-6_img5	3	12	0	9	0.63	0	yes	7
P11__S15_2-6_img5	4	8	0	9	0.92	0	no	7
P11__S15_2-6_img5	5	9	0	8	1.08	0	no	7
P11__S15_2-6_img5	6	10	0	9	0.79	0	no	7
P11__S15_2-6_img5	7	11	0	14	0.99	0.14	no	7
P11__S15_2-6_img6	1	13	0	9	0.81	0	no	7
P11__S15_2-6_img6	2	14	0	12	0.96	0	no	7
P11__S15_2-6_img6	3	15	0	9	0.97	0.01	no	7
P11__S15_2-6_img6	4	16	0	6	0.92	0	no	7
P11__S15_2-6_img6	5	2	0	18	0.79	0	yes	7
P11__S15_2-6_img6	6	6	0	13	0.86	0	yes	7
P11__S15_2-6_img6	7	12	0	5	1.02	0	yes	7
P11__S15_2-6_img7	1	2	0	16	0.69	0	no	3
P11__S15_2-6_img7	2	6	0	11	0.95	0	no	3
P11__S15_2-6_img7	3	12	0	5	1.35	0	no	3

Table 4.2 The table that is produced automatically to show parameters used in quantitative analysis of the tracked cysts.

4.5. Results discussion and evaluation

The Acanthamoeba image registration and cyst tracking phase was applied to 54 images from 13 subjects with Acanthamoeba keratitis. Each subject has an ordered sequence of images ranging in number from 3 to 7.

The registration process relies on the SIFT algorithm, which is relatively slow but very accurate. To assess SIFT accuracy; the algorithm has been tested on 17 images which were picked randomly from the 15 subjects. The test was carried out after applying random rotation and scaling of each image. The percentage of scale means the percentage of resizing, and the minimum

percentage used in the evaluation process was about 50%. The results appear in Table 4.3. The difference (in rotation and scaling) between the applied transformation and the detected one after SIFT is very low and does not exceed 0.02 for scale, 2.99 for rotation except in one case, it reached 0.03 for scale and 8.07 for rotation.

The cyst tracking was accurate as well; it uses the result of the registration process that aligns the sequence of images for each patient on the top of each other to get a three-dimensional view of the disease. Each detected cyst after segmentation is tracked in the rest of segmented registered images using its location. The evaluation of this stage was achieved by observations which were done by the researcher and the clinicians.

Name of the original image	Scale percentage applied to the image	Rotation in degrees applied to the image	Result of scale percentage after SIFT	Result of rotation in degrees after SIFT	Absolute difference of scale percentage	Absolute difference of rotation in degrees
P2_img3	0.93	-18	0.92	-18.32	0.01	0.32
P13_img1	0.85	10	0.84	9.49	0.01	0.51
P3_img3	0.87	17	0.88	19.15	0.01	2.15
P11_img5	0.8	22	0.79	21.93	0.01	0.07
P11_img7	0.6	28	0.59	28.02	0.01	0.02
P12_img3	0.63	35	0.64	34.84	0.01	0.16
P1_img2	0.89	11	0.92	19.07	0.03	8.07
P14_img1	0.77	-12	0.77	-11.71	0	0.29
P14_img4	0.68	-18	0.67	-18.02	0.01	0.02
P15_img2	0.55	24	0.55	24.78	0	0.78
P15_img4	0.78	-33	0.77	-32.98	0.01	0.02
P1_img5	0.72	-35	0.71	-35.47	0.01	0.47
P7_img1	0.7	31	0.69	31.56	0.01	0.56
P9_img3	0.75	27	0.74	27.2	0.01	0.2
P10_img4	0.65	15	0.65	14.8	0	0.2
P4_img2	0.66	38	0.66	37.51	0	0.49
P5_img2	0.58	29	0.56	26.01	0.02	2.99

Table 4.3 Results of scale and rotation values found using SIFT after running the algorithm on 17 randomly selected images from the dataset that have been scaled and rotated using random values.

It is important to mention that confocal images can show the same cyst in different slices with different reflectivities and sizes depending on the cross

section it was taken from. Consequently, a few cysts were missed at certain levels in the process of tracking in some cases:

1- During the segmentation phase: sometimes a cyst in an image in the sequence is not reflective enough to be detected; or it is detected as a very small area and then removed by the morphological operations; or it is connected with other cyst(s) and the circularity of these connected cysts do not exceed the threshold; or maybe some cysts start to appear connected and then at another level they disconnect.
2- At the registration phase, it is sometimes hard to get an exact match of locations between all of the corresponding cysts of two registered images. In the case where one cyst is detected as a small area and the corresponding cyst in the previous image is bigger with a shift in location, then it is hard to track this cyst and to give the small one the same track number as the big one.
3- At the registration phase as well, it is possible to get the wrong matching between detected key points of two images and this leads to wrong scaling and rotation which ends up with wrong registration. This case mostly happens when a sequence of images to be registered is not ordered in the right way. In the sequence of images of this research's dataset which was ordered manually, this did not happen.

4.6. Conclusion

Image registration is a vital process aiding further analysis in a diagnostic system where a new and more informative image is obtained by integrating two images that may differ in orientation, rotation, and scale. Image registration is used in this research to align the sequence of images for such a patient on top

of each other to estimate the depth of the detected Acanthamoeba cysts and thus provide the ophthalmologist with a three-dimensional visualization for those cysts.

SIFT is the registration technique that was chosen in this research. Although slow, it is a very accurate technique, and it was very effective in the developed diagnostic system of this research. According to the experiments of SIFT's author, the best results were achieved with a 4×4 array of histograms with 8 orientation bins in each. So the descriptor of SIFT that was used is: 4×4×8=128 descriptors. While in this research, the best results were achieved with a 5×5 array of histograms, each with 12 orientation bins. So the descriptor of SIFT that is used here is 5×5×12=300 descriptors.

After registration, each detected cyst was tracked to get its depth and number of images it appeared in. This is used as evidence of a cyst’s reliability. The tracking ended up with quantitative analysis for the detected cysts which includes the filename of each processed image, cyst number, cyst track number, the percentage of cyst darkness, cyst diameter, cyst roundness, the percentage of cyst halo, the availability of cyst in the next image, and the total count of detected cysts in each processed image.

Registration itself is not an aim of this research, but registered images were used to track Acanthamoeba cysts and thus estimate the level of the infection and SIFT was able to achieve accurate results. For that reason, and because of the lack of available time, the author did not test more registration methods. In the future, there is a suggestion to investigate other registration techniques to overcome the main disadvantage that SIFT suffers from which is the long time it takes to do the job.

5. Fusarium Images Enhancement and Segmentation

5.1. Introduction

Confocal microscope images of Fusarium are not ready for straightforward segmentation. They suffer mainly from non-uniform illumination, unwanted information, which could be hyper-reflective inflammatory cells or the original layer cells, appearing prominently close to the hyphae, and other artefacts, which all make the detection of the Fusarium hyphae harder, see Figure 5.1, A1-A3. For this reason, there is a strong need to prepare the images for the segmentation process by pre-processing them to enhance and to improve their quality. Segmentation of the Fusarium images separates the hyphae from the background and simplifies the measurement of hyphal quantitative parameters.

Section 5.2 covers the procedure used for enhancing Fusarium images by reducing blurring and unwanted information, while the segmentation algorithm proposed for detecting Fusarium hyphae is described in section 5.3. Section 5.4 evaluates and discusses the results obtained after applying the proposed approaches of enhancement and segmentation on the dataset. Section 5.5 analyses the quantitative parameters obtained for Fusarium hyphae and the Conclusion is presented in section 5.6.

5.2. Fusarium images enhancement

Image enhancement seeks to improve the quality of an image [43]. There are large numbers of image enhancement techniques available, however, the techniques used in this section were chosen with regard to the nature and the characteristics of the images that have been provided in the dataset. The focus

was in enhancing the illumination uniformity, improving Fusarium hyphae visibility, and reducing any information not belonging to the hyphae.

In order to address these problems, a contrast-limited adaptive histogram equalisation (CLAHE) technique was applied to the input image, then Gaussian filtering, and finally an anisotropic diffusion filter.

CLAHE is used to improve the visibility of Fusarium hyphae and enhance the local contrast of the image as apparent in Figure 5.1, B1-B3. CLAHE prevents over-amplification of noise in homogenous regions and facilitates the comparison of different areas of an image by enhancing the brightness level to a specific range. In CLAHE, the input image is partitioned into many non-overlapping small areas called tiles. The contrast of each tile is enhanced, so the histogram of the output region approximately matches a specific histogram shape. The neighbouring tiles are then combined to eliminate falsely generated boundaries [64, 65]. The input image is divided into 20 tiles (four rows and five columns) and each tile is processed to match the Rayleigh histogram distribution.

The enhanced-contrast image is then smoothed using the Gaussian filter. The effect is to blur the image while preserving well-defined edges [39], and this helps to reduce false artefacts and to reduce edge blurring in Fusarium images as shown in Figure 5.1, C1-C3. The degree of smoothing is determined by the standard deviation of the Gaussian σ which was set to 2 pixels.

For further smoothing and noise reducing, the Anisotropic Diffusion Filter which is explained in detail in section 3.2.2 has been adopted. The result of this step is shown in Figure 5.1, D1-D3.

The parameters values for the CLAHE method, Gaussian filter, and Anisotropic Diffusion Filter were chosen after an intensive empirical investigation of their impact on the segmentation result to make this as close as possible to that from manual segmentation. In other words, the selected values contributed to getting results with the least number of unwanted segments and the least number of disconnected Fusarium hyphae.

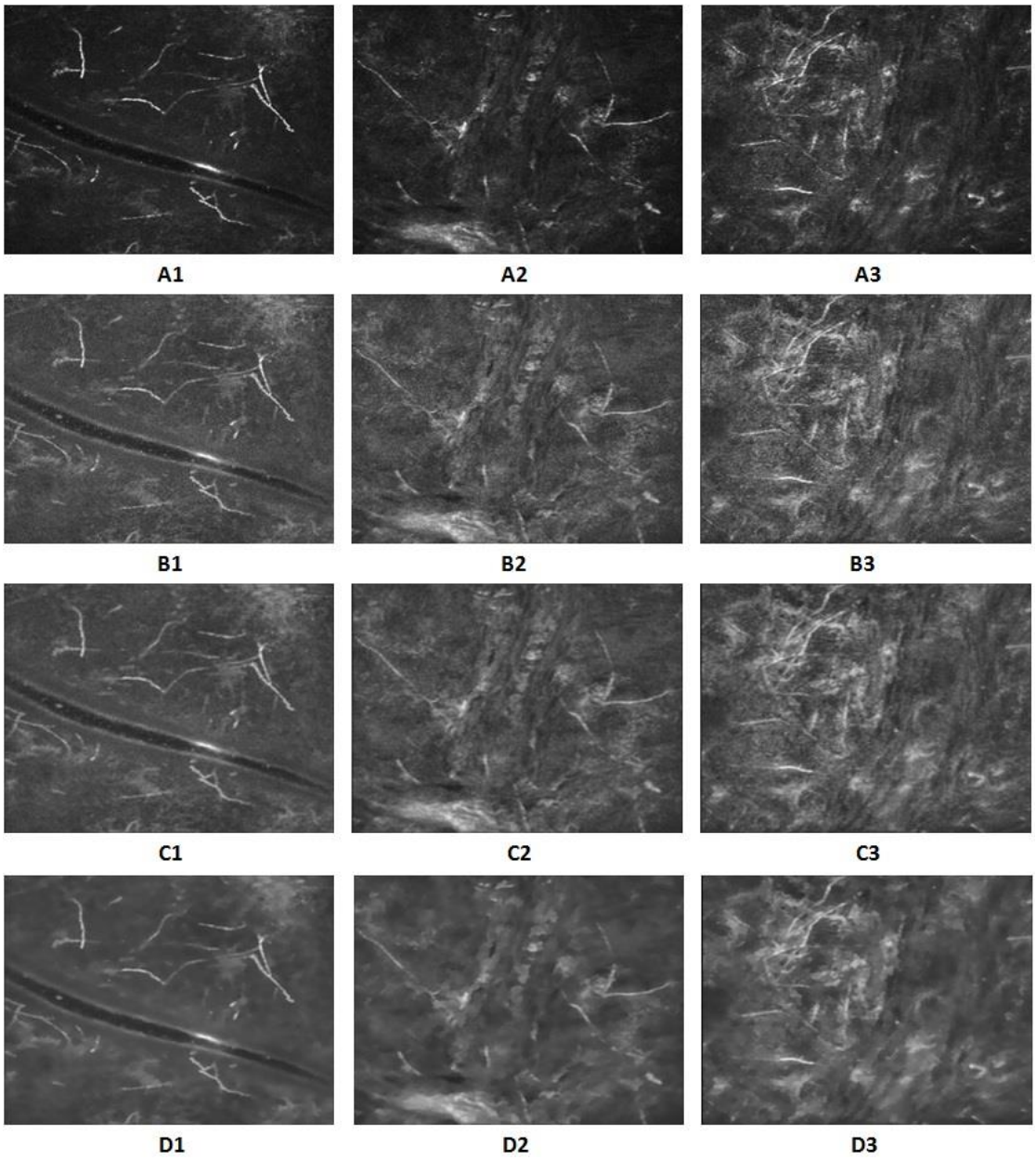

Figure 5.1 Enhancement steps for Fusarium image. A1-A3) Input images from the dataset. B1-B3) Contrast-limited adaptive histogram equalisation output. C1-C3) Gaussian filtering output. D1-D3) Anisotropic diffusion filter output.

5.3. Fusarium image segmentation

5.3.1 Overview

Image segmentation aims to isolate the objects of interest for a certain application [44]. The regions of interest in Fusarium confocal microscope images are represented in the appearance of hyper-reflective, thin, and branching hyphae as mentioned in section 2.2. Segmenting the hyphae from confocal microscope images is difficult due to low edge contrast and high image noise. The enhancement phase plays the main role in de-noising Fusarium images. To detect hyphae which have curvy line-like structures, the Coherence-Enhancing Diffusion filter (CED) was adopted. Instead of the scalar diffusivity function, which was explained in detail in Section 3.2.2, CED uses a tensor D which promotes anisotropic smoothing by acting mainly along the preferred structure direction in order to preserve interesting features [66, 67]. CED is one of two Anisotropic Diffusion filtering techniques introduced by Weickert [68]. The second is Edge-Enhancing Diffusion (EED). EED inhibits smoothing across edge structures but still diffuses along them [69], while CED has been specifically designed to enhance flow-like structures [70]. Many medical images segmentation studies [39, 66, 71] have used hybrid diffusion that combines EED and CED algorithms with continuous switches to exploit the benefits of both techniques; noise is filtered, while edges, tubular structures and small spherical structures are preserved. For this work, hybrid diffusion was not efficient. When it has been applied to the enhanced image, which is already smoothed and noise-filtered, the result was too smoothed; thus many hyphae parts were lost. The same effect was seen when it was applied to the original image or the contrast-improved one. Also, the hybrid diffusion didn't work well

on the Gaussian-filtered image, where the detected hyphae had extra filaments disconnection. CED was better in enhancing the fingerprint lines (with structures very similar to hyphae structures) without blurring junctions as demonstrated in Ref. [68, 70, 72]. Weickert [70] shows many examples which demonstrate that CED can close interrupted lines and enhance the flow-like character when the diffusion parameters are well-suited.

5.3.2 Coherence filtering

The coherence filtering method is an iterative edge preserving smoothing method that consists of two main steps. The first is to describe the image structure using a structure tensor. The second step is to transform the structure tensor into a diffusion tensor for edge enhancing [66, 73, 74]. Let *I(X)* denotes a 2D image, where *X* = (x, y) is the coordinate vector. The structure tensor defined at a coordinate in the image *I* is symmetric positive 2 × 2 tensor given by [71, 73, 74]:

$$J(\nabla I) = K_j * (\nabla I \cdot \nabla I^T) \qquad Eq.5.1$$

where ∇I is the image gradient, and K_j is the Gaussian kernel with standard deviation *j*, and * is the convolution operator. The local image features are obtained by eigen-analysis of the structure tensor:

$$J(\nabla I) = [v_1 \ v_2] \cdot \begin{bmatrix} \mu_1 & 0 \\ 0 & \mu_2 \end{bmatrix} \cdot \begin{bmatrix} v_1^T \\ v_2^T \end{bmatrix} \qquad Eq.5.2$$

where v_1, v_2 are the eigenvectors that give the local image orientations with $v_1=[v_{11}, v_{12}]^T$ and $v_2=[v_{12}, v_{22}]^T$, and the eigenvalues $\mu_1 \geq \mu_2$ give the average contrast in these directions. This structure tensor is transformed into the diffusion tensor equation is described by [66, 67, 71, 73, 74]:

$$\frac{\partial u}{\partial t} = \nabla \cdot (D \nabla u) \qquad Eq.5.3$$

where the result $\partial u/\partial t$ is the rate of change in intensity value in image $u(u = u(t, x, y))$at diffusion time t and pixel coordinates (x, y). ∇. Is the divergence operator, ∇u is the gradient of the image u, and D is the diffusion tensor that uses the same eigenvectors orientations as given by the structure tensor (note the symmetry):

$$D = \begin{bmatrix} D_{11} & D_{12} \\ D_{12} & D_{22} \end{bmatrix} with\ D_{ij} = \sum_{n=1..2} \lambda_n v_{ni} v_{nj} \qquad Eq.5.4$$

The eigenvalues λ_1, λ_2 are calculated via:

$$\lambda_1 = c_1 \qquad Eq.5.5$$

$$\lambda_2 = \begin{cases} c_1 & if\ \mu_1 = \mu_2 \\ c_1 + (1 - c_1) exp\left(\frac{-c_2}{(\mu_1 - \mu_2)^2}\right) & else \end{cases} \qquad Eq.5.6$$

where $c_1 \in (0, 1)$ is a global smoothing constant, and $c_2 > 0$ is the edge enhancing smoothing constant. The described edge enhancing diffusion filtering is repeated in an iterative way. The amount of smoothing is determined by the number of iterations, which is set by the user.

The tensor diffusion Eq.5.3 can be solved numerically using finite differences [39, 73, 74]. The common way to discretise $\partial u/\partial t$ is to use a forward difference approximation. The resulting so-called explicit scheme has the basic structure that is shown in Eq.5.7. This scheme allows calculating all values at a new time level k directly from the ones in the previous level without solving a nonlinear system of equations as shown in Eq.5.8.

$$\frac{u_{i,j}^{k+1} - u_{i,j}^{k}}{\tau} = A_{i,j}^{k} * u_{i,j}^{k} \qquad Eq.5.7$$

$$u_{i,j}^{k+1} = \left(I + \tau A_{i,j}^{k}\right) * u_{i,j}^{k} \qquad Eq.5.8$$

where τ is the time step size and $u_{i.j}^{k}$ indicates the approximation of $\mathrm{u}(\mathrm{x}, \mathrm{t})$ in the pixel (i, j) at time $k\tau$. The expression $A_{i,j}^{k} * u_{i,j}^{k}$ represents a discretisation of the diffusion tensor equation that was described in Eq.5.3. For $A_{i.j}^{k}$ which is also called a stencil and gives the diffusion updates, there are two common discretisations which are called the standard and non-negative discretisation, and which use a 3×3 stencil. These schemes were introduced for simplicity or stability reasons, with no attention paid to optimising their directional behaviour. In order to address this problem, an optimised rotation invariant 5×5 stencil was introduced by Weickert and Scharr [74] where the smoothing values [1,2,1] of the commonly used Sobel kernel were changed to [3,10,3] which gives more rotation invariant derivatives [73, 74]. The research work of [73, 74] showed blurring artefacts in the images especially at the finer structures when applying the standard and non-negative schemes, while the rotation invariant anisotropic diffusion of a 5×5 line filtering scheme was the most suitable scheme for curved structures. For that reason, the CED with the rotation scheme was applied to Fusarium hyphae that have the curved line-like structures. The parameters have been chosen empirically: diffusion time=5, diffusion time step size=1, σ=1.5. These values contribute to filtering more noise without losing the structure of hyphae. The result of applying the coherence filtering to the enhanced image that appears in Figure 5.1, D1-D3 is shown in Figure 5.2, A1-A3.

5.3.3 Morphological operations and binarisation

The goal of this phase is to identify the hyphae (Fusarium filaments) with least noise and imperfection. The first step was to apply a top-hat transform to the coherence diffusion filtered image to acquire the directional information of the filament structures. The top-hat transform of image I, with greyscale structure element Se, is given by:

$$T(I) = I - I \circ Se \qquad Eq.5.9$$

For removing the filaments structure, a structuring element of length 4 is chosen and to capture all possible filaments with their high reflectivity, seven directions have been included (0°, 30°, 60°, 90°, 120°, 150°, and 180°). The responses of all directions are added together as shown in Figure 5.2, B1-B3. To extract the filaments that are most probably hyphae, the multi-level Otsu thresholding method is used. The pixel intensities of the top-hat filter image were divided to three levels, and it is seen that the hyphae are located in the first two levels, see Figure 5.2, C1-C3. The three-level image is binarised so all pixel intensity values coming within these first two levels are converted to 1 and the third level values are converted to 0 as shown in Figure 5.2, D1-D3. To refine the shape of hyphae and connect very close disconnected segments, a morphological close operation with disk structure element of size 3 has been applied to the binarised image and then the noisy and unwanted regions with an area less than 55 pixels have been removed. By doing this, the most likely Fusarium filaments with least possible noise were kept as shown in Figure 5.2, E1-E3. Figure 5.2, F1-F3 shows the automated trace for detected hyphae which are coloured in red.

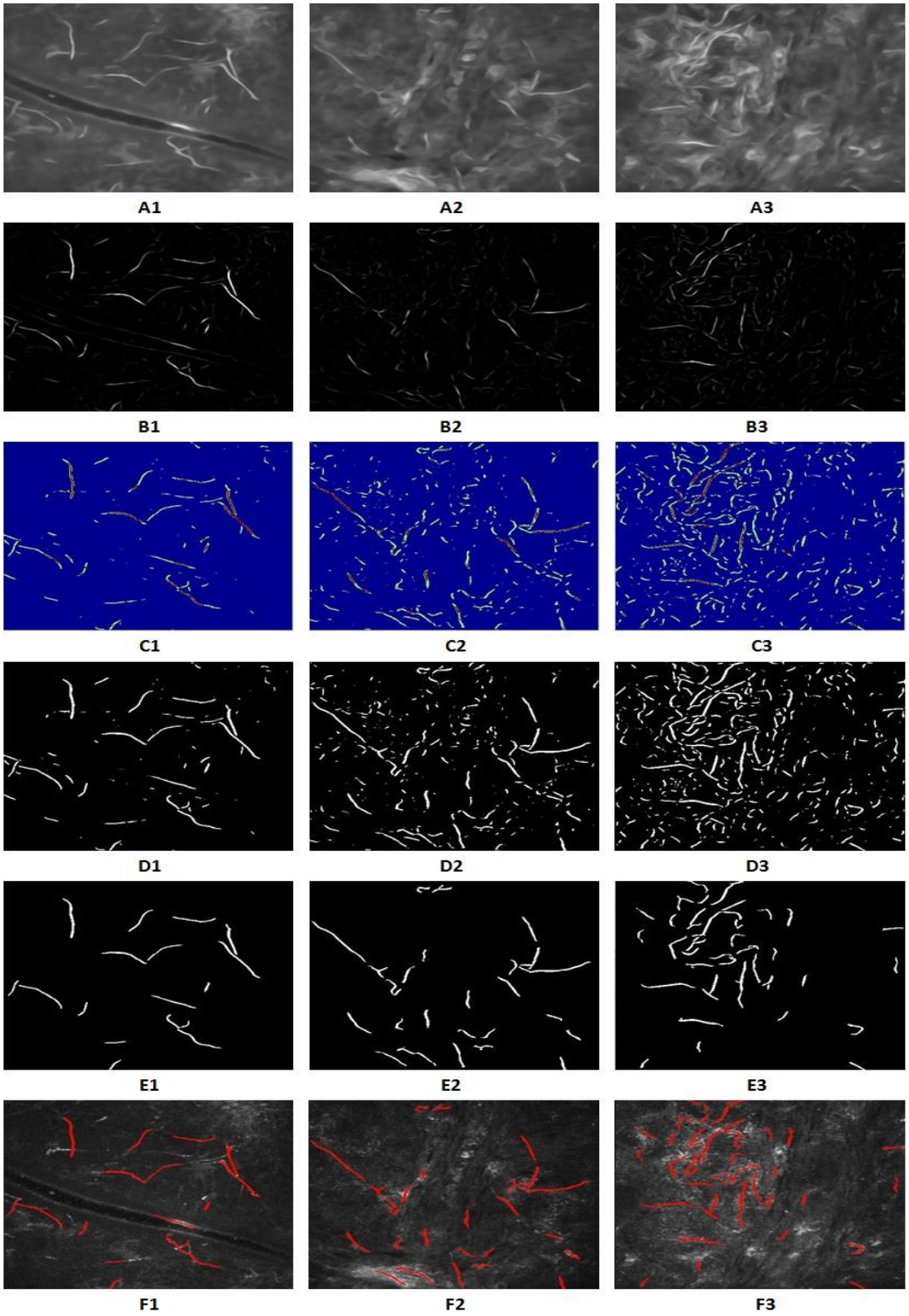

Figure 5.2 Segmentation steps for Fusarium image. A1-A3) Coherence-enhancing diffusion filter output. B1-B3) Top-hat transform output. C1-C3) Division of pixel intensities of the top-hat image into three levels. D1-D3) Binarisation of images in (C1-C3) where all pixel intensity values coming within these first two levels are converted to 1 and the third level values are converted to 0. E1-E3) The detected Fusarium hyphae after removing unwanted information. F) Colouring the detected hyphae in red on the original images that appear in Figure 5.1, A1-A3.

5.3.4 Detection of high reflective canal

Some of the images in the dataset showing a relatively high reflective and long linear structure with a canal shape which is partially detected by the hyphae segmentation algorithm, and which consists of two very long lines running alongside each other. Dr Jaya Chidambaram (Ophthalmologist at Manchester Royal Eye Hospital, U.K.) stated that this canal may not represent fungal hyphae and its appearance may represent an anatomical feature in the cornea (e.g. collagen lamellae or corneal fold).

As the algorithm proposed to detect Fusarium hyphae was not able to detect the whole canal where it has low reflective parts compared to the hyphae (see Figure 5.3, A1-A3), another algorithm to detect the canal wherever it appears was implemented.

The algorithm starts with the coherence diffusion filtered image which appears in Figure 5.3, B1-B3. This image is smoothed using a Gaussian filter with σ equal to 2 as shown in Figure 5.3, C1-C3. The same top-hat filter which was discussed in section 5.3.3 is applied to the Gaussian filtered image to get the image content structures shown in Figure 5.3, D1-D3.

To extract those structures, a hysteresis thresholding is used. This thresholding method is performed for edge detection using two thresholds. Very low thresholds were used to get as most as possible of the canal and the values 0.023 and 0.011 were effective for the images of the dataset. This leads to the creation of 3 classes; below the low threshold of 0.011 (to be removed), above the high threshold of 0.023 (to be retained), and between these thresholds (to be retained only if connected to an edge above the high threshold) and it also helps in edge linking.

The result of the thresholding step is shown in Figure 5.3, E1-E3. Areas of less than 680 pixels (the value is determined empirically), containing noisy and unwanted information, are removed as shown in Figure 5.3, F1-F3. After that, the characteristic of two very long lines running alongside each other has been used to detect only the canal as some segments remain beside the canal (if it exists).

As shown in Figure 5.3, F1-F3, the segment which is not one of the canal lines is not thin which means it has a big minor axis length in comparison to canal lines. The minor axis length returns a scalar that specifies the length (in pixels) of the minor axis of the ellipse that has the same normalised second central moments as the region and it is computed using the 'MinorAxisLength' of the 'regionprops' MATLAB function.

By examining the images of Fusarium in the dataset, it has been found that the canal line has a minor axis length value which is less than 47. The result of final automated detected canal is shown in Figure 5.3, G1-G3.

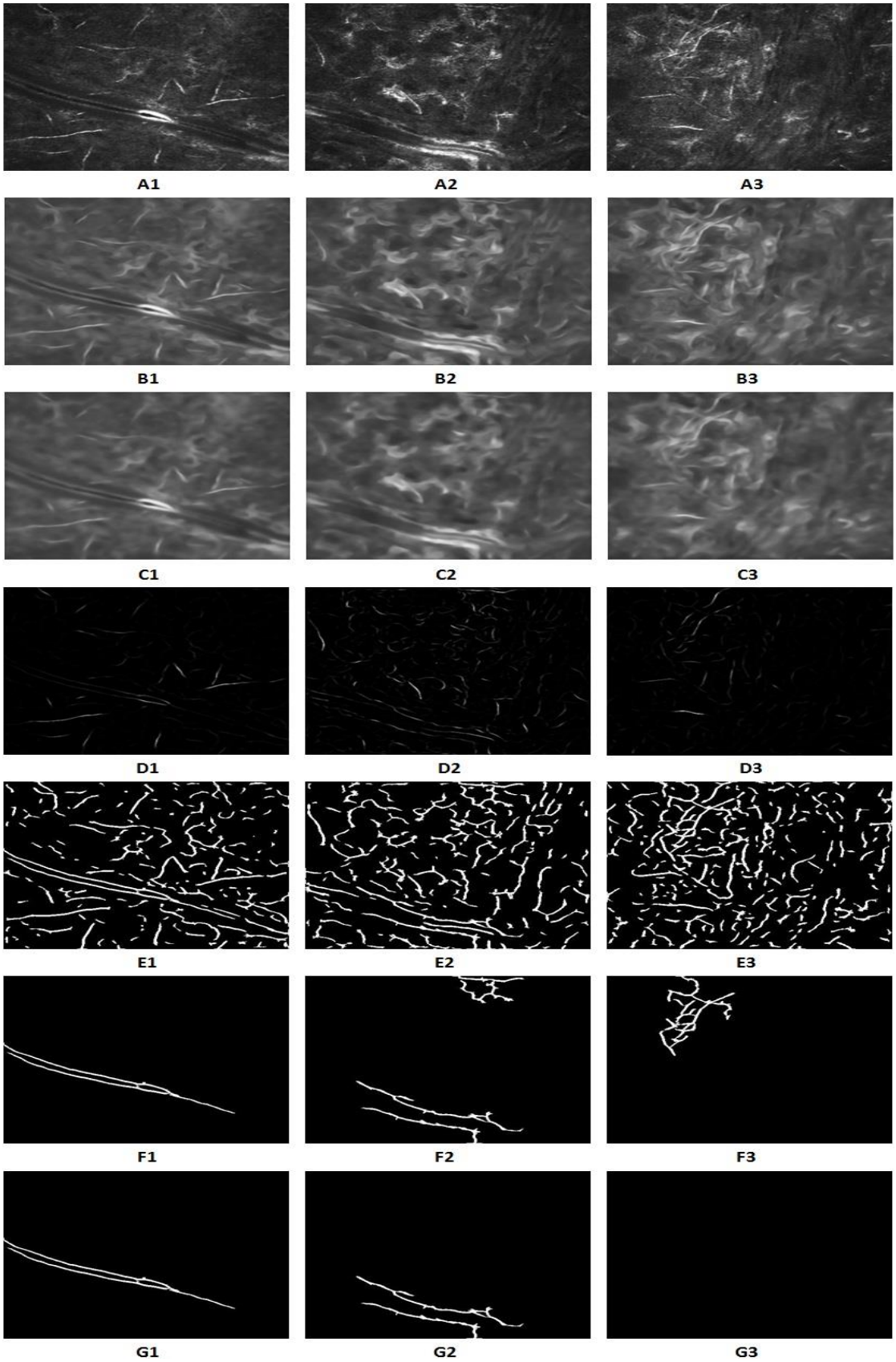

Figure 5.3 The steps of detecting the reflective canal. A1-A3) Input images from the dataset. B1-B3) Coherence-enhancing diffusion filter output. C1-C3) Gaussian filtered output. D1-D3) Top-hat transform output. E1-E3) Hysteresis thresholding output. F1-F3) The segments that remain after removing unwanted information. G1-G3) The canal is only detected (if it exists).

5.4. Results discussion and evaluation

The Fusarium image enhancement and segmentation procedure is summarised in Figure 5.4.

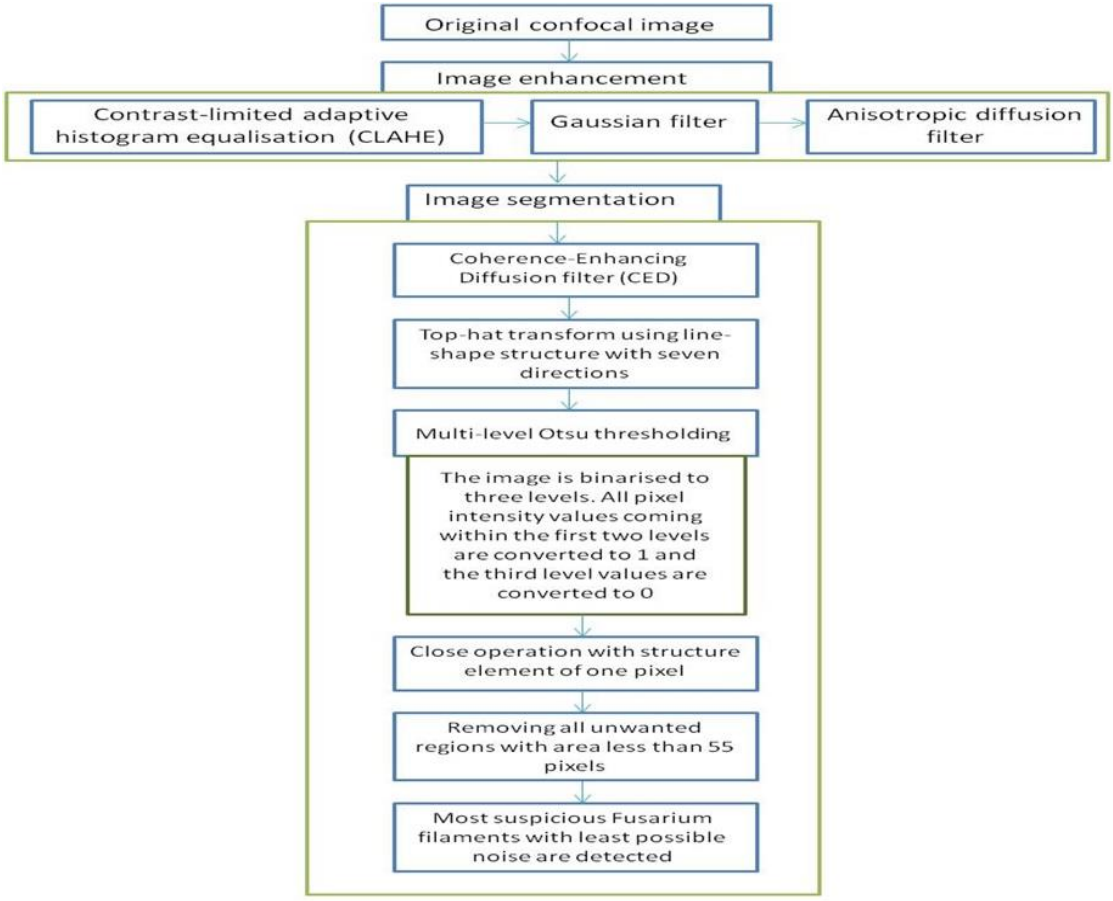

Figure 5.4 The proposed algorithm of Fusarium image enhancement and segmentation.

This process was applied to the dataset which contains 22 images from one patient has Fusarium keratitis. The dataset of Fusarium keratitis images was sent to Dr Chidambaram and she traced manually the most suspicious filaments that are most likely to be Fusarium hyphae. Figure 5.5 shows the hyphae that were detected by the proposed system in comparison to those that were traced by the ophthalmologist (the rest of images appear in Appendix B).

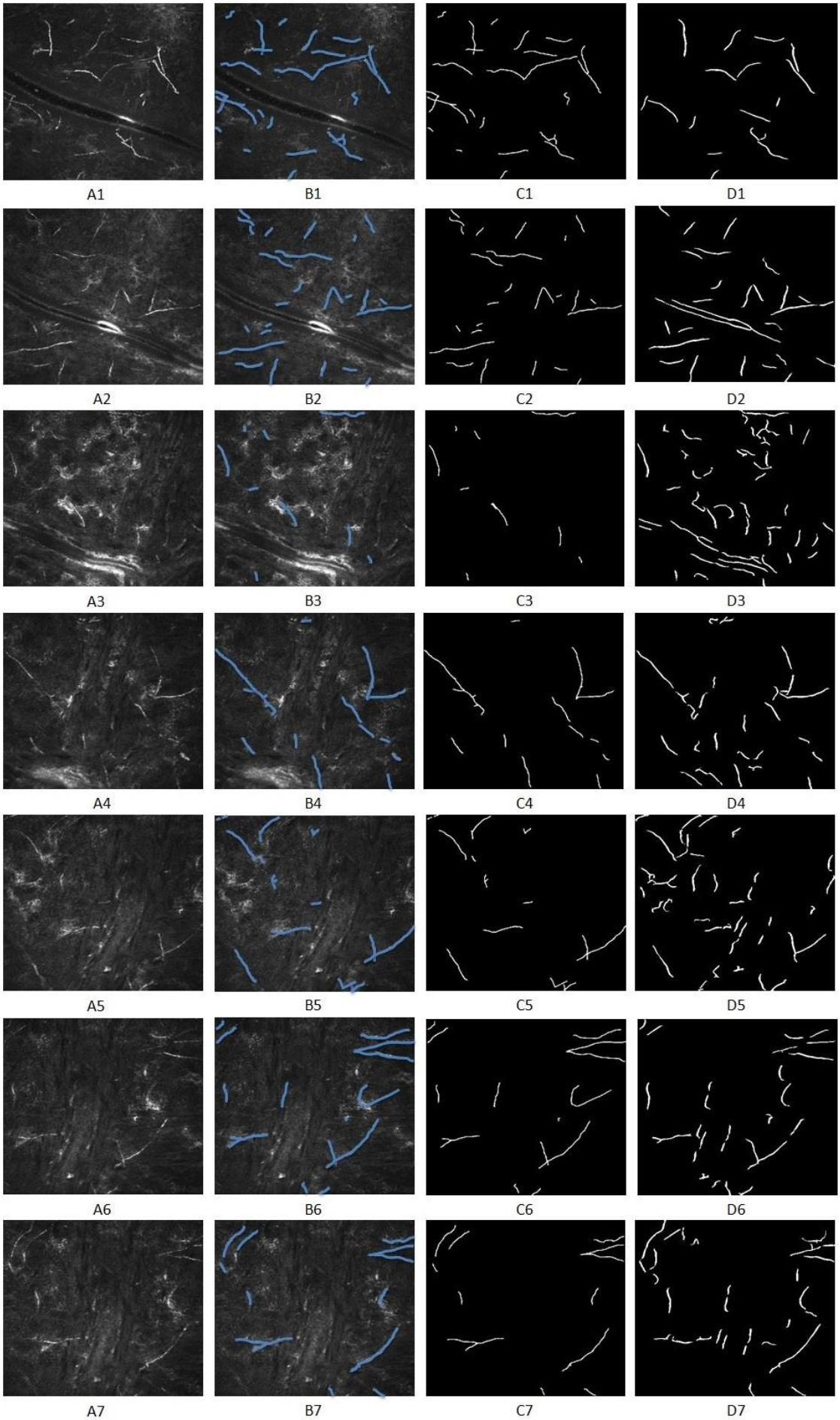
A1
B1
C1
D1
A2
B2
C2
D2
A3
B3
C3
D3
A4
B4
C4
D4
A5
B5
C5
D5
A6
B6
C6
D6
A7
B7
C7
D7

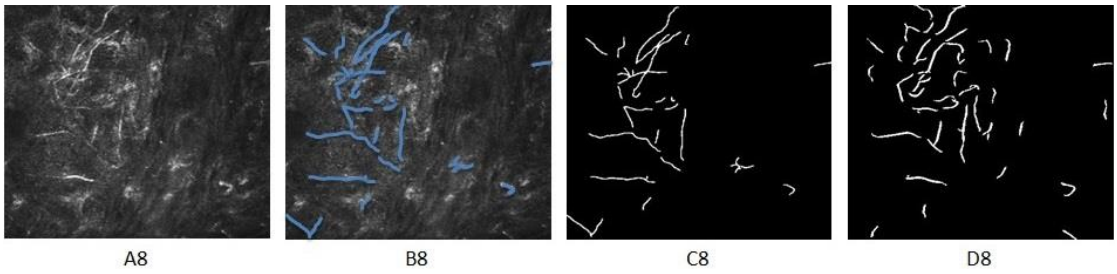

Figure 5.5 Sample of 8 images from the dataset to evaluate the performance of the proposed segmentation process of Fusarium hyphae. A1-A8) Input images. B1-B8) The manually traced hyphae. C1-C8) Binarisation of the manual traced hyphae. D1-D8) Binarisation of the automated traced hyphae.

It is seen that most of the traced hyphae are detected by the proposed system. However, we can also see some challenges with the automated system which are summarised in the following points:

1- The appearance of false-positive hyphae (separate, or part of the true ones). The feedback received from the clinician indicated that these parts are most likely to be stromal keratocytes. These keratocytes appear as high reflective granules and broad bands that are cellular processes that take on a linear shape or appear adjacent to the hyphae and so the proposed procedure detects them as fungal filaments. This problem appears clearly in Figure 5.5, D3.

2- The discontinuities that occur in some detected hyphae. This problem refers to hypo-reflectivity of some hyphal parts. This means, instead of detecting a single long hypha as observed with the manual tracing of hyphae, the programme detects many segments (two or three or more) of the hyphae and naturally this adversely affects the total number of detected hyphae (see Figure 5.5, D6). Hypo-reflectivity could cause another problem other than discontinuity; i.e. losing part(s) of the hypha (see Figure 5.5, D1).

For discontinuities and hypo-reflectivity, it is important to mention that the confocal scan is used in conjunction with clinical knowledge, i.e. whether the patient history and examination fits, and the corneal sample grows fungi [19, 75]. Consequently, it is hard to reach an exact segmentation or to say that such a segmentation algorithm is the best using only confocal images. Furthermore, it is important to know that clinicians do not make a diagnosis or decision using one image; they deal with a sequence of images that is taken for one eye at different depths in the cornea. For that reason, there is a need to align those images on top of each other so they are registered. This is very helpful in diagnosing fungal keratitis where the same filament is viewed at least 2 µm deeper in the adjacent confocal image and therefore it may have better reflectivity and maybe improved resolution. Eye movement during the acquisition process, which mostly happens due to respiration and cardiac pulse, causes misalignment and shifts in the x-y plane of captured images as mentioned in section 4.1. Therefore, the need for image registration process arises. The registration of a sequence of images for an infected eye helps to address the problem of discontinuity and hypo-reflectivity to a large extent. However, because of the lack of an available Fusarium dataset, the registration of Fusarium images will be a future research work.

3- Overlapping detected hyphae. This affects the count of hyphae where the connected parts are counted as one segment. Thus it affects the length of hypha where the length will be computed for the segment as one hypha but in reality could be many overlapping hyphae (see Figure 5.5, D8).

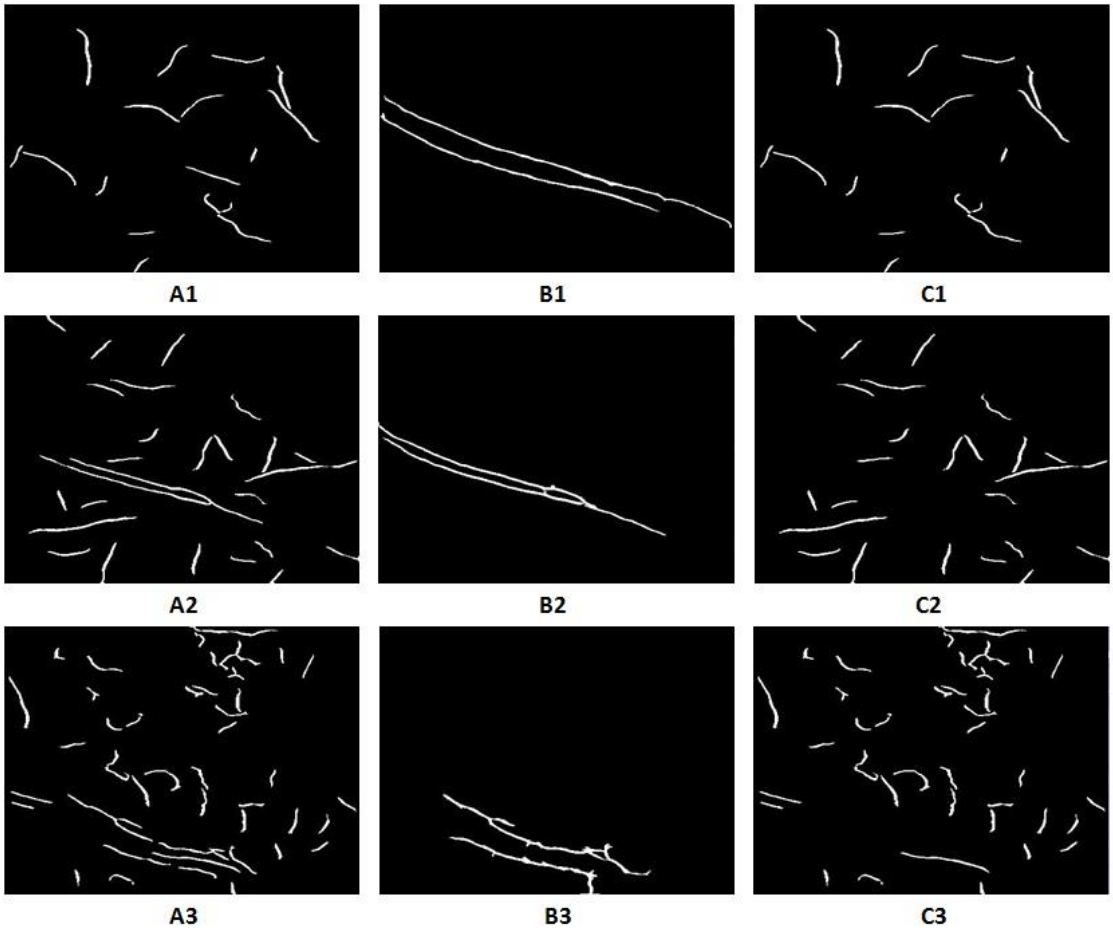

Figure 5.6 The removal of canal structure from the segmented image. A1-A3) Automated detected hyphae using the proposed segmentation algorithm with the appearance of canal structure, fully or partially. B1-B3) Automated detection of the canal structure. C1-C3) The result after removing the canal structure parts which are falsely detected in the images A1-A3.

4- The appearance of high reflective canals. As mentioned in section 5.3.4, some images include a highly reflective long linear structure with a canal shape, which is detected fully or partially as hyphae by the system as shown in Figure 5.5, D1, D2, and D3. The segmentation outcome was improved by using the results of the detected canal (as explained in section 5.3.4) to subtract it from the falsely detected image (see Figure 5.6).

The proposed segmentation process of hyphae was evaluated as well by comparing the result of this work with the result of Qiu's work which mentioned

in Section 2.3. Figure 5.7 shows an input image from the study by Qiu et al. and the difference between their detection result and the one from this research is clear. In their result, many hyphae are missed out, most hyphae still have gaps, and the result is very noisy. Unwanted background regions are connected to the hyphae intensively and other parts appear as accumulated particles (not filaments) and are still kept in the segmented image. Moreover, the result obtained from the method proposed in this research can be improved more. It is seen that the hyphae of their dataset are mostly long and overlapping, so if cut-off value is set for the minimum area or length then the detected filaments which are most probably not related to fungal hyphae will be removed, as shown in Figure 5.7D.

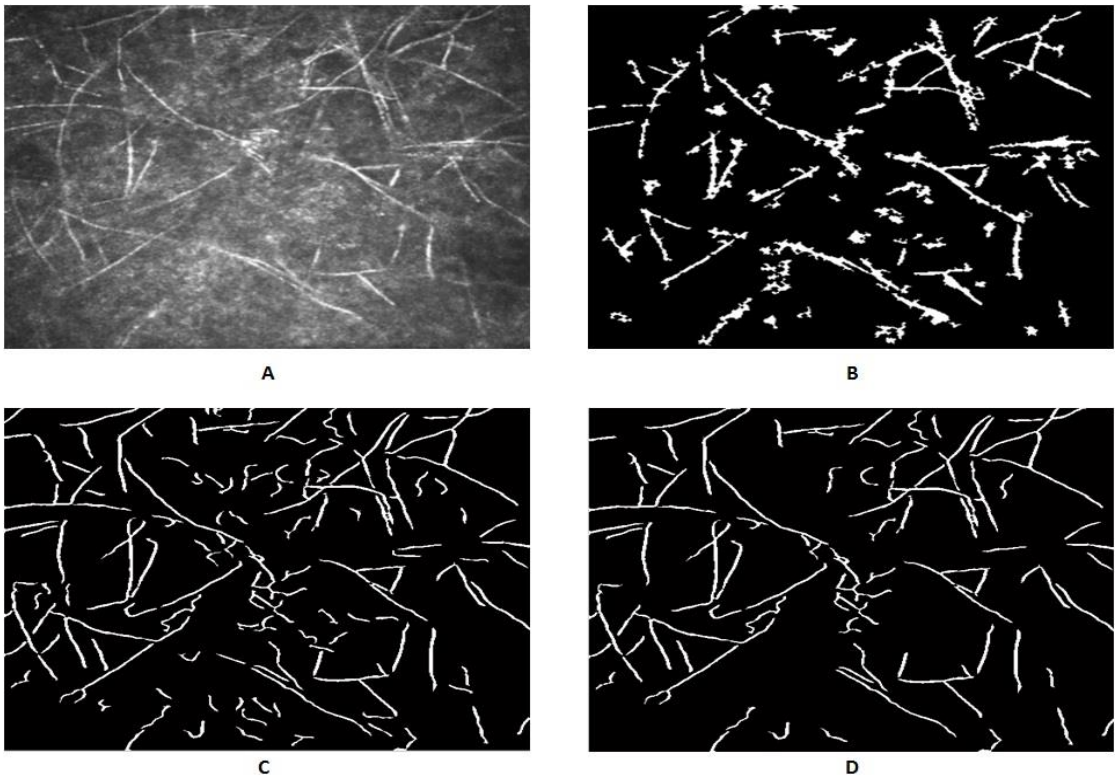

Figure 5.7 Comparison between the result of segmentation of this research and the study of Qiu et al. [41]. A) The original image of fungal keratitis from the dataset of Qiu et al. B) The result of Qiu's method. C) The result of applying this research proposed method. D) Improving the result in (C) by removing small areas using specific cut-off value as the filaments are long and overlapped.

5.5. Parameters for quantitative analysis of Fusarium hyphae

Clinicians and fungal biologists believe that there are several measurements that could be useful in diagnosing fungal keratitis or in measuring changes before and after treatment [76]. As a result, this may help clinicians in assessing the corneal response to therapy.

The standard measurements of fungal hyphae based on fungal biologists [76] and computed for the image results from the segmentation process are:

1. **Total Hyphal Volume**: the total number of white pixels from all hyphae within the image size. When the hyphae are skeletonised then the total hyphal volume is equal to total hyphal length.
2. **Total Hyphae Volume Density**: the total number of white pixels from all hyphae divided by the image size in pixels.
3. **Hyphal Growth Unit**: the total length of all hyphae in the image (Total Hyphal Volume) divided by the number of hyphal tips within the image (count of hyphae).
4. **Max Length**: the maximum length of the lengths of all hyphae.
5. **Min Length**: the minimum length of the lengths of all hyphae.
6. **Fungal Branching Angle**: the angle in degrees of hyphal branches.

Table 5.1 shows the main values of measurements that have been computed by the system for manual and automated traced images that are shown in Figure 5.5. All of those measures have been computed after converting the binarised image to its skeletonised version using the 'skel'

morphological operation in MATLAB. This means the hyphae are represented as one pixel in width and consequently the computation of the above measures becomes reliable.

Knowledge of hyphal length may make a difference, as the length may change before and after treatment. The clinician mentioned that therapy could be one possible reason for hyphae breaking up. So if the length of hyphae becomes smaller after treatment, this may help clinician to understand whether the patient is responding well to the treatment.

Manual traced					
Figure 5.5	**Total Hyphae Volume**	**Total Hyphae Volume Density**	**Hyphal Growth Unit**	**Max Length**	**Min Length**
C1	1460	1.0005	76.8421	232	15
C2	1246	0.8539	49.84	154	14
C3	405	0.2775	45	106	14
C4	855	0.5859	77.7273	247	20
C5	788	0.54	60.6154	195	12
C6	1134	0.7771	94.5	276	14
C7	872	0.5976	79.2727	185	20
C8	1475	1.0108	77.6316	488	13
Automated traced					
Figure 5.5	**Total Hyphae Volume**	**Total Hyphae Volume Density**	**Hyphal Growth Unit**	**Max Length**	**Min Length**
C1, Figure 5.6	749	0.5133	49.9333	81	21
C2, Figure 5.6	1087	0.7449	43.48	117	24
C3, Figure 5.6	1344	0.921	37.3333	98	18
D4	1011	0.6928	43.9565	95	23
D5	1352	0.9265	42.25	134	20
D6	941	0.6449	47.05	139	20
D7	1154	0.7908	42.7407	132	20
D8	1460	1.0005	42.9412	102	19

Table 5.1 The values of measurements that have been computed for manual and automated traced images.

The accuracy of the computed measurements can be quantified by calculating the percent error which is a measure of the agreement of a particular measurement with the true (or accepted) value of the parameter. The formula for percent error is [77]:

$$\%Error = \frac{|x_T - x_E|}{x_T} \times 100\% \qquad Eq.5.10$$

where x_T and x_E are true and experimental values, respectively.

True values represent values computed for the manual traced images, while experimental values represent values computed for the automated traced images. Percent error rates which obtained for the standard measurements of fungal hyphae were as following: Total Hyphal Volume=48%, Total Hyphae Volume Density=48%, Hyphal Growth Unit=23%, Max Length=33%, and Min Length=49%.

The percent error rate is relatively considered high and this happened because of the challenges that have been mentioned in Section 5.4. However, the researcher supposes these values may be more useful when comparing automated traced images for the same patient before and after therapy with the same segmentation procedure used in both cases.

The automated detection of hyphal branches is a big challenge mainly because of the overlapping of fungal filaments which gives a false impression of branching and in image processing any intersection point is considered a branch point. The result was improved and the number of false branches was significantly reduced after a deep observation of the images of the dataset, i.e., after skeletonisation of the binary images of the detected hyphae and then after applying the algorithm to detect branch points (using the 'branchpoints' morphological operation in MATLAB). It has been noticed that most of the overlapping hyphae have more than one intersection point while in most cases of real branches there is just one pixel that represents the intersection point. Then the angle of the branch is computed using the 'Orientation' region property

in MATLAB. The branch angle of filaments is considered a useful measurement to distinguish between different fungal species as reported in the literature [18]. For example, Fusarium filaments have a hyphal branching angle of 90° in IVCM while the branching angle in the infected cornea of Aspergillus fumigatus was measured as 45°. Recently, Chidambaram et al. [19] found that the branch angle of hyphae in IVCM images cannot be used to distinguish Fusarium from Aspergillus spp as there was no significant difference in the branching angle between the two species. However, branch angles may change following anti-fungal treatment, and therefore an automated system that is able to detect this in IVCM images may help the clinician to do further research in this field in an objective and rapid way. Figure 5.8 shows the suspicious branches marked by the Ophthalmologist in a sample of manually traced images while Figure 5.9 shows the automated detected branches and their angles for the same sample.

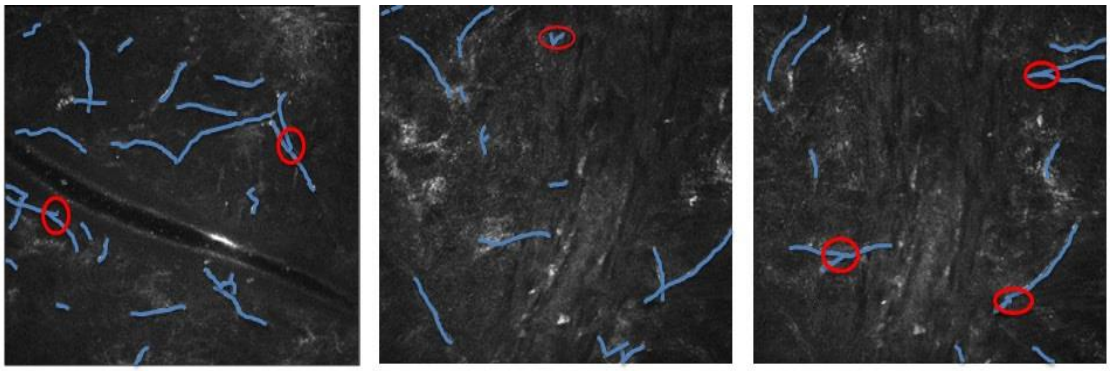

Figure 5.8 Sample of manually traced images with suspicious branches marked by the Ophthalmologist.

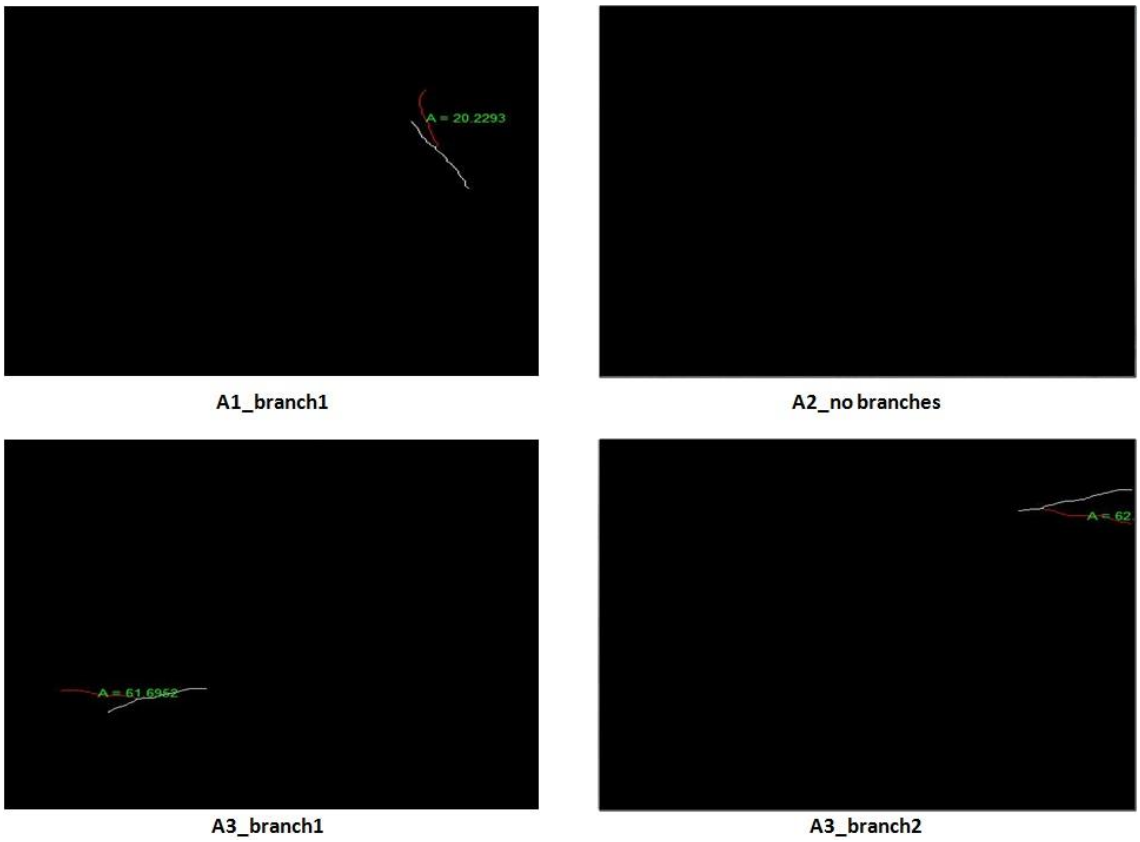

Figure 5.9 The automated detected branches for the images appear in Figure 5.8 and their angles degrees. In each image, one branch was missed out.

It is important to mention here that even though the proposed algorithm tried to eliminate the false branches especially those produced because of overlapping, it is still possible to detect branches which are overlapping hyphae and not real branches in the original images. This happens because hyphae have been connected in the result of the segmentation, thus the number of detected branches depends on the accuracy of segmentation process.

5.6. Conclusion

Fusarium confocal images suffer mostly from blur and the appearance of unwanted information which could result from mechanical contact with the cornea, motion of the cornea, light reflection, or from the existence of stromal keratocytes or other anatomical features in the cornea. To improve the visibility

of the filaments and to reduce the artefacts, Fusarium image processing starts with image enhancement using the CLAHE technique, a Gaussian filter, and then the Anisotropic Diffusion Filter.

The detection of Fusarium hyphae is achieved by first using a coherence-enhancing diffusion filter, which makes many interrupted filaments get closer and preserves the filaments' shape features with less noise. Secondly, to extract the filaments in order to deal with them later, a top-hat transform with line-shaped structure is used. The image is then binarised using a three-level Otsu thresholding method and the interesting regions are located in the first two levels. The result is refined using morphological operations to close and remove small areas. The useful quantitative parameters of detected hyphae are then measured to be used in the evaluation of the patient's condition.

The automated procedure of detection Fusarium hyphae faces many challenges such as discontinuities and overlapping which affect the accuracy of hyphal segmentation and therefore the following computation of measurements. The accuracy of the measurements values was quantified by calculating the percent error rate for each measurement and which ranged from 23% to 49%.

As fungal biologists and clinicians believe that in vivo confocal microscopy can help them to firstly make the diagnosis for fungal infection, and also indicate how the fungi behave long-term if they repeat imaging after treatment, the automated rapid processing for the confocal images including the computation of measurements for the detected filaments would be very useful in therapy.

6. Conclusions and Suggestions for Future Work

6.1. Overview

The cornea is the eye's outermost layer. Transparency and avascularity make the cornea a very special tissue with a thickness of approximately 520 μm at the centre to about 650 μm at the periphery, divided into three main layers separated by two thin membranes. The epithelium is the outermost layer separated from the central stromal layer by Bowman's membrane. Descemet's membrane separates the stromal layer from the innermost endothelial layer. Each layer and membrane has its featured histological structure.

Confocal microscopy is a powerful diagnostic technique that allows non-invasive, repeated, rapid, in vivo cellular and high-resolution imaging of all layers of the cornea, providing direct visualization of pathogens within the patient's cornea, enabling the clinical investigation of numerous corneal diseases and new discoveries of corneal pathology at the cellular level. In vivo confocal microscopy is helpful in evaluating the morphological characteristics of corneal abnormalities at the histological level and may be helpful in diagnosis, determination of progression, and the efficiency of the treatment.

Infectious keratitis can lead to irreversible complications, significant visual loss, and even loss of the eye. The value of IVCM method has been demonstrated in the diagnosis and management of Acanthamoeba and fungal keratitis through which fungal filaments (hyphae) and Acanthamoeba cysts can be immediately detected in the patient's cornea, allowing clinicians to promptly start the correct antimicrobial therapy.

The existence of automated visual signature detection and analysis for HRT confocal images of Acanthamoeba keratitis and fungal keratitis can be valuable to ophthalmologists as it makes the process of the diagnosis faster, more accurate, and more objective. The automated analysis of the quantitative parameters for Acanthamoeba cysts and fungal filaments can help in studying the correlation of quantitative evaluation of these cysts and filaments with clinical staging of disease. It also assists clinician in determining whether the ulcer is improving, or whether a change of treatment is needed.

This research work detects Acanthamoeba cysts and Fusarium hyphae and analyses them through many stages; image enhancement to improve the quality of the image and to eliminate unwanted information, and image segmentation to isolate the visual signatures of the disease from the background. The most useful measurements for cysts and hyphae that help in diagnosing the disease, in assessing the treatment, and in discovering the stages of the disease are then computed. The cysts and hyphae detected are coloured in images to draw the attention of clinicians to the affected regions. In Acanthamoeba images of the dataset where the cysts were traced manually and automatically, the positive predictive values rate of cysts was 76%. In Fusarium images, many standard measurements of hyphae were computed. The accuracy of their values was quantified by calculating the percent error rate for each measurement and which ranged from 23% to 49%.

For Acanthamoeba images, the ordered sequence of images, as each corneal scan produces many images along the whole cornea, are registered to get the depth of the infection and to prepare the 2D sequence of images of each patient for the 3D building model. The lack of images in the Fusarium dataset in

this research moves registration a step further into the future. The accuracy of the system was mainly evaluated by comparing automated detection with manual marking. The results were very accurate as they were very close to the detection done by a human. The challenges and limitations that affect the accuracy of segmentation were rationally justified. Many useful clinical quantitative parameters for the cysts and hyphae detected by the system were analysed, which can give ophthalmologists an idea of how the cyst or fungi behave long-term if imaging were repeated after treatment and these parameters were used as well in the accuracy evaluation of segmentation.

6.2. Highlights and contributions

The outcome of this research and the main contributions presented in this thesis are summarised as follows:

1. Acanthamoeba keratitis HRT confocal images are very noisy; they are blurry, hazy, and have unwanted information such as epithelial cells. An effective enhancement technique was proposed using a dark channel prior scheme which was used by He et al. [49] to retrieve the original scene (free-haze) from hazy, outdoor, and coloured camera images. The scheme has been normalised and adapted to develop an enhancement method that was able to generate a very clean image with most of the cysts and a least of unwanted information.
2. An efficient segmentation technique for Acanthamoeba cysts was suggested and it was divided into two steps; one for normal sized cysts and the other for massive cysts. Level by level new binarisation technique using the histogram of the enhanced image was proposed to detect the normal sized cyst, while the massive cysts were detected by applying a binarisation

using a specific threshold value that is able to show the border of the massive cysts and then morphological operations were used to complete the process of cyst detection.

3. A refinement step using the local standard deviation has been proposed. It was able to keep from the detected cysts the most possible to be cysts and to avoid the regions that would be detected as cysts while they are epithelial cells when applying the algorithm to normal epithelial confocal images.
4. A registration step using SIFT technique was adopted to align the Acanthamoeba ordered sequence of images, which is one of the main requirements to develop 3D modelling. The SIFT algorithm has been normalised to work effectively with the dataset of this research.
5. A tracking methodology for Acanthamoeba cysts was suggested to know the depth of each detected cyst in the whole sequence of images for each subject, which means to follow up the cysts in a z-direction. The estimated geometric transform that was computed in the registration step was used and applied to the segmented images to keep the process of cyst tracking in the sequence of images. At the end, each cyst has the same tracking number from the first original image in which it appears until the last original image where it can be seen. This process facilitates following up cysts in an identical location in order to perform more efficient treatment evaluation but the challenge here is still to design systems that can accurately perform serial scans in an identical location on the cornea.
6. The system provides an automatic quantitative analysis of the tracked cysts which could be clinically helpful in the follow-up and treatment assessment. Furthermore, the parameters' values of the quantitative analysis could contribute in the distinction between Acanthamoeba in its active and its

dormant phase. The remaining challenge here is to design an in vivo microscopy system that can pick up Acanthamoeba in their active form. These quantitative values could be used as well to distinguish between Acanthamoeba cysts and any other confusing structures such as stromal keratocytes and epithelial cells, but the clinical studies that are dedicated to cover this issue are still not available.

7. Fungal keratitis HRT confocal images are very noisy; they are blurry and have unwanted information such as stromal keratocytes. An effective enhancement technique was used to improve the quality of Fusarium images and to be prepared then for the segmentation process.
8. An efficient segmentation technique for Fusarium hyphae was suggested. This technique contributes to getting results with most number of hyphae, least number of unwanted segments, and least number of disconnected Fusarium hyphae.
9. The system provides an automatic quantitative analysis of the traced hyphae which could be clinically helpful in the follow-up and treatment assessment. Furthermore, it could be a good indicator for the hyphae's behaviour.
10. The developed diagnostic system is fully automated and is implemented with friendly GUI (see Appendix C).
11. The developed system could be applied to other biological systems that exhibit a similar behaviour. For example, the researcher has noticed that mammograms show abnormal structures (masses, and microcalcifications) that look like Acanthamoeba cysts. This idea could be investigated as future work for the author.

6.3. Challenges and Limitations

The main challenge faced in this work was the lack of available datasets to work on. Most clinical studies or reports of Acanthamoeba and Fusarium show few images in their evaluation and discussion. Moreover, the contact with other ophthalmologists to get more datasets was not successful. Thus, the research relies relatively on small datasets especially for Fusarium which was obtained from Manchester Royal Eye Hospital. This challenge limits further work with Fusarium, as there were not enough fungal images to do registration which may help in improving the process of segmentation. If the same filament could be viewed at least 2µm deeper in the adjacent confocal image, it might have better reflectivity and thus improve the overall resolution.

The lack of benchmarks in the literature to compare with is another challenge. This work depends only on samples from the datasets that were manually marked by the clinicians who were involved in this research. However, this could be considered a strong point of this research as it delivers a fully automated system dealing with infectious keratitis confocal images which aims to detect Acanthamoeba cysts and Fusarium hyphae and quantitatively analyses them. Therefore it would be a base for any future research in the same field.

Technically, the main limitation of segmentation process for cysts in Acanthamoeba keratitis images is the inability to isolate Acanthamoeba cysts from stromal keratocytes nuclei when the infection reaches the stroma. Also, it deals with all cysts as one type without taking into consideration the appearance of double wall cysts in advanced stages of the disease.

The segmentation process for hyphae in Fusarium images faces many challenges which affect the accuracy of hyphae's measurements calculations. The main challenge is overlapping between Fusarium hyphae and therefore the total apparent count of hyphae and the length of each hypha differing from what they are in reality.

6.4. Suggestions for future work

The main suggestions for future work that could improve the developed system and could extend the research are:

1- The appearance of double-wall cysts helps in distinguishing between Acanthamoeba cysts and other confusing structures. The researcher aims to work in this field, but there is a need to get more information about the features of double-wall cysts since there is not enough or any clear description in literature especially in terms of measurable values. Depending on the visual appearance, some measurements, such as the percentage of halo and the percentage of darkness can contribute to identifying the double-wall cyst.

2- In a certain stage of Acanthamoeba keratitis, Acanthamoeba cysts start to appear blurry and connected showing cysts in chains and clusters. This could be an indicator of cyst behaviour and may help as well in distinguishing the cysts from other structures. For that reason, there is a goal to detect this behaviour and then to improve the segmentation scheme to capture the case of connected cysts in clusters.

3- There is a plan to generate 3D models from the sequence of registered images of Acanthamoeba keratitis and Fusarium scans which may help in furthering the process of the disease diagnosis.

4- Because of the lack of time, the researcher was not able to order the sequence of images of the Acanthamoeba patient automatically. The ordering was done manually. Also, there was not enough time to investigate more registration methods especially because SIFT gave very accurate results and was enough to achieve the ultimate goal although it is a bit slow. To avoid human intervention and to make the system faster, there is a need to look for effective ordering techniques and to investigate faster registration methods which have the same efficiency as SIFT.

5- The author believes that the enhancement and segmentation techniques developed in this research for detecting Acanthamoeba cysts that have round shapes could be effective in detecting high reflective round structures on a dark background in grey-scaled images of any application. Therefore, it is recommended to work further on this idea in the future.

6- Because of the lack of an available Fusarium dataset, the registration of Fusarium images is suggested to be work for the future. The registration of a sequence of images for an infected eye helps to address many of low-quality problems of Fusarium images.

7. References

[1] D. Patel, “In vivo confocal microscopy of the cornea in health and disease,” ResearchSpace@ Auckland, 2005.

[2] T. Hillenaar, “In Vivo Confocal Microscopy expanding horizons in corneal imaging,” Ph.D. thesis, Erasmus University Rotterdam, 2012.

[3] D. Smerdon, “Anatomy of the eye and orbit,” *Current Anaesthesia & Critical Care,* vol. 11, no. 6, pp. 286-292, 2000.

[4] "Facts About the Cornea and Corneal Disease," 17 February, 2017; https://nei.nih.gov/health/cornealdisease.

[5] A. Elbita *et al.*, “Preparation of 2D sequences of corneal images for 3D model building,” *Computer methods and programs in biomedicine,* vol. 114, no. 2, pp. 194-205, 2014.

[6] M. S. Sharif *et al.*, “An efficient intelligent analysis system for confocal corneal endothelium images,” *Computer methods and programs in biomedicine,* vol. 122, no. 3, pp. 421-436, 2015.

[7] R. Alzubaidi *et al.*, “In vivo confocal microscopic corneal images in health and disease with an emphasis on extracting features and visual signatures for corneal diseases: a review study,” *British Journal of Ophthalmology*, 2015.

[8] R. L. Niederer, and C. N. J. McGhee, “Clinical in vivo confocal microscopy of the human cornea in health and disease,” *Progress in Retinal and Eye Research,* vol. 29, no. 1, pp. 30-58, 1//, 2010.

[9] N. Lagali *et al.*, *Laser-scanning in vivo confocal microscopy of the cornea: Imaging and analysis methods for preclinical and clinical applications*: INTECH Open Access Publisher, 2013.

[10] F. Scarpa, “Automatyc analysis of confocal images of the cornea,” 2008.

[11] A. Labbé *et al.*, “Contribution of In Vivo Confocal Microscopy to the Diagnosis and Management of Infectious Keratitis,” *The Ocular Surface,* vol. 7, no. 1, pp. 41-52, 1//, 2009.

[12] P. K. Vaddavalli *et al.*, “Role of confocal microscopy in the diagnosis of fungal and acanthamoeba keratitis,” *Ophthalmology,* vol. 118, no. 1, pp. 29-35, 2011.

[13] I. Ekkeshis, *Patient Information – External disease and corneal Acanthamoeba Keratitis [Leaflet]*, Moorfields Eye Hospital NHS, 2015.

[14] Q. Liang, X. Sun, and A. Labbe, “Role of in vivo confocal microscopy in the management of infectious keratitis,” *[Zhonghua yan ke za zhi] Chinese journal of ophthalmology,* vol. 49, no. 10, pp. 951-955, 2013.

[15] A. M. Imam, “Blindness due to Acanthamoeba: first case report from Sudan,” *International journal of health sciences,* vol. 2, no. 2, 2010.

[16] W. Shi *et al.*, “Antifungal chemotherapy for fungal keratitis guided by in vivo confocal microscopy,” *Graefe's Archive for Clinical and Experimental Ophthalmology,* vol. 246, no. 4, pp. 581-586, 2008/04/01, 2008.

[17] L. Wang *et al.*, “In vivo confocal microscopic characteristics of fungal keratitis,” *Life Science Journal,* vol. 5, no. 1, 2008.

[18] E. Brasnu *et al.*, "In vivo confocal microscopy in fungal keratitis," *Br J Ophthalmol*, 5, pp. 588-91, England, 2007.

[19] J. D. Chidambaram *et al.*, “In vivo confocal microscopy appearance of Fusarium and Aspergillus species in fungal keratitis,” *British Journal of Ophthalmology*, pp. bjophthalmol-2016-309656, 2017.

[20] E. C. Alfonso *et al.*, “Insurgence of Fusarium keratitis associated with contact lens wear,” *Arch Ophthalmol,* vol. 124, no. 7, pp. 941-947, 2006.

[21] B. Clarke *et al.*, “Advances in the diagnosis and treatment of Acanthamoeba keratitis,” *Journal of ophthalmology,* vol. 2012, 2012.
[22] L. L. Cheng *et al.*, “Review of Acanthamoeba keratitis associated with contact lenses in Hong Kong Chinese people,” *Hong Kong Journal of Ophthalmology,* vol. 13, no. 1, pp. 9-14, 2009.
[23] D. N. Parmar *et al.*, “Tandem scanning confocal corneal microscopy in the diagnosis of suspected Acanthamoeba keratitis,” *Ophthalmology,* vol. 113, no. 4, pp. 538-547, 2006.
[24] M. R. Kanavi *et al.*, “Sensitivity and specificity of confocal scan in the diagnosis of infectious keratitis,” *Cornea,* vol. 26, no. 7, pp. 782-786, 2007.
[25] E. Y. Tu *et al.*, “The relative value of confocal microscopy and superficial corneal scrapings in the diagnosis of Acanthamoeba keratitis,” *Cornea,* vol. 27, no. 7, pp. 764-772, 2008.
[26] Y. Matsumoto *et al.*, “The application of in vivo confocal scanning laser microscopy in the management of Acanthamoeba keratitis,” *Mol Vis,* vol. 13, no. 7, pp. 1319-1326, 2007.
[27] K. Babu, and K. R. Murthy, “Combined fungal and acanthamoeba keratitis: diagnosis by in vivo confocal microscopy,” *Eye,* vol. 21, no. 2, pp. 271-272, 07/14/online, 2006.
[28] S. C. Hau *et al.*, “Diagnostic accuracy of microbial keratitis with in vivo scanning laser confocal microscopy,” *British Journal of Ophthalmology,* vol. 94, no. 8, pp. 982-987, 2010.
[29] R. A. Copeland Jr, and N. Afshari, *Copeland and Afshari's Principles and Practice of Cornea*: JP Medical Ltd, 2013.
[30] K. Chamberlain, and J. Risma. "Confocal microscopy in fungal keratitis," http://webeye.ophth.uiowa.edu/eyeforum/atlas/pages/Confocal-microscopy-fungal-keratitis.
[31] S.-J. Chew *et al.*, “Early diagnosis of infectious keratitis with in vivo real time confocal microscopy,” *Eye & Contact Lens,* vol. 18, no. 3, pp. 197-201, 1992.
[32] A. Avunduk *et al.*, “Confocal microscopy of Aspergillus fumigatus keratitis,” *British journal of ophthalmology,* vol. 87, no. 4, pp. 409-410, 2003.
[33] K. Winchester, W. D. Mathers, and J. E. Sutphin, “Diagnosis of Aspergillus keratitis in vivo with confocal microscopy,” *Cornea,* vol. 16, no. 1, pp. 27-31, 1997.
[34] A. Labbé *et al.*, “Diagnosis of fungal keratitis by in vivo confocal microscopy: a case report,” *Eye,* vol. 25, no. 7, pp. 956-958, 03/11, 2011.
[35] F. Scarpa, D. Fiorin, and A. Ruggeri, "In Vivo Three-Dimensional Reconstruction of the Cornea from Confocal Microscopy Images." pp. 747-750.
[36] A. Ruggeri, and S. Pajaro, “Automatic recognition of cell layers in corneal confocal microscopy images,” *Computer Methods and Programs in Biomedicine,* vol. 68, no. 1, pp. 25-35, 4//, 2002.
[37] M. S. Sharif *et al.*, "An efficient system for preprocessing confocal corneal images for subsequent analysis." pp. 1-8.
[38] S. Al-Fahdawi *et al.*, "An Automatic Corneal Subbasal Nerve Registration System Using FFT and Phase Correlation Techniques for an Accurate DPN diagnosis." pp. 1035-1041.
[39] S. Al-Fahdawi *et al.*, “A fully automatic nerve segmentation and morphometric parameter quantification system for early diagnosis of diabetic neuropathy in corneal images,” *computer methods and programs in biomedicine,* vol. 135, pp. 151-166, 2016.
[40] G. D. Tsibidis *et al.*, “Semi-automated Acanthamoeba polyphaga detection and computation of Salmonella typhimurium concentration in spatio-temporal images,” *Micron,* vol. 42, no. 8, pp. 911-920, 2011.
[41] Q. Qiu *et al.*, "Automatic detecting cornea fungi based on texture analysis." pp. 214-217.

[42] J. D. Chidambaram *et al.*, “Prospective study of the diagnostic accuracy of the in vivo laser scanning confocal microscope for severe microbial keratitis,” *Ophthalmology,* vol. 123, no. 11, pp. 2285-2293, 2016.
[43] G. A. Baxes, *Digital image processing: principles and applications*: John Wiley \\& Sons, Inc., 1994.
[44] R. C. Gonzalez, and R. E. Woods, *Digital Image Processing*: Addison-Wesley Longman Publishing Co., Inc., 1992.
[45] P. Perona, and J. Malik, “Scale-space and edge detection using anisotropic diffusion,” *IEEE Transactions on Pattern Analysis and Machine Intelligence,* vol. 12, no. 7, pp. 629-639, 1990.
[46] C. Bazan, and P. Blomgren, “Image smoothing and edge detection by nonlinear diffusion and bilateral filter,” *CSRCR2007,* vol. 21, pp. 2-15, 2007.
[47] C. Pal, A. Chakrabarti, and R. Ghosh, “A Brief Survey of Recent Edge-Preserving Smoothing Algorithms on Digital Images,” *arXiv preprint arXiv:1503.07297*, 2015.
[48] M. J. Black, and G. Sapiro, "Edges as outliers: Anisotropic smoothing using local image statistics," *Scale-Space Theories in Computer Vision*, pp. 259-270: Springer, 1999.
[49] K. He, J. Sun, and X. Tang, “Single Image Haze Removal Using Dark Channel Prior,” *IEEE Transactions on Pattern Analysis and Machine Intelligence,* vol. 33, no. 12, pp. 2341-2353, 2011.
[50] S. G. Narasimhan, and S. K. Nayar, “Vision and the Atmosphere,” *International Journal of Computer Vision,* vol. 48, no. 3, pp. 233-254.
[51] E. Samei *et al.*, “Assessment of display performance for medical imaging systems: executive summary of AAPM TG18 report,” *Medical physics,* vol. 32, no. 4, pp. 1205-1225, 2005.
[52] E. Samei *et al.*, “Toward Clinically Relevant Standardization of Image Quality,” *Journal of Digital Imaging,* vol. 17, no. 4, pp. 271-278, 11/25, 2004.
[53] U. Qidwai, and C.-h. Chen, *Digital image processing: an algorithmic approach with MATLAB*: CRC press, 2009.
[54] The MathWorks Inc. "Identifying Round Objects," 17 April, 2016; https://uk.mathworks.com/examples/image/mw/images_product-RoundObjectsExample-identifying-round-objects.
[55] Wikipedia. "Shape factor (image analysis and microscopy)," 16 NOV, 2016; https://en.wikipedia.org/wiki/Shape_factor_(image_analysis_and_microscopy).
[56] P. Subashini, and N. Sridevi, “An optimal binarization algorithm based on Particle Swarm Optimization,” *International Journal of Soft Computing and Engineering (IJSCE),* vol. 1, 2011.
[57] B.-J. Cho, and E. J. Holland, “In vivo tandem scanning confocal microscopy in acanthamoeba keratitis,” *Korean Journal of Ophthalmology,* vol. 12, no. 2, pp. 112-107, 1998.
[58] A. K. Akobeng, “Understanding diagnostic tests 1: sensitivity, specificity and predictive values,” *Acta paediatrica,* vol. 96, no. 3, pp. 338-341, 2007.
[59] A.-M. Šimundić, “Measures of diagnostic accuracy: basic definitions,” *EJIFCC,* vol. 19, no. 4, pp. 203, 2009.
[60] D. G. Lowe, “Distinctive image features from scale-invariant keypoints,” *International journal of computer vision,* vol. 60, no. 2, pp. 91-110, 2004.
[61] U. Sinha. "SIFT: Theory and Practice," December 20, 2016; http://aishack.in/tutorials/sift-scale-invariant-feature-transform-introduction/.
[62] Murray. "SIFT Image Features," December 20, 2016; http://homepages.inf.ed.ac.uk/rbf/CVonline/LOCAL_COPIES/AV0405/MURRAY/SIFT.html.
[63] A. Kovnatsky. "Feature points in image, Keypoint extraction," February 20, 2016; http://uk.mathworks.com/matlabcentral/fileexchange/29004-feature-points-in-image--keypoint-extraction.

[64] S. Gupta, and Y. Kaur, “Review of Different Local and Global Contrast Enhancement Techniques for a Digital Image,” *International Journal of Computer Applications (0975–8887) Volume*, 2014.
[65] A. Namdeo, and S. S. Bhadoriya, “A Review on Image Enhancement Techniques with its Advantages and Disadvantages.”
[66] D.-J. Kroon, C. Slump, and T. J. Maal, "Optimized Anisotropic Rotational Invariant Diffusion Scheme on Cone-Beam CT," *Medical Image Computing and Computer-Assisted Intervention – MICCAI 2010*, Lecture Notes in Computer Science T. Jiang *et al.*, eds., pp. 221-228: Springer Berlin Heidelberg, 2010.
[67] L. Fritz, “Diffusion-based applications for interactive medical image segmentation,” *Proceedings of CESCG,* vol. 2006, 2006.
[68] J. Weickert, “A review of nonlinear diffusion filtering,” *Scale-space theory in computer vision*, pp. 1-28, 1997.
[69] J. Weickert, "Theoretical foundations of anisotropic diffusion in image processing," *Theoretical foundations of computer vision*, pp. 221-236: Springer, 1996.
[70] J. Weickert, “Coherence-enhancing diffusion filtering,” *International journal of computer vision,* vol. 31, no. 2, pp. 111-127, 1999.
[71] A. M. Mendrik *et al.*, “Noise reduction in computed tomography scans using 3-D anisotropic hybrid diffusion with continuous switch,” *IEEE Transactions on Medical Imaging,* vol. 28, no. 10, pp. 1585-1594, 2009.
[72] J.-M. Mirebeau *et al.*, “Anisotropic diffusion in ITK,” *arXiv preprint arXiv:1503.00992*, 2015.
[73] D. Kroon, and C. Slump, “Coherence filtering to enhance the mandibular canal in cone-beam CT data,” 2009.
[74] J. Weickert, and H. Scharr, “A scheme for coherence-enhancing diffusion filtering with optimized rotation invariance,” *Journal of Visual Communication and Image Representation,* vol. 13, no. 1-2, pp. 103-118, 2002.
[75] P. Thomas, and J. Kaliamurthy, “Mycotic keratitis: epidemiology, diagnosis and management,” *Clinical Microbiology and Infection,* vol. 19, no. 3, pp. 210-220, 2013.
[76] S. M. Kurian, “Live-cell imaging of the early stages of colony development in Fusarium oxysporum in vitro and ex vivo during infection of a human corneal model,” University of Manchester, 2016.
[77] W. Suparta, and W. Putro, "Analysis distribution of galactic cosmic rays particle energy with polar orbit satellite for Geant4 application." p. 012038.

Appendix A

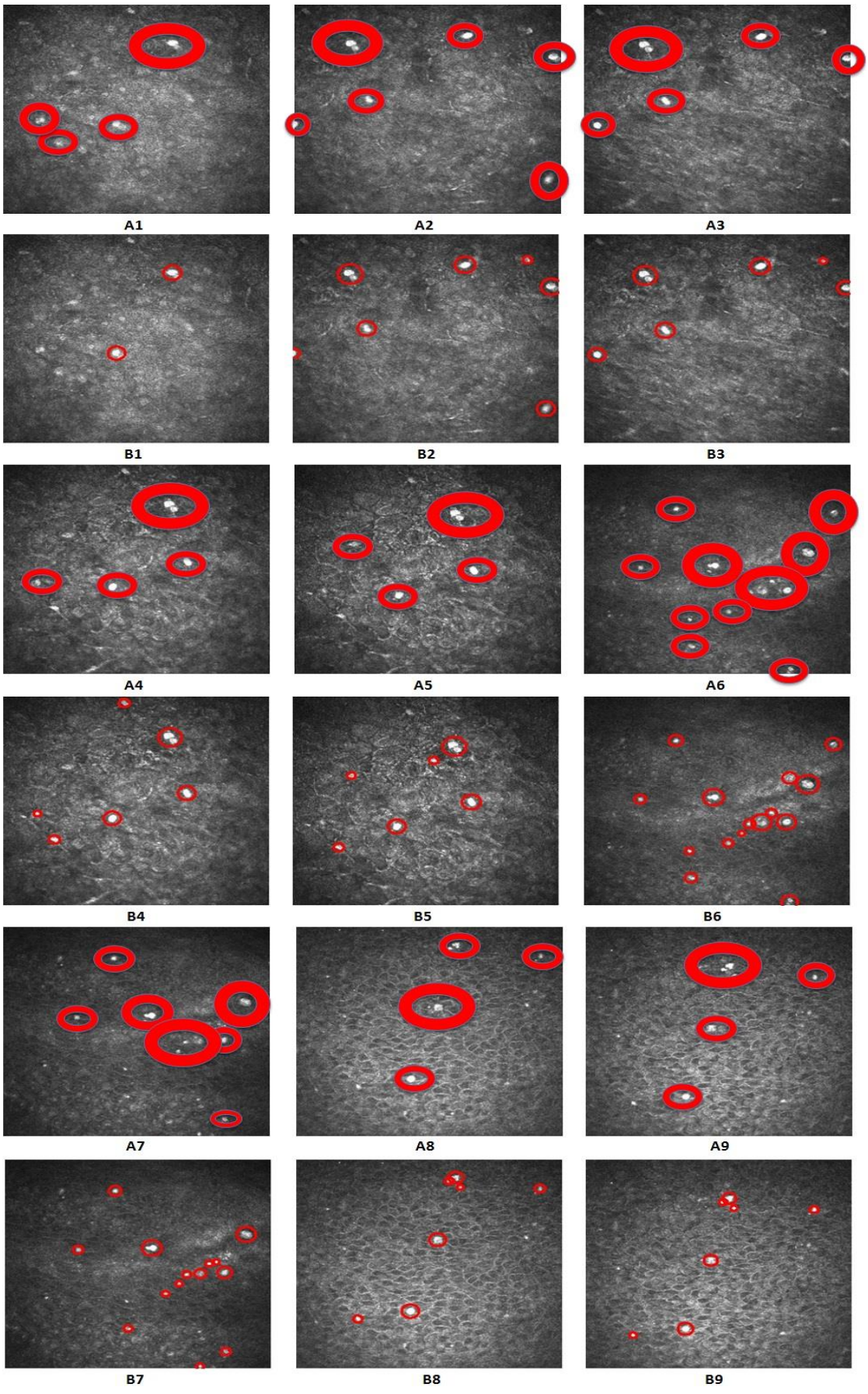

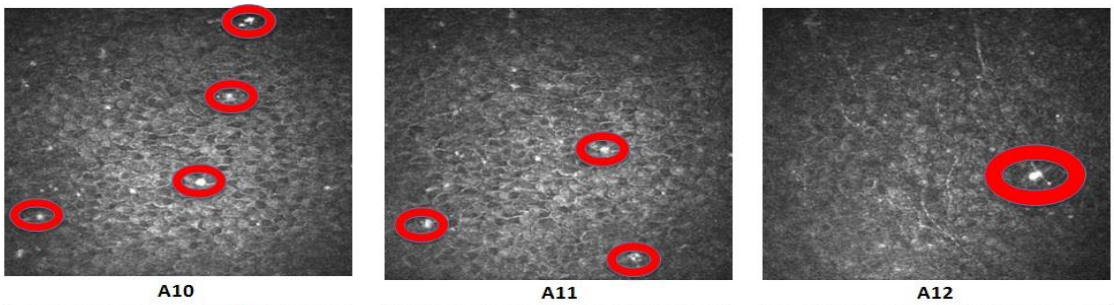

A10 A11 A12

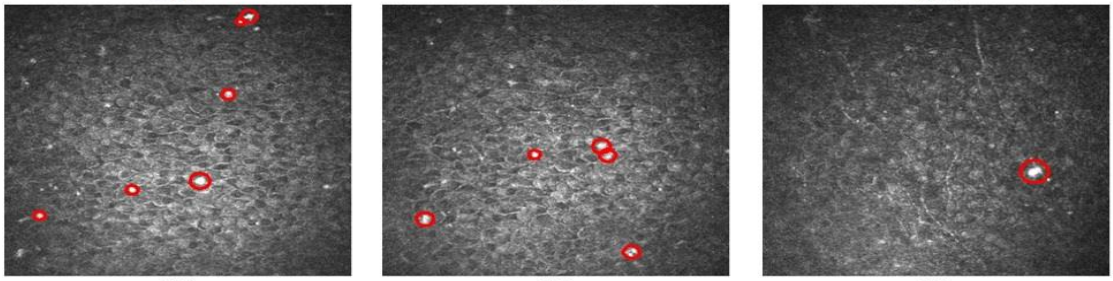

B10 B11 B12

A13 A14 A15

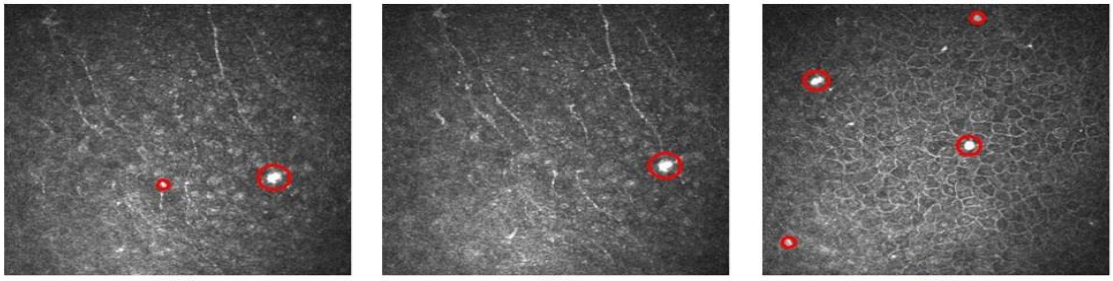

B13 B14 B15

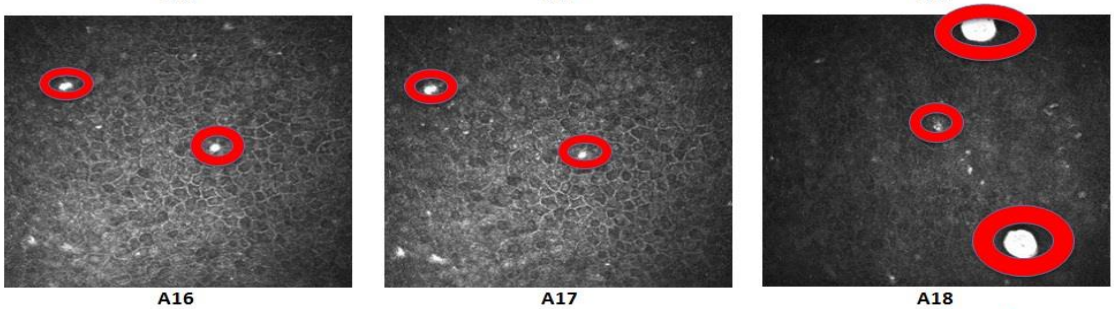

A16 A17 A18

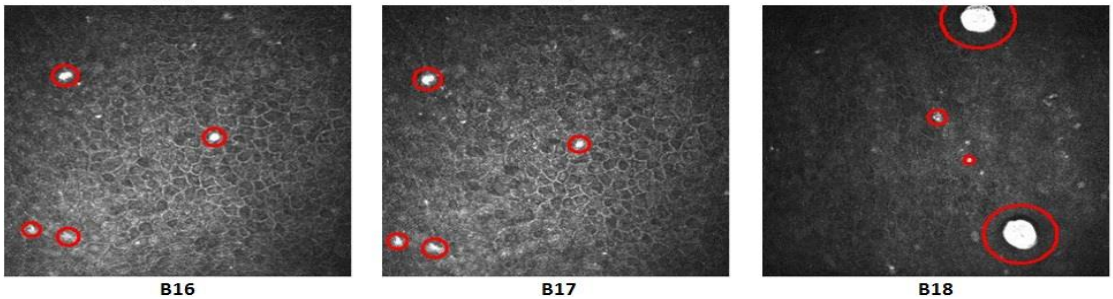

B16 B17 B18

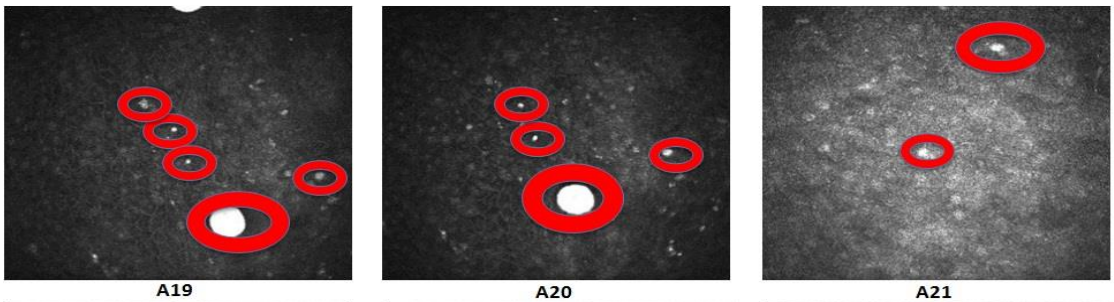

A19 A20 A21

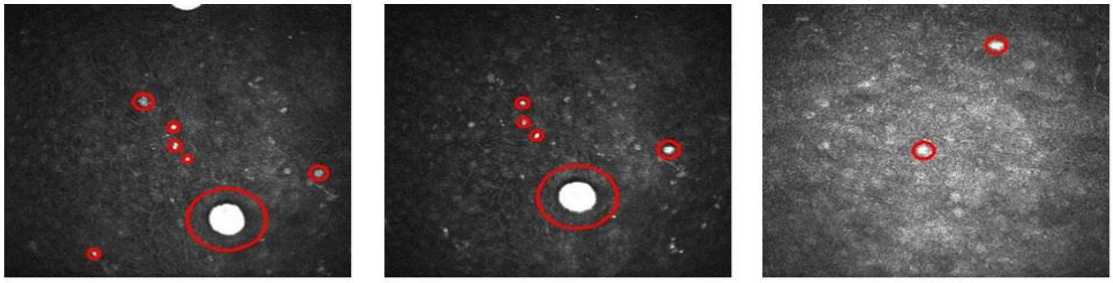

B19 B20 B21

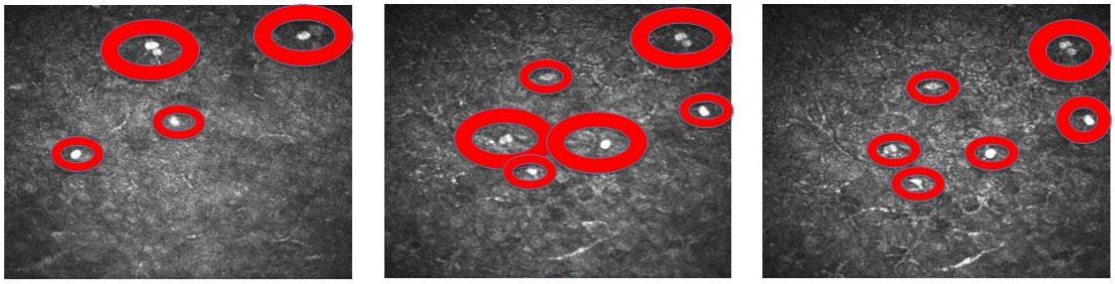

A22 A23 A24

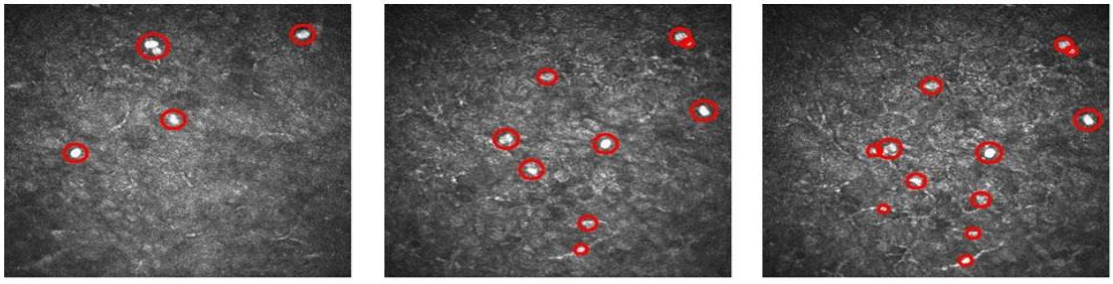

B22 B23 B24

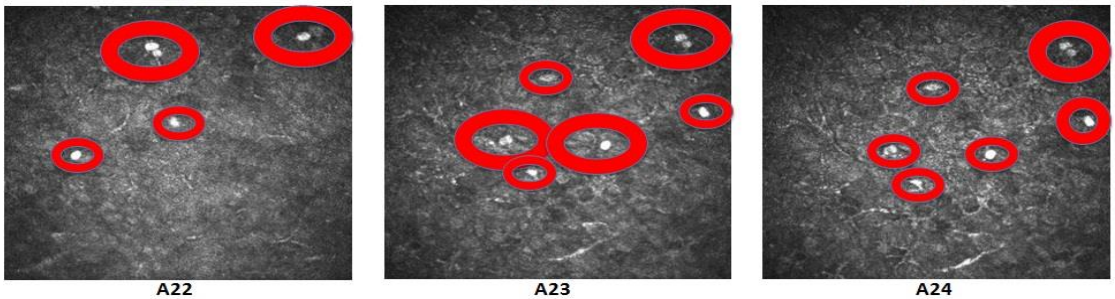

A22 A23 A24

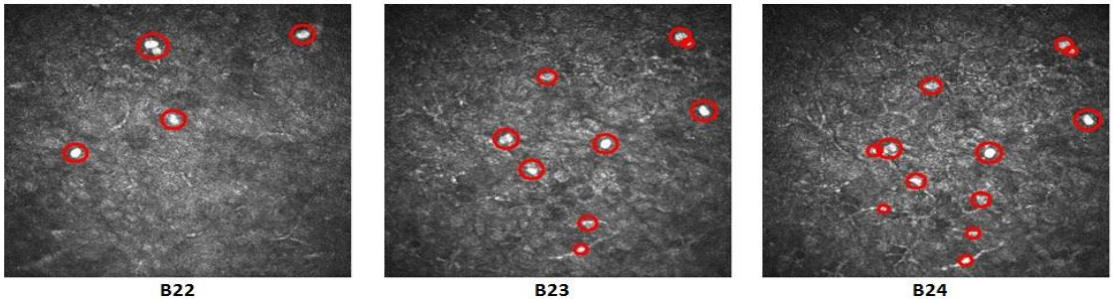

B22 B23 B24

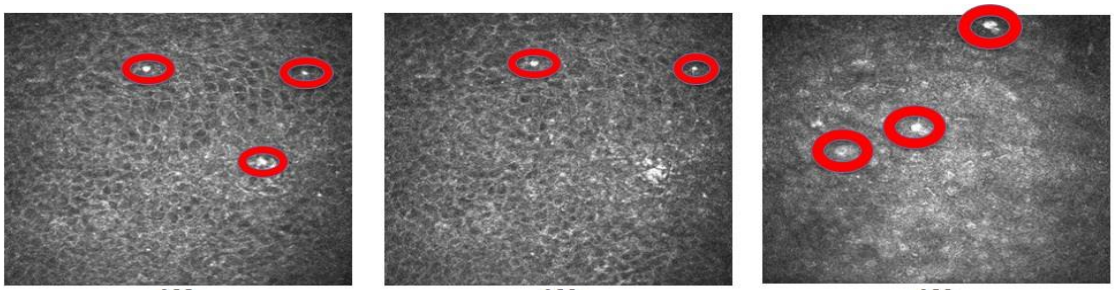

A28 A29 A30

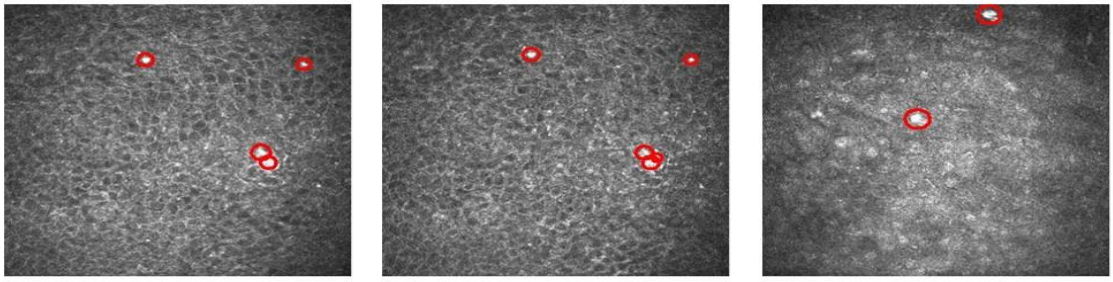

B28 B29 B30

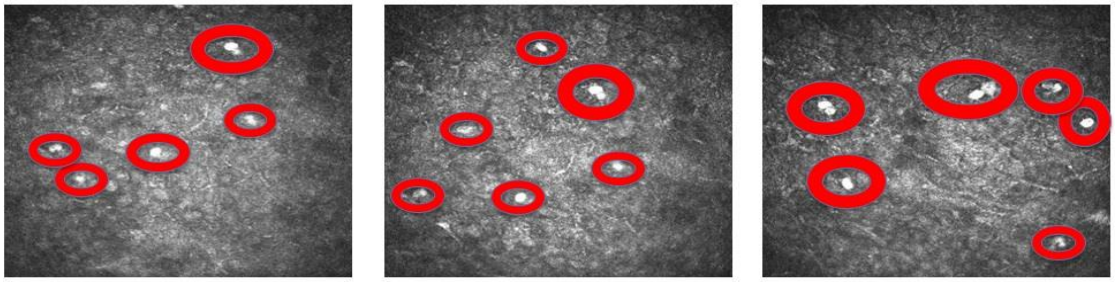

A31 A32 A33

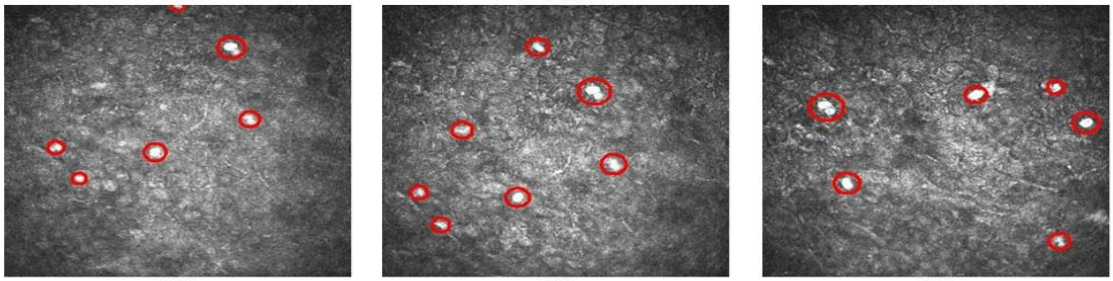

B31 B32 B33

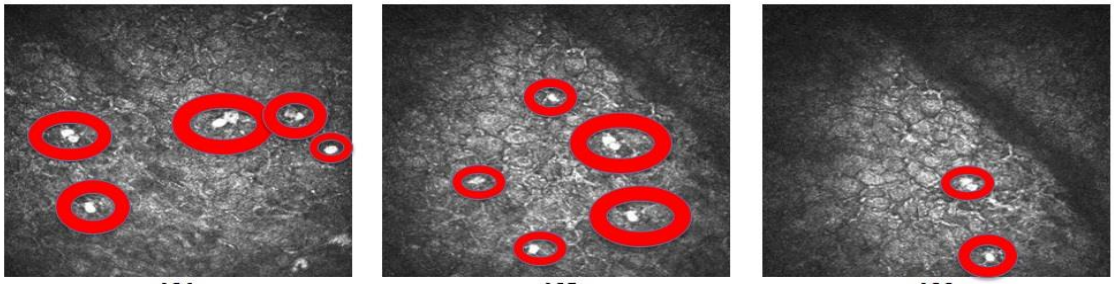

A34 A35 A36

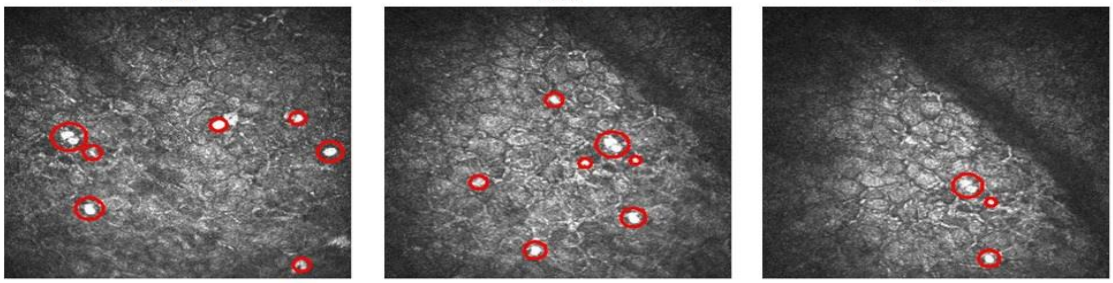

B34 B35 B36

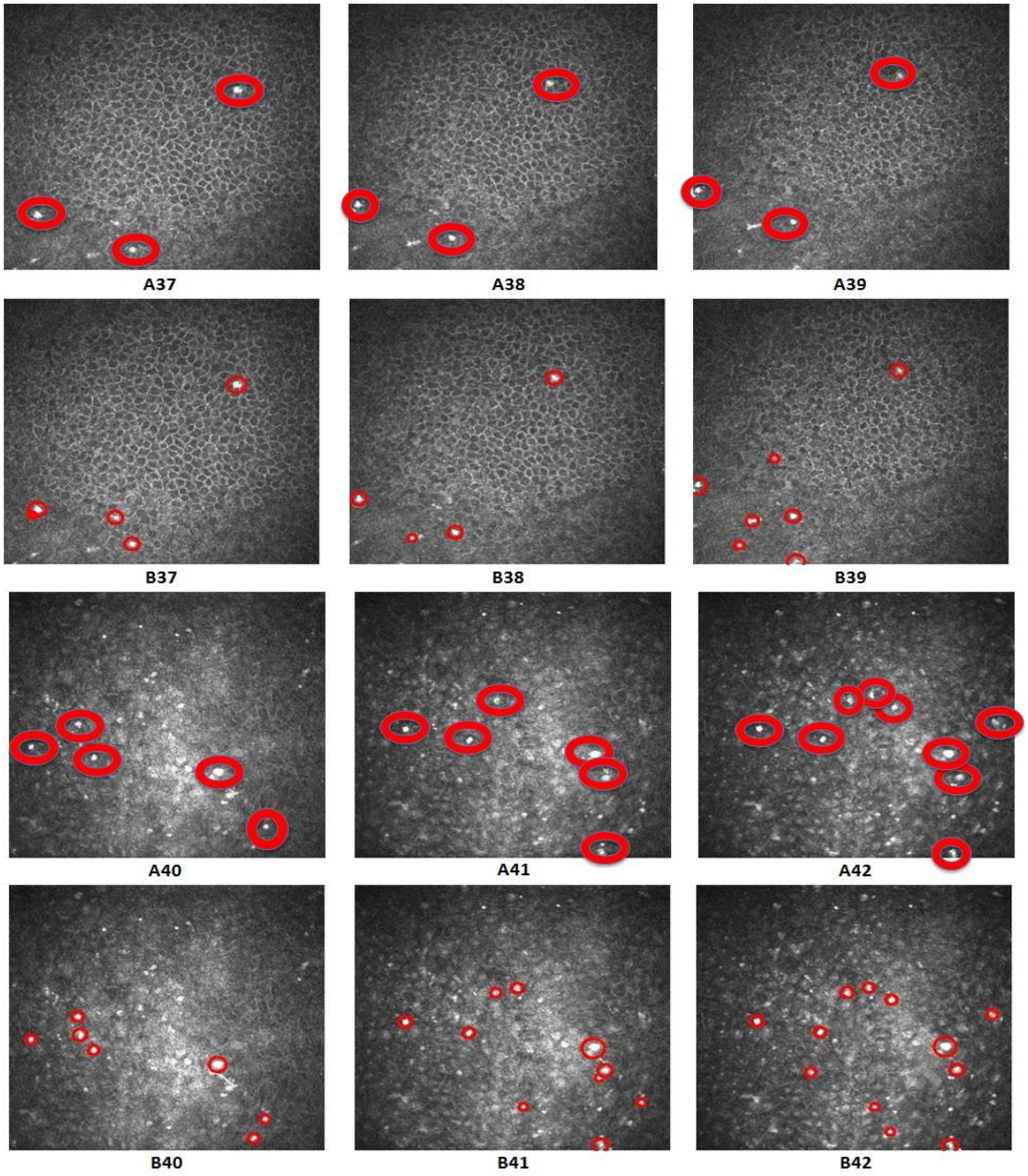

Figure A.1 The rest of Acanthamoeba images in the dataset to evaluate the performance of the proposed segmentation process for Acanthamoeba keratitis cysts in comparison to the manual segmentation. A1-A42) Manual detection of Acanthamoeba cysts by the clinical consultant. B1-B42) Automated detection of Acanthamoeba cysts by the developed system.

Appendix B

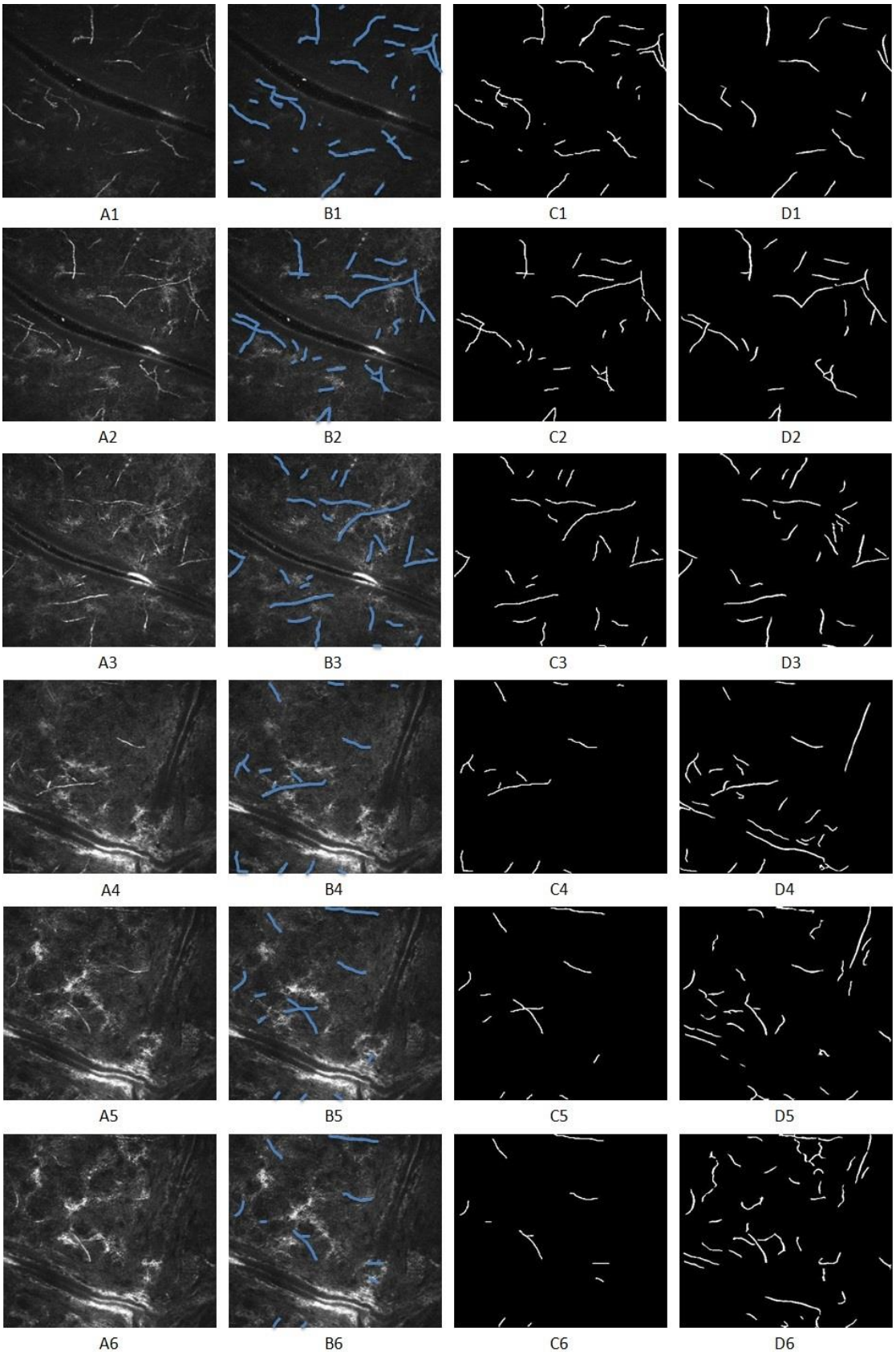

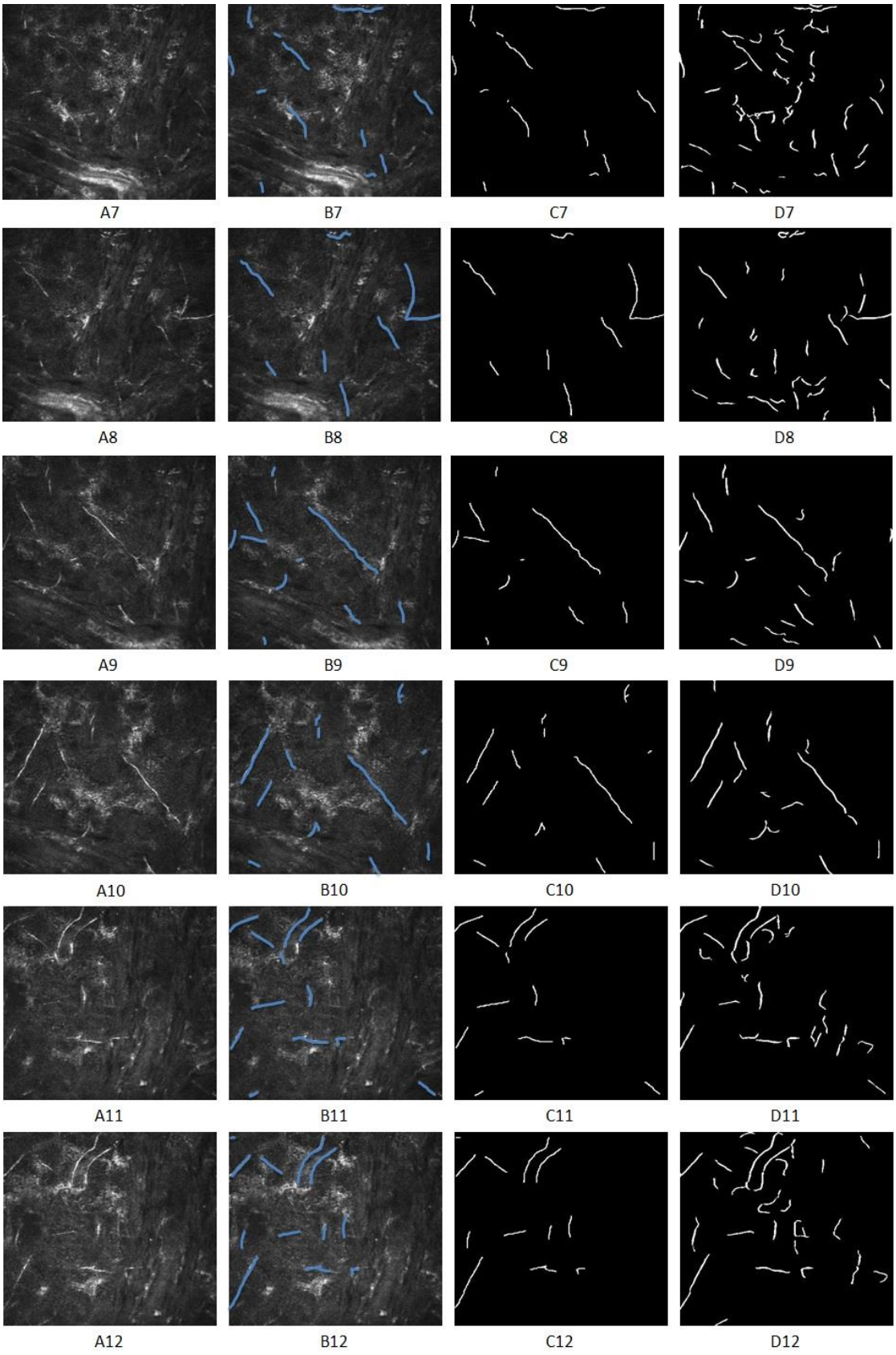
A7
B7
C7
D7
A8
B8
C8
D8
A9
B9
C9
D9
A10
B10
C10
D10
A11
B11
C11
D11
A12
B12
C12
D12

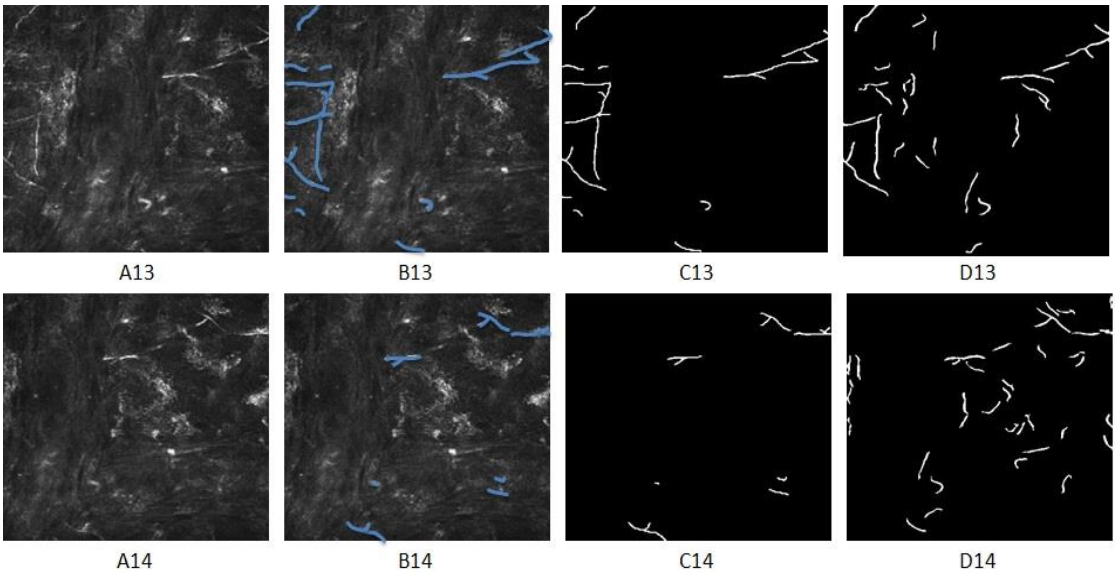

Figure B.1 The rest of Fusarium images in the dataset to evaluate the performance of the proposed segmentation process of Fusarium hyphae. A1-A14) Input images. B1-B14) The manually traced hyphae. C1-C14) Binarisation of the manual traced hyphae. D1-D14) Binarisation of the automated traced hyphae.

Appendix C

This part shows the GUI that is developed to provide ophthalmologists with an easy and friendly way to diagnose Acanthamoeba Keratitis (see Figure C.1) and Fusarium (see Figure C.2). All the techniques and algorithms used and proposed in this work are implemented using MATLAB (R2014a).

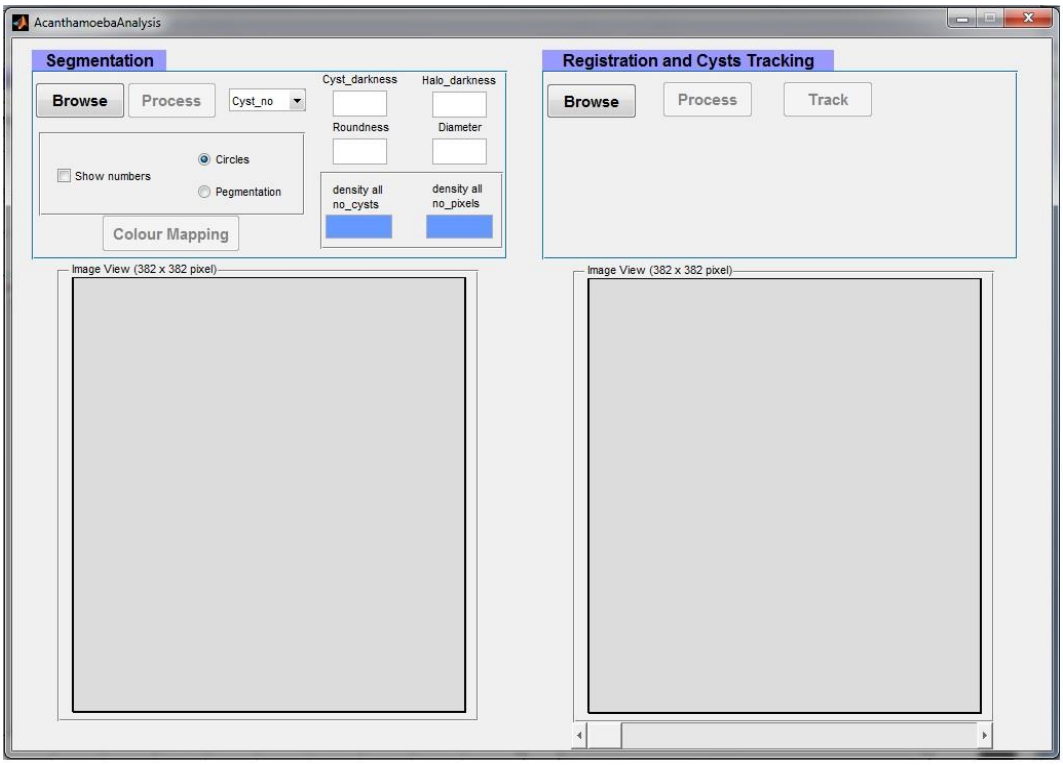

Figure C.1 The GUI of Acanthamoeba Keratitis diagnosis.

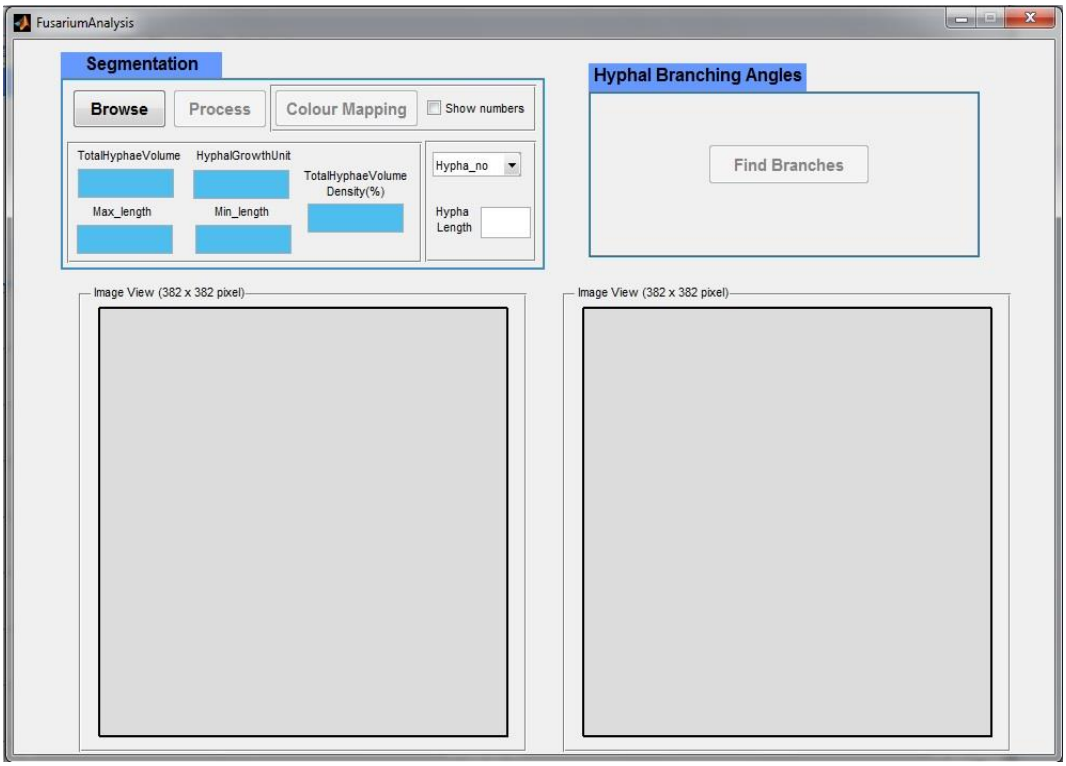

Figure C.2 The GUI of Fusarium diagnosis.

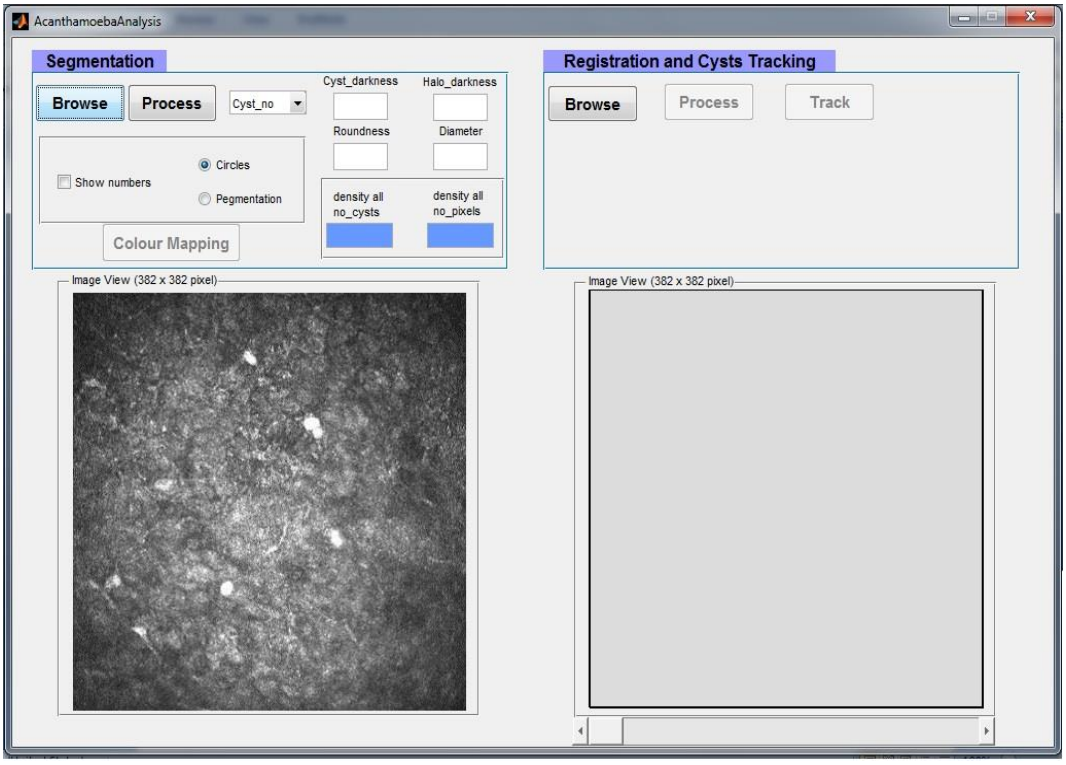

Figure C.3 Select the image to be processed using the 'Browse' button.

In regards to the Acanthamoeba diagnosis system, in the segmentation side, the user can select one image to be processed using the 'Browse' button as shown in Figure C.3. After selecting the image to be processed, the 'Process' button becomes active. This button is used to detect the suspicious cysts. It implicitly applies the enhancement and the segmentation procedures. Figure C.4 shows the output of the process step.

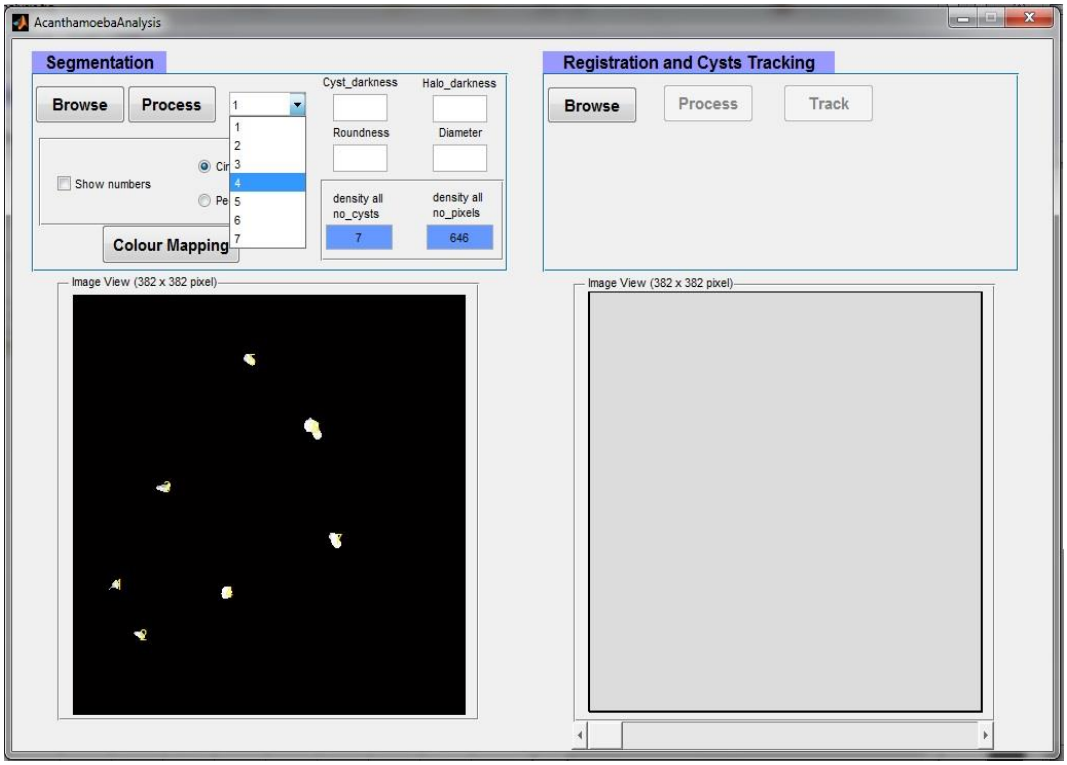

Figure C.4 The segmented image with cysts numbers produced by the 'Process' button.

The parameters that are used to quantitatively analyse the detected cysts are also computed in the 'process' step. Each cyst has a number. According to the selected number in the pop-up menu, the related values appear in the boxes as shown in Figure C.5.

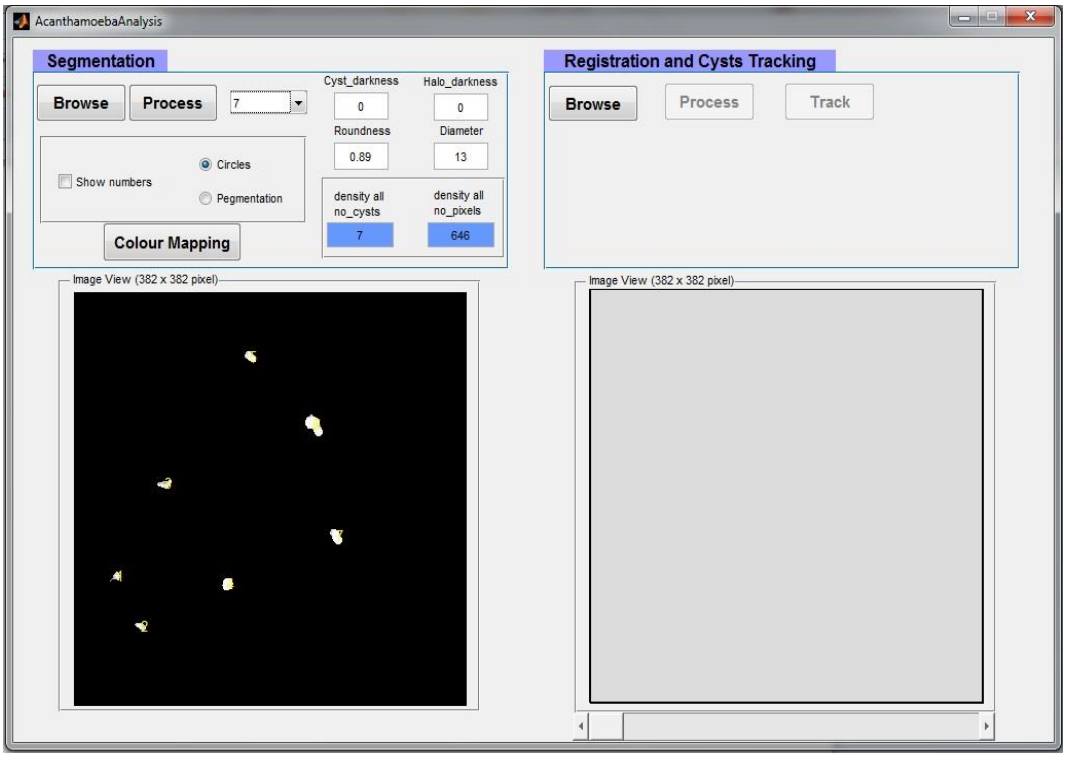

Figure C.5 The related quantitative values of the selected number in the pop-up menu.

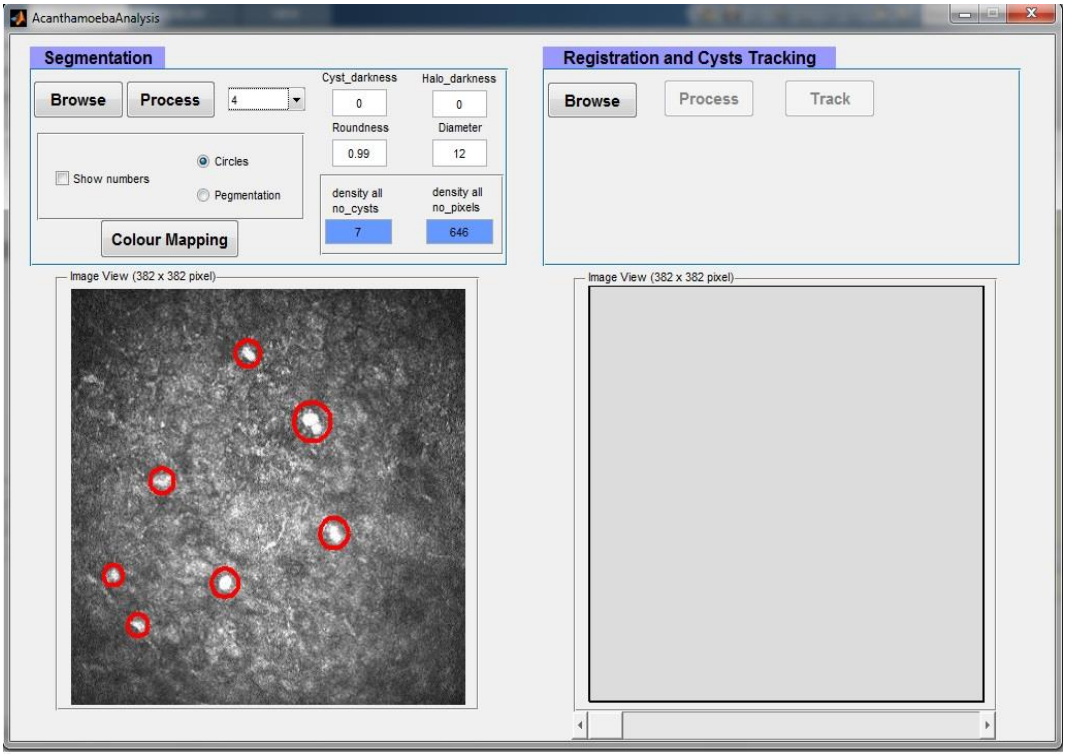

Figure C.6 Tracing for the detected cysts on the original image (displayed as circles) using the 'Colour Mapping' button.

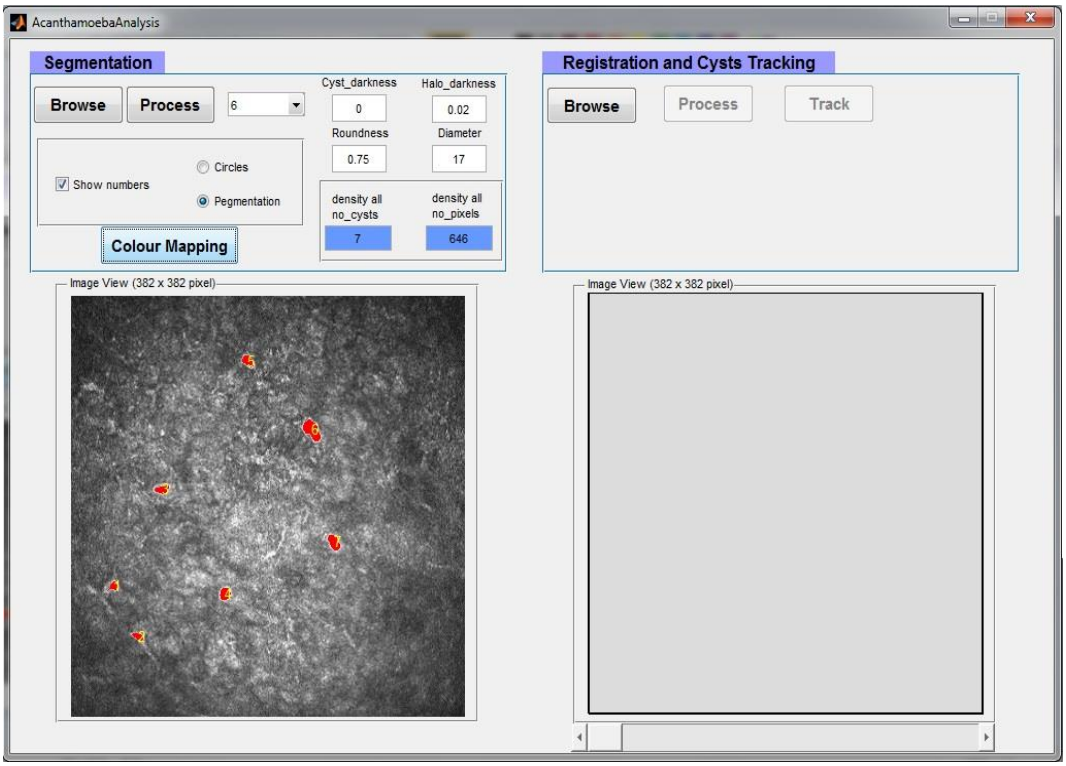

Figure C.7 Tracing for the detected cysts on the original image (displayed as pigmentation) using the 'Colour Mapping' button. The number of each cyst appears because the 'Show numbers' box is selected.

To do tracing for the detected cysts on the original image, the 'Colour Mapping' button is used. This colour mapping can be displayed as circles surrounding the cysts (see Figure C.6) or as pigmentation (see Figure C.7). In both cases, the number of each cyst can be shown when the 'Show numbers' box is selected. In the registration and cyst tracking side, which is separate from the segmentation part, the user can select a sequence of ordered images to be registered. Figure C.8 shows an example of selecting two images. The slide bar is used to view the selected images.

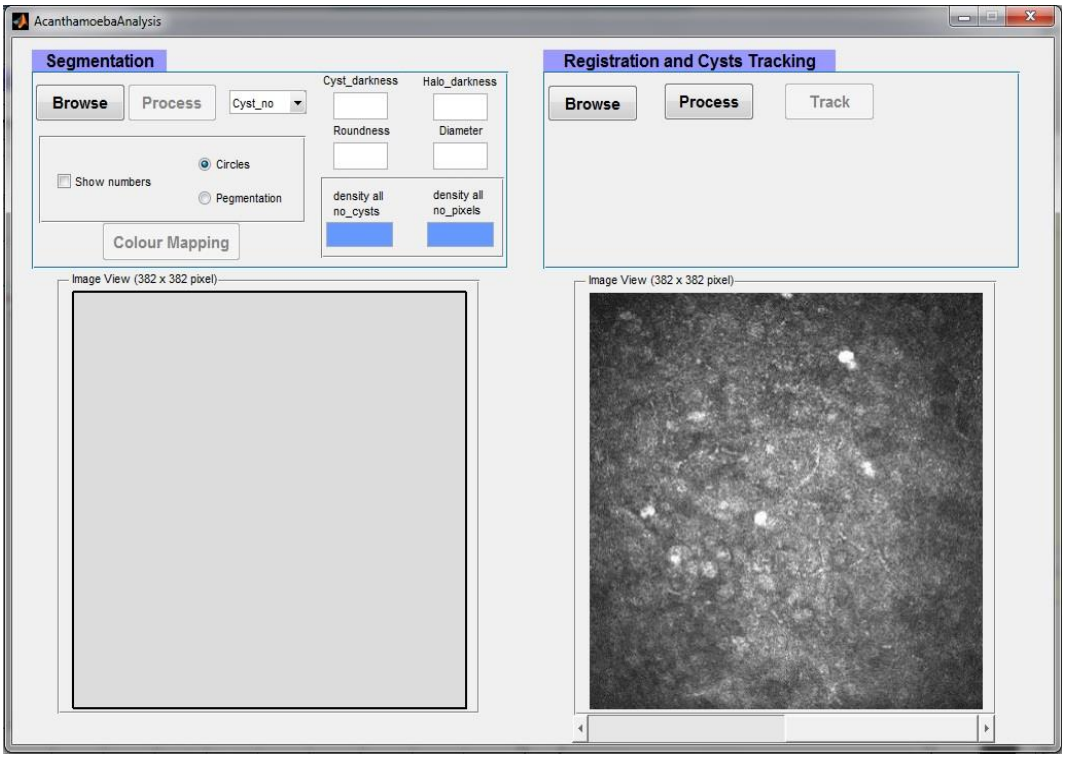

Figure C.8 Select multiple images to be registered (at least two images as shown in the example) using the 'Browse' button.

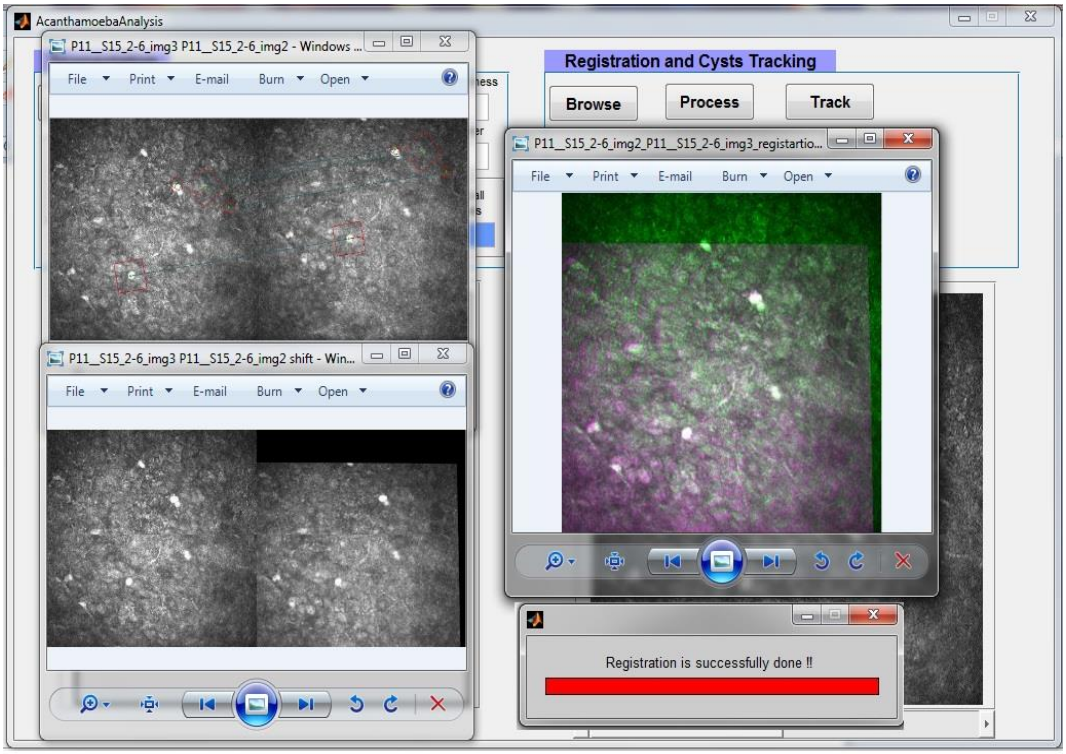

Figure C.9 The result of Registration process using the 'Process' button.

The 'Process' button is used to apply the registration algorithm and the result is saved in a folder titled 'Registration_Results'. This folder contains three Figures for every two adjacent images to be registered. The first Figure shows the matching point pairs between the two images, while the second Figure shows the image after applying the estimated geometric transformation lying beside the next image to be integrated with. A combination of the two images to be integrated is shown in the third Figure. The result of the registration step is shown in Figure C.9.

The 'Track' button is used to track each cyst in the whole sequence of registered images. The cyst that appears multiple times in the sequence gets the same tracking number. The result of this step is saved in a folder labelled 'Tracking_Results'. This folder contains each image in the sequence with the cyst tracking numbers. Figure C.10 shows the result of cyst tracking.

The quantitative analysis for detected cysts is automatically computed and saved in a file in the 'Tracking_Results' folder. The quantitative parameters of the illustrated example are shown in Table C.1.

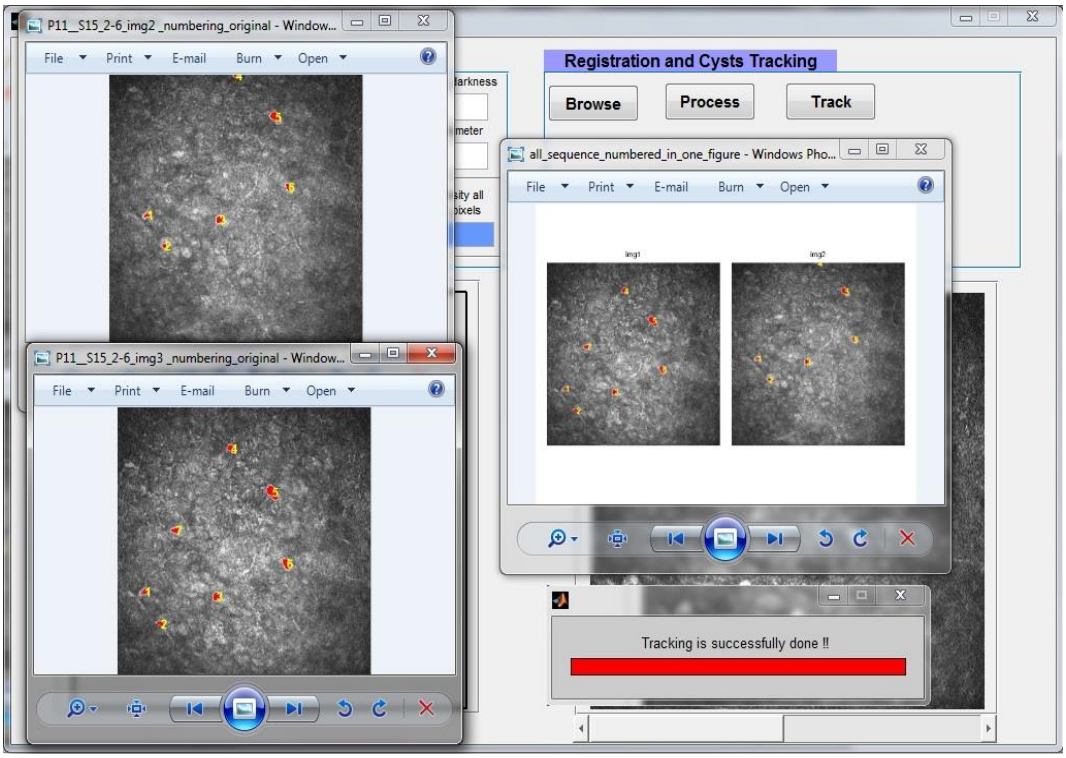

Figure C.10 The result of cyst tracking using the 'Track' button.

Image_name	Cyst_order	Cyst_no	Darkness	Diameter	Roundness	Halo	Availability	Cysts_count
P11__S15_2-6_img2	1	1	0	8	0.73	0	yes	6
P11__S15_2-6_img2	2	2	0	7	1.16	0	yes	6
P11__S15_2-6_img2	3	3	0	12	0.93	0	yes	6
P11__S15_2-6_img2	4	4	0	6	1.09	0.16	yes	6
P11__S15_2-6_img2	5	5	0	14	0.79	0.01	yes	6
P11__S15_2-6_img2	6	6	0	10	0.9	0	yes	6
P11__S15_2-6_img3	1	1	0	9	0.7	0	No	7
P11__S15_2-6_img3	2	2	0	9	0.92	0.04	No	7
P11__S15_2-6_img3	3	7	0	11	0.77	0	No	7
P11__S15_2-6_img3	4	3	0	12	0.99	0	No	7
P11__S15_2-6_img3	5	4	0	12	0.91	0.05	No	7
P11__S15_2-6_img3	6	5	0	17	0.75	0.02	No	7
P11__S15_2-6_img3	7	6	0	13	0.89	0	No	7

Cyst_no	count of images	Depth in micron_start	Depth in micron_end	Images filenames
1	2	5	10	P11__S15_2-6_img2, P11__S15_2-6_img3
2	2	5	10	P11__S15_2-6_img2, P11__S15_2-6_img3
3	2	5	10	P11__S15_2-6_img2, P11__S15_2-6_img3
4	2	5	10	P11__S15_2-6_img2, P11__S15_2-6_img3
5	2	5	10	P11__S15_2-6_img2, P11__S15_2-6_img3
6	2	5	10	P11__S15_2-6_img2, P11__S15_2-6_img3
7	1	10	10	P11__S15_2-6_img3

Table C.1 The quantitative analysis for detected cysts which is automatically computed and saved in a file.

As for the Fusarium diagnosis system, in the segmentation side, the user can select one image to be processed using the Browse button as shown in Figure C.11. After selecting the image to be processed, the 'Process' button becomes active. This button is used to detect the suspicious hyphae. It implicitly applies the enhancement and the segmentation procedures. The parameters that are used to quantitatively analyse the detected hyphae are also computed in the process step and each hypha has a number.

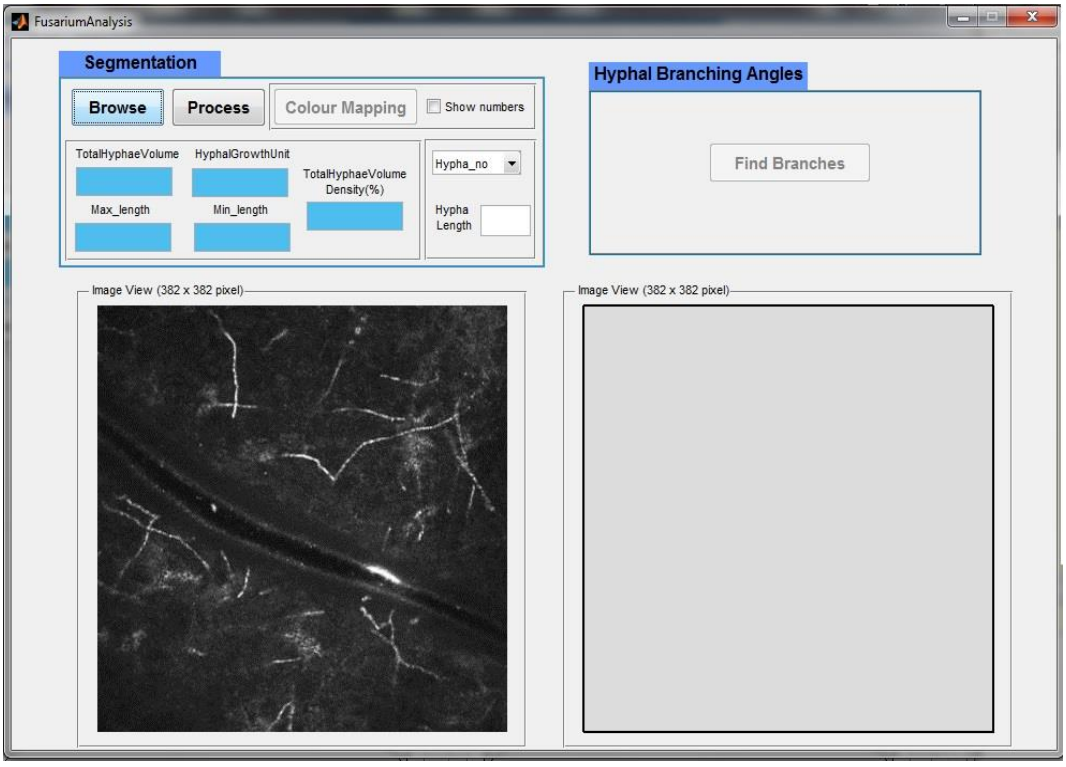

Figure C.11 Select the image to be processed using the 'Browse' button.

Figure C.12 shows the output of the 'process' step. To do tracing for the detected hyphae on the original image, the 'Colour Mapping' button is used (see Figure C.13).

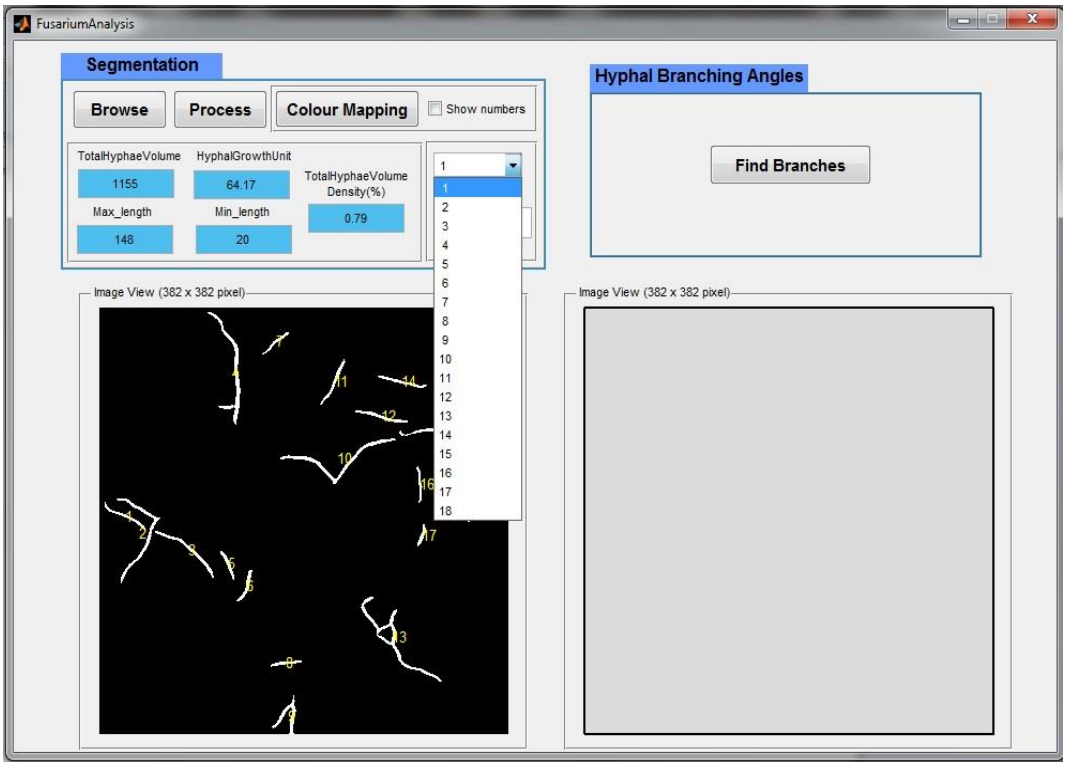

Figure C.12 The segmented image with hyphae numbers produced by the 'Process' button. The quantitative parameters are also computed.

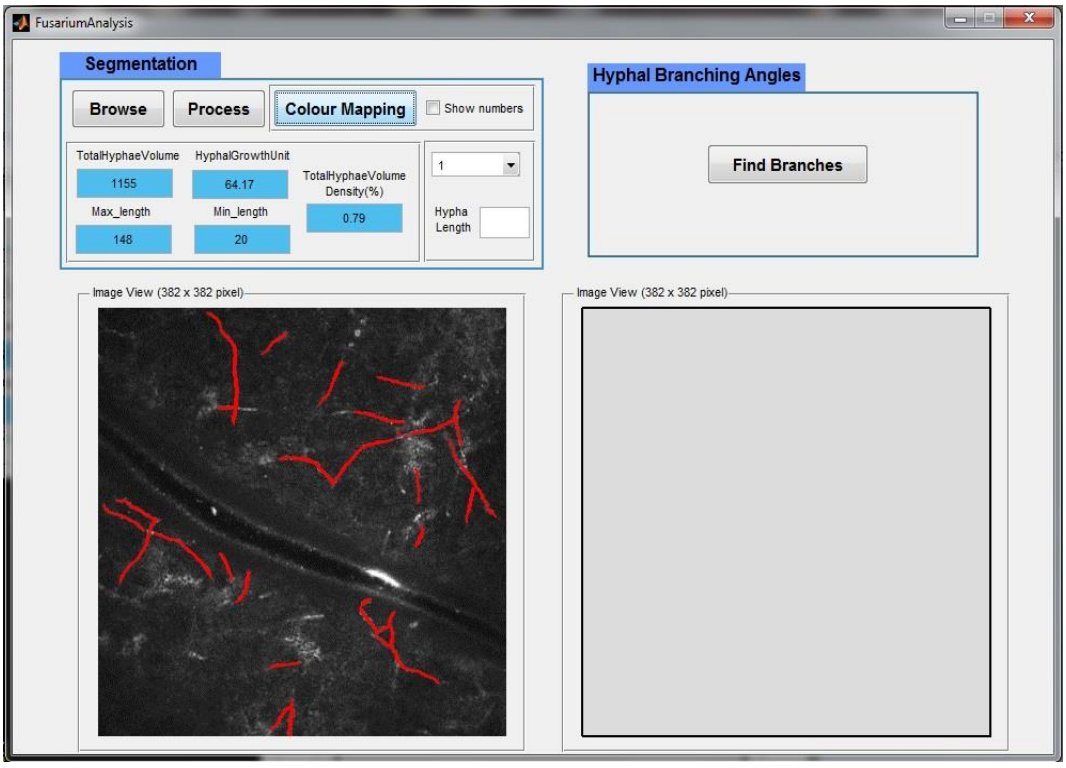

Figure C.13 Tracing for the detected hyphae on the original image.

The number of each hypha can be shown on the colour-mapped image when the 'Show numbers' box is selected (see Figure C.14). According to the selected number in the pop-up menu, the related length appears in the box as shown as well in Figure C.14.

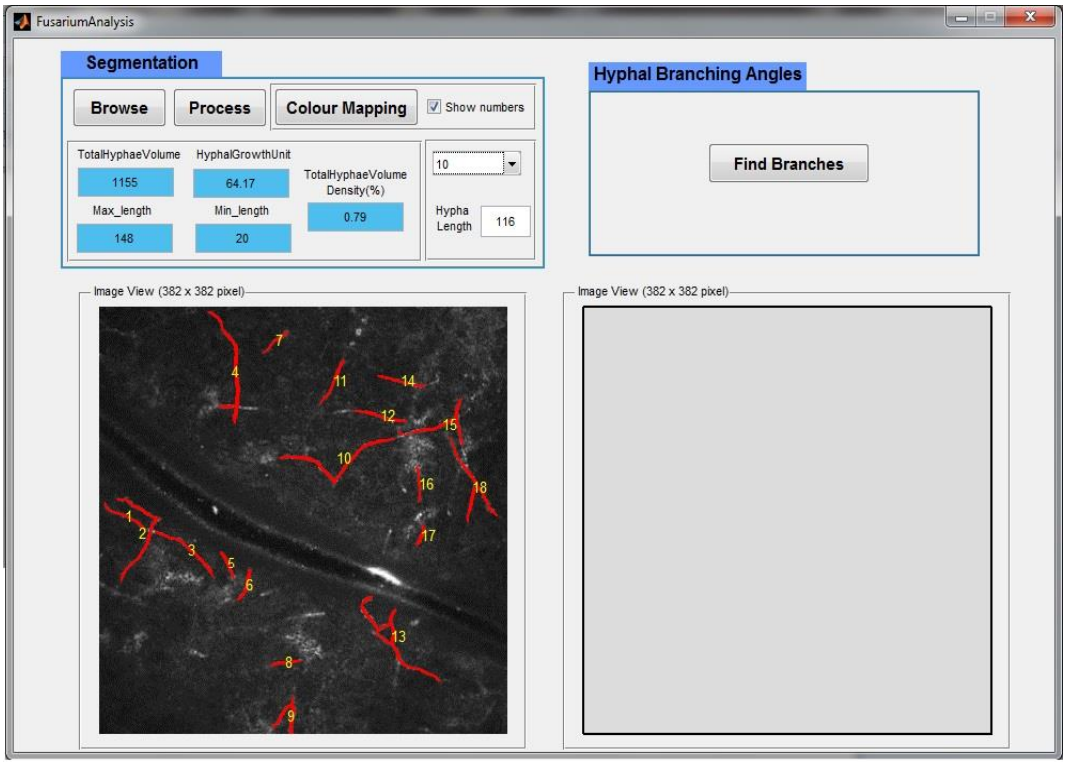

Figure C.14 Tracing for the detected hyphae on the original image with the appearance of the hyphae numbers because the 'Show numbers button' was selected. The length of any hypha appears when its related number is chosen from the pop-up menu.

In the hyphal branching angles side, which is connected to the segmentation part, the user can find the suspected branches and their angles by selecting the 'Find Branches' button. The result of the 'hyphal branching' step is shown in Figure C.15. The quantitative analysis for the segmented image is automatically computed and saved in a file as shown in Table C.2.

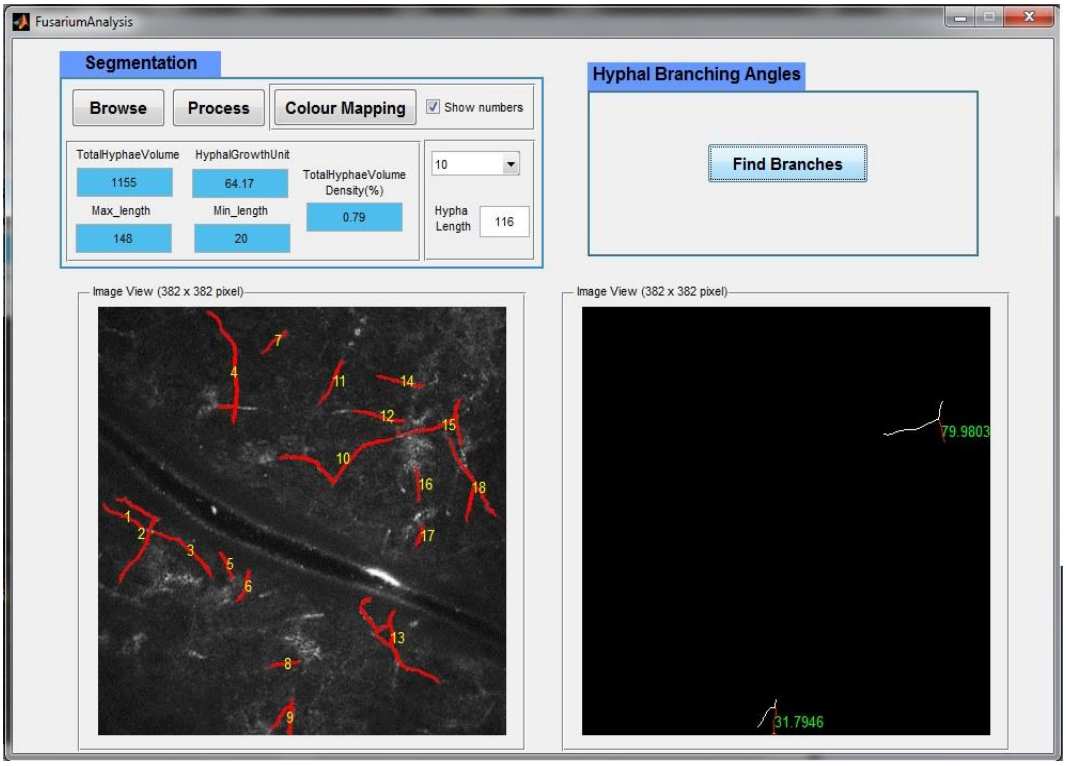

Figure C.15 Find the suspected branches and their angles in the processed image by selecting the 'Find Branches' button.

Image name	Total Hyphae Volume	Total Hyphae Volume Density	Hyphal Growth Unit	Max Length	Min Length
Fusa17	1155	0.79	64.17	148	20

Table C.2 The quantitative analysis for the segmented image which is automatically computed and saved in a file.

Appendix D

MATLAB function (or property)	Description
bwlabel	Label connected components in 2-D binary image.
skel	Morphological operation on binary images which removes pixels on the boundaries of objects but does not allow objects to break apart. The pixels remaining make up the image skeleton.
branchpoints	Morphological operation on binary images which finds branch points of skeleton. For example: 0 0 1 0 0 — 0 0 0 0 0 0 0 1 0 0 becomes 0 0 0 0 0 1 1 1 1 1 — 0 0 1 0 0 0 0 1 0 0 — 0 0 0 0 0 0 0 1 0 0 — 0 0 0 0 0
regionprops	Measure properties of image regions.
regionprops properties:	
Area	Actual number of pixels in the region, returned as a scalar.
EquivDiameter	Diameter of a circle with the same area as the region, returned as a scalar. Computed as sqrt(4*Area/pi).
PixelList	Locations of pixels in the region, returned as a *p*-by-Q matrix. Each row of the matrix has the form [x y z ...] and specifies the coordinates of one pixel in the region.
BoundingBox	Smallest rectangle containing the region, returned as a 1-by-Q*2 vector, where Q is the number of image dimensions.
MinorAxisLength	Length (in pixels) of the minor axis of the ellipse that has the same normalized second central moments as the region, returned as a scalar.
Orientation	Angle between the *x*-axis and the major axis of the ellipse that has the same second-moments as the region, returned as a scalar. The value is in degrees, ranging from -90 degrees to 90 degrees.

Appendix E

List of Seminars

1. **Developing an automated diagnostic corneal system to detect abnormalities in corneal layers of Fusarium patient using in vivo confocal microscopic images**. *Centre of visual computing*, *Jan 14, 2016. University of Bradford, UK*.
2. **Developing an automated diagnostic corneal system to detect abnormalities in corneal layers of Acanthamoeba keratitis patient using in vivo confocal microscopic images**. *IT Faculty, Aug 3, 2016. Jordan University of Science and Technology, Jordan*.
3. **Automated Diagnosis for Medical Imaging of Eye Diseases**. *School of Electrical Engineering and Computer Science, Mar 15, 2017. University of Bradford, UK*.
4. **Fully automated image processing system for diagnosis of corneal diseases**. *IT Faculty, Aug 16, 2017. Yarmouk University, Jordan*.